DOCTOR OF PHILOSOPHY

Fading in Wearable Communications Channels and its Mitigation

Yoo, Seong Ki

Award date:
2017

Awarding institution:
Queen's University Belfast

Fading in Wearable Communications Channels and its Mitigation

Seong Ki Yoo

School of Electronics, Electrical Engineering and Computer Science

Queen's University of Belfast

A thesis submitted for the degree of

Doctor of Philosophy

June 14, 2017

This page is intentionally left blank.

Abstract

The fabrication of miniature electronics and sensors has encouraged the creation of a wide range of wireless enabled devices designed to be worn on the human body. This has led to the prominence of so-called wearable communications, which have emerged to satisfy the demand for wireless connectivity between these devices and with external networks. The work in this thesis has focused on the characterization of the composite fading (i.e combined multipath and shadowing) observed in wearable communications channels. It has also investigated the mitigation of the deleterious effects of both of these propagation phenomena in wearable communications.

In order to accurately characterize the behaviour of the composite fading signal observed in wearable communications channels, new fading models such as $\mathcal{F}$, κ-μ / inverse gamma and η-μ / inverse gamma composite fading models, have been proposed. The generality and utility of these composite fading models have been validated through extensive field measurements performed in both indoor and outdoor environments with two key types of propagation geometry, i.e. line-of-sight (LOS) and non-LOS (NLOS) channel conditions.

The potential improvement in signal reliability for wearable communications channels has been empirically investigated using a switched combining based micro-diversity setup (to mitigate multipath) and a switched combining based macro-diversity configuration (to overcome shadowing). Three different switched combining schemes are considered, namely switch-and-stay combining (SSC), switch-and-examine

combining (SEC) and SEC with post-examining selection (SECps). The output of each switched combining scheme is also statistically characterized using diversity specific analytical equations. To mitigate occurrences of simultaneous multipath and shadowing, the signal reliability improvement which can be achieved when using dual-stage micro- and macro-diversity based combining has also been investigated through field measurements conducted in both indoor and outdoor environments.

Acknowledgements

I would like to thank my Ph.D supervisors, Dr. Simon L. Cotton and Prof. William G. Scanlon for their help, insight and guidance throughout the period of my Ph.D study. Their valuable feedback and enthusiasm for research made my Ph.D study a very enjoyable and rich experience. I hope that I could be as lively, enthusiastic and energetic as Simon and William.

I would also like to thank all the present members of Simon's research group: Dr. Adrian McKernan, Dr. Young Jin Chun, Mr. Michael G. Doone, Ms. Nidhi Bhargav and Mr. Son Dinh Van. My gratitude also extends to a number of people who were not part of the Simon's research group but helped me out, including Dr. Gareth Conway, Dr. Youngwook Ko and Dr. Michalis Matthaiou.

Finally, I would like to thank my family, in particular my parents for their constant support and encouragement throughout my life and the course of the Ph.D. Most importantly, I am deeply indebted to my lovely wife Shinyoung Lee, daughter Jimin Yoo and son Jaehyun Yoo for their love, support and sacrifice. Without them, I would never have been written.

This thesis is dedicated to

my parents,

my wife,

my daughter,

and my son.

Table of Contents

List of Figures

List of Tables

List of Acronyms

AF amount of fading.

AFD average fade duration.

AICc second-order Akaike information crieterion.

AOA angle of arrival.

BAN body area network.

BER bit error rate.

BSN body sensor network.

CDF cumulative distribution function.

D2D device-to-device.

DG diversity gain.

ECG electrocardiogram.

ECIT Institute of Electronics, Communications and Information Technology.

EGC equal gain combining.

FSK Frequency Shift Keyed.

i.i.d. independent and identically distributed.

i.n.i.d. independent and non-identically distributed.

KLD Kullback Leibler divergence.

K-S Kolmogorov-Smirnov.

LAN local area network.

LCR level crossing rate.

LOS line-of-sight.

MDPSK M-ary differential phase shift keying.

MGF moment generating function.

MIMO multiple-input and multiple-output.

MLE maximum likelihood estimation.

mm-wave millimetre-wave.

MRC maximal ratio combining.

NLOS non-LOS.

PAP power angle profile.

PDF probability density function.

PDP power delay profile.

PSC pure selection combining.

PVC polyvinyl chloride.

RAD resistor-average distance.

RF radio frequency.

RFMD RF Micro Devices.

rms root-mean-square.

RX receiver.

SEC switch-and-examine combining.

SECps SEC with post-examining selection.

SNR signal-to-noise ratio.

SSC switch-and-stay combining.

TI Texas Instruments.

TOA time of arrival.

TSC threshold selection combining.

TX transmitter.

VNA vector network analyzer.

WPAN wireless personal area network.

Chapter 1

Introduction

1.1 Wearable Communications

Recent advancements in the fabrication of miniature electronics and sensors have allowed the creation of a wide range of wearable devices which are designed to be carried or worn by the user. Among the many form factors available include watches, glasses, headbands, wigs and rings. As shown in Figure 1.1, wearable devices are being developed for a diverse range of applications [1], such as personal and business computing, medical, sport, military and communications. With the emergence of many new applications, wearable devices will continue to increase in popularity. However, it is worth pointing out that there has been growing scepticism of wearables [2] due to potential risks for users, invasion of their privacy, security concerns etc. Nevertheless, the wearables market is still expected to grow rapidly [3]. In fact, according to industry analyst firm, CCS Insight, the market value of connected wearable devices is expected to reach $ 34 million by 2020 and the shipment of wearable devices is set to reach 411 million by 2020 [4]. Additionally, CNBC reports that wearables will become the worlds best-selling consumer electronics product after smartphones [5].

For many wearable devices, wireless communications are necessary to transfer

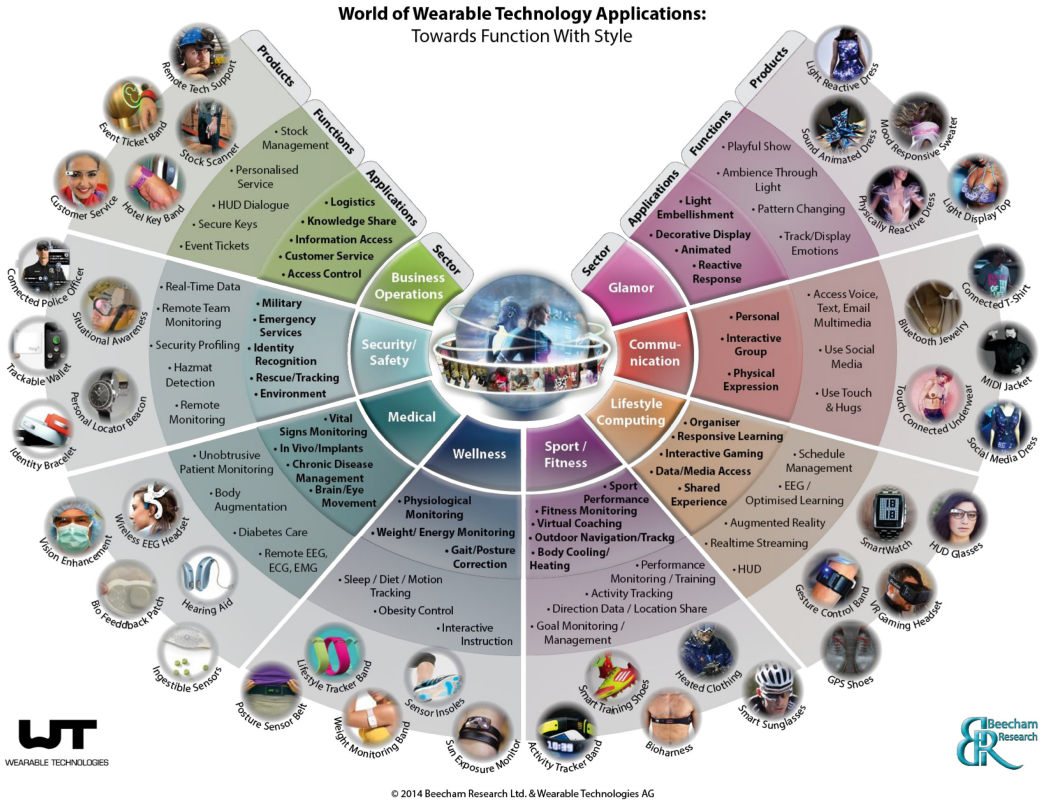

Figure 1.1: Wearable technology applications [1]

or receive data from external networks, which has led to the research area often being referred to as wearable communications. In wearable communications, one or more wireless devices carried or worn by the user may communicate with local transceivers or base stations in the local vicinity. This type of wireless communications is often referred to as off-body communications and is a fundamental part of wireless personal area networks (WPANs) currently standardized by the IEEE 802.15 *task group* 4 [6]. Additionally, wearable communications can also occur between wireless devices situated on the user's body using on-body communications. On-body communications often form the basis of connectivity in body area networks (BANs) and body sensor networks (BSNs) which have been standardized by the IEEE 802.15 *task group* 6 [7].

Since wearable devices are operated in close proximity to the human body, wearable communications systems can suffer from the complex antenna-body interaction effects such as near-field coupling, radiation pattern distortion, reduced radiation efficiency and shifts in antenna input impedance [8–10]. Furthermore,

the wearable channels can be particularly prone to shadowing induced by the movement of body parts and blockages caused by user's body and/or surrounding obstacles including other people [11–13]. The variation in the received signal can also occur due to the reflections from nearby objects and scattering from the body and local surrounding environments (i.e. multipath fading) [14]. All of these factors may degrade the quality of radio links and reduce the overall signal reliability and the performance of wearable systems. In accordance with these deleterious effects, research in context of the wearable communications can be broadly divided into three key areas. These are summarized as follows:

- **Antenna Design**: Antennas often need to be specially designed for use in wearable devices. In particular, when used in conjunction with radio frequency (RF) and baseband circuitry, they are required to be compact, lightweight, robust, ultra-low power architectures and unobtrusive to the user.

- **Channel Characterization and Modelling**: As a precursor to wireless systems development, it is essential to characterize fading behaviour accurately to analyse performance and improve design. The fading observed in wearable communications channels can be modelled in terms of fundamental statistics, such as the probability density functions (PDFs), cumulative distribution functions (CDFs) and moment generating functions (MGFs). The PDF is the most commonly used for characterizing fading channels and it can also be used for the use of diversity system and error correction coding [15]. However, from the point of view of the performance analysis, the CDF and MGF play an important role in the computation of the communications performance metrics of interest, such as error probability and outage probability [16, 17].

- **Signal Improvement Techniques**: Among the many signal improvement techniques available, one of the most commonly researched in the context

of wearable communications is the use of a diversity configuration at the receiver (RX). Space, time, frequency and polarization diversity methods are often utilised with the aim of providing partially de-correlated signal versions at the RX. If the diversity branches are uncorrelated and subject to received signals with comparable mean levels, then it is expected that the combined signal will provide a higher signal level compared to the case when only one branch is used.

1.2 Challenges and Motivations

The characteristics of wearable communications channels have been previously studied for different operating frequencies, types of antenna, multipath environments, user movements and wearable node locations [18–23]. The decomposition of the received signal into its multipath and shadowing components is common amongst all the analyses presented in [18–23]. However, although this step may simplify the analysis of the channel data, in some respects it seems an unnatural approach as in reality both multipath and shadowing co-exist and consequently affect wearable communications channels simultaneously.

While these studies have provided important insights into different aspects of signal propagation in wearable communications channels, it is difficult to see how the combined multipath and shadowing (i.e. composite fading) affect wearable communications channels. Furthermore, it is required to determine an appropriate smoothing window size for the computation of the local mean signal when decomposing the received signal, which can fundamentally affect the parameter estimation process and any inference made from the channel data. To this end, in [24, 25], composite fading models have been utilised to characterize the fading behaviour experienced in wearable communications channels. However, for both composite fading models, it was not possible to obtain closed-form expressions for their PDFs and thus they must be computed numerically. Consequently, they are not convenient for the analytical calculations associated with the performance

evaluation of wearable communications systems. These issues will be addressed in more detail in Chapters 3 and 4.

Over the last few decades, in the context of wearable communications, micro-diversity[1] has been commonly studied using multiple co-located antennas positioned at a base station with the aim of mitigating the detrimental effects of multipath fading [26–31]. In contrast, macro-diversity[2], which has seen a lesser interest, has been investigated using spatially separated antennas on the human body to overcome shadowing [32, 33]. When combining the received signal for both micro- and macro-diversity, the majority of these studies have considered only the pure selection combining (PSC), equal gain combining (EGC) and maximal ratio combining (MRC) techniques.

Although these combining schemes provide a worthwhile performance, they increase the implementation complexity compared to switched diversity techniques such as switch-and-stay combining (SSC), switch-and-examine combining (SEC) and SEC with post-examining selection (SECps), as they may require continuous and simultaneous knowledge of all of the possible signal paths. Consequently, they can be both time- and power-consuming compared to switched diversity schemes and thus may be impractical for implementation in wearable systems which favour low complexity, low cost and ultra-low power architecture [34, 35]. Additionally, there exist many drawbacks to constructing diversity systems designed to be worn on the human body, especially when compared to integrating the technology into a local base station or using combining opportunities offered by multiple base stations. These include potential obtrusion to the user, the additional weight added to the wearable systems associated circuity and enclosures and also the extra drain on battery life. These issues will form the basis of work presented in Chapters 4 and 5.

[1]The antennas are typically positioned within a single base station with a separation distance of the order of (or shorter than) the signal wavelength so that they are expected to experience different multipath.

[2]The antennas are often located in different, spatially separated base stations for which the spacing is much longer than signal wavelength so that they are expected to experience different shadowing.

Motivated by all of these issues, this thesis first proposes some novel composite fading models which benefit from convenient and tractable closed-form expressions for many of the fundamental statistics of interest. These new formulations are not only straightforward to handle both analytically and numerically, but most importantly flexible enough to accurately characterize the composite fading behaviour experienced in wearable communications channels. To overcome the deleterious effects of multipath and shadowing in wearable communications, switched combining based diversity techniques are investigated. Important metrics, such as the switching threshold, achievable diversity gain (DG), number of path examinations and number of the path switches, are established. Additionally, for the first time, these channels are modelled using diversity specific statistical models.

1.3 Objectives

The main objectives of this thesis are highlighted as follows:

- To propose new and general composite fading models, which are more convenient to handle both analytically and numerically than existing composite fading models, namely $\mathcal{F}$, κ-μ / inverse gamma and κ-μ / inverse gamma composite fading models.

- To characterize the behaviour of the combined multipath and shadowing (i.e. composite fading) observed in wearable communications channels using the newly proposed fading models.

- To validate the generality and utility of the $\mathcal{F}$, κ-μ / inverse gamma and η-μ / inverse gamma composite fading models for the wearable channels.

- To investigate the improvement in signal reliability using multiple antennas at the RX for wearable communications channels by mitigating multipath

fading (i.e. micro-diversity), shadowing (i.e. macro-diversity setup) and both multipath and shadowing (i.e. combined micro- and macro-diversity).

- To analyse the fading observed at the output of diversity combiner for wearable communications systems using diversity specific analytical equations.

1.4 Contributions

This thesis includes three main contributions which are summarized as follows:

1. The behaviour of the composite fading observed in wearable communications channels has been investigated. To this end, a number of novel composite fading models, namely $\mathcal{F}$, κ-μ / inverse gamma and η-μ / inverse gamma composite fading models, have been presented according to two key types of propagation geometry, i.e. line-of-sight (LOS) and non-LOS (NLOS). For the $\mathcal{F}$ and κ-μ / inverse gamma composite fading models, due to the simplicity, many of the fundamental statistics of interest, such as the PDFs, CDFs, higher order moments, amount of fading (AF) and MGFs, have been able to be obtained in closed-form expressions. For the η-μ / inverse gamma composite fading model, closed-form expressions for the PDF, higher order moments and AF are presented along with important analytical expressions for the corresponding CDF and MGF. The generality and suitability of the new models for characterizing composite fading channels are demonstrated through extensive field measurements. For all of measurements, LOS and NLOS channel conditions are considered. Then these three composite fading models are compared with other existing composite fading models and the best fading model among them is determined using the second-order Akaike information crieterion (AICc).

2. For the first time, the potential improvement in signal reliability for wearable communications channels has been investigated using a switched combining based micro-diversity and a switched combining based macro-diversity.

Three different switched diversity techniques are considered, namely SSC, SEC and SECps. These combining schemes are chosen as they are likely to be more suited for use in wearable systems compared to more traditional combining schemes such as MRC due to their lower complexity of implementation. The analysis of the performance/complexity trade-off has been empirically evaluated. The fading observed at the output of the switched combining based micro-diversity has been statistically characterized using diversity specific analytical equations developed for independent and identically distributed (i.i.d.) Nakagami-m multipath fading channels. On the other hand, the fading behaviour at the output of the switched combining based macro-diversity is statistically characterized using diversity specific analytical equations developed under the assumption of independent and non-identically distributed (i.n.i.d.) Nakagami-m shadowing channels. The resistor-average distance (RAD) has been evaluated to provide a quantitative measure of the goodness-of-fit of the theoretical PDFs with the measured data.

3. While micro-diversity and macro-diversity may provide a worthwhile improvement in signal reliability for channels which suffer from either multipath or shadowing respectively, their use in isolation may not be sufficient to overcome the combined channel impairments induced by the simultaneous existence of multipath and shadowing. Therefore, for the first time, this thesis also investigates the further improvement in signal reliability for wearable communications systems using a combined micro- and macro-diversity configuration in which MRC and SECps schemes are considered in the micro-diversity and macro-diversity stages respectively, i.e. a combined MRC-SECps system. The performance of a combined micro- and macro-diversity system has been empirically evaluated and compared.

1.5 Thesis Outline

The thesis consists of seven chapters which are outlined as follows.

Chapter 2 provides an overview of the relevant literature review and background knowledge required to understand the topics covered in this thesis. For example, it explains the path loss, multipath and shadowing phenomena, which are generally responsible for shaping the characteristics of the received signal in wireless communications channels. This chapter also introduces some of the existing composite fading models available in the literature. The operation principle of PSC, EGC, MRC, SSC, SEC and SECps schemes, which are prevalently used in diversity reception for the improvement of signal reliability, is described. The concepts of DG, correlation and power imbalance are also introduced for analysing the performance of diversity systems while the RAD and AICc are reviewed for the evaluation of goodness-of-fit and model selection respectively.

Chapter 3 introduces the κ-μ / inverse gamma composite fading model which is proposed for the LOS wearable channel conditions. It also demonstrates the versatility of the κ-μ / inverse gamma composite fading model through reduction to some special cases which coincide with existing well-known distributions as well as its ability to approximate other more complicated composite fading models. The utility of the κ-μ / inverse gamma composite fading model for the LOS wearable communications channels is validated using an exhaustive set of field measurements coverage a wide range of environments. Furthermore, the best model between the κ-μ / inverse gamma composite fading model and other composite fading models associated with the κ-μ fading model is selected using the AICc analysis.

In Chapter 4, the $\mathcal{F}$ and η-μ / inverse gamma composite fading models are proposed for the NLOS wearable channel conditions. Similar to Chapter 3, the flexibility of the $\mathcal{F}$ and η-μ / inverse gamma composite fading models are demonstrated using some special cases and approximations of other composite fading models. It introduces some wearable field measurements conducted in the same

environments described in Chapter 3 which are employed to validate the suitability of the $\mathcal{F}$ and η-μ / inverse gamma composite fading models for the NLOS wearable communications channels. They are compared with other composite fading models associated with the NLOS channel conditions and the best model amongst them is determined using the AICc.

In Chapter 5, micro-diversity and macro-diversity configurations are considered to investigate the potential improvement in signal reliability for wearable communications channels through the mitigation of multipath and shadowing respectively. For both the micro-diversity and macro-diversity systems, SSC, SEC and SECps schemes are considered when combining the received signal. The performance of micro-diversity and macro-diversity combining is evaluated using DG along with an analysis of the correlation and power imbalance between diversity branches (or base stations). Furthermore, for both the micro-diversity and macro-diversity configurations, the fading behaviour observed at the output of the diversity combiner is statistically characterized using the diversity specific analytical equations. The RAD is evaluated to provide a quantitative measure of the goodness-of-fit for diversity combiners with the measurement data.

Chapter 6 investigates the further improvement in signal reliability which can be achieved by using both micro- and macro-diversity based combining compared either technique in isolation. To investigate this, the results of a comprehensive measurement campaign performed in both indoor and outdoor environments are presented. To mitigate the concurrent multipath and shadowing, an MRC scheme is considered in the micro-diversity stage, whereas an SECps scheme is utilised in macro-diversity stage (i.e. a combined MRC-SECps system). Similar to the approach used in Chapter 5, the correlation and power imbalance are calculated and the performance of a combined micro- and macro-diversity system is empirically evaluated using DG.

Chapter 7 summarizes some important conclusions obtained from this thesis and also gives some possible avenues for future work.

Chapter 2

Background and Literature Review

In traditional wireless communications, radio signal propagation is characterized by three statistically independent phenomena, namely path loss, multipath fading and shadowing. To help with the understanding of the work presented in this thesis, in this Chapter, the necessary background information on these mechanisms are presented along with some of the relevant literature. A diversity configuration is one of the most common methods utilised in wireless communications to mitigate fading and improve signal reliability. Accordingly, this Chapter describes the operation principle of a number of different diversity combining schemes along with the introduction of the concepts of DG, correlation and power imbalance which are commonly used to analyse the performance of diversity systems. This Chapter also introduces the RAD and AICc which are used in this thesis to evaluate the goodness-of-fit and to perform model selection respectively.

2.1 Path Loss

The path loss is a measure of the signal attenuation between the transmitter (TX) and RX as a function of the separation distance. It is commonly modelled using

the classical power law in logarithmic form as follows [36]

$$P\,[\mathrm{dB}] = P_0 + 10\,n_e \log_{10}\left(\frac{d}{d_0}\right) \tag{2.1}$$

where P_0 represents the path loss at the reference distance (d_0) and n_e is the path loss exponent which indicates the rate at which the path loss increases with the separation distance (d) between the TX and RX. There exist a number of studies on path loss in context of wearable communications [37–41]. In the majority of these studies, it has been observed that the path loss exponent for the LOS walking scenarios within the indoor environments was smaller than that associated with isotropic radiation in free space ($n_e = 2$) due to the waveguide effect which can be present within indoor environments [37–40]. Furthermore, a multi-slope path loss model has been proposed in [41] by combining the main propagation mechanism responsible for carrying signal around the human body (i.e. the creeping wave) with the traditional path loss formula given in (2.1).

2.2 Multipath Fading

Multipath fading is mainly caused by the constructive and destructive interference between two or more versions of the transmitted signal over short distances. There exist a number of different models used to represent the multipath fading behaviour depending on the nature of the radio propagation environment, namely Rayleigh [42, 43], Rice (Nakagami-n) [44, 45] and Nakagami-m [46, 47] fading models. More recently, new and more general fading models, namely κ-μ and η-μ fading models [48], have been used to describe the random fluctuation of the received signal envelope.

2.2.1 Rayleigh Fading

The Rayleigh distribution is commonly used to model the multipath fading signal when no direct signal path exists between the TX and RX (i.e. NLOS channel

conditions). The PDF of the fading signal envelope, R, in a Rayleigh fading channel can be expressed as

$$f_R(r) = \frac{2r}{\Omega} \exp\left(-\frac{r^2}{\Omega}\right) \tag{2.2}$$

where $\mathbb{E}[R^2] = \Omega$ is the mean power with $\mathbb{E}[\cdot]$ denoting statistical expectation. The Rayleigh distribution has previously found limited success in the characterization of multipath fading observed in NLOS wearable communications channels [49].

2.2.2 Rice Fading

The Rice distribution is often used to model the multipath fading signal when there exists a direct signal path between the TX and RX (i.e. LOS channel conditions) as well as a scattered signal contribution. The PDF of the fading signal envelope, R, in a Rice fading channel can be written as

$$f_R(r) = \frac{r}{\sigma^2} \exp\left(-\frac{\delta^2 + r^2}{2\sigma^2}\right) I_0\left(\frac{\delta r}{\sigma^2}\right) \tag{2.3}$$

where $I_0(\cdot)$ represents the modified Bessel function of the first kind with order zero [50, Eq. (9.6.16)], δ and σ are the non-centrality and scaling parameters, respectively. From the parameters δ and σ, the well-known K factor can be obtained, which is defined as the ratio between the power in the dominant component (δ^2) and the power in the scattered component ($2\sigma^2$), i.e. $K = \delta^2/2\sigma^2$. The Rice distribution in (2.3) degenerates to the Rayleigh distribution given in (2.2) when there exists no dominant signal component (i.e. $\delta = 0$). When either a direct signal path (i.e. LOS), a dominant signal path created by a strong specular reflection or a dominant signal path induced by diffraction around the human body exists in wearable on-body communications channels, the Rice distribution has successfully described the random fluctuation of the received signal [51, 52].

2.2.3 Nakagami-m Fading

The Nakagami-m fading model is universally associated with multipath fading signal in NLOS channel conditions. It is well-known that the sum of m i.i.d. Rayleigh fading signals follows the Nakagami-m distribution. The corresponding PDF of the fading signal envelope, R, over a Nakagami-m fading channel can be expressed as

$$f_R(r) = \frac{2m^m r^{2m-1}}{\Gamma(m)\,\Omega^m} \exp\left(-\frac{mr^2}{\Omega}\right) \tag{2.4}$$

where $\Gamma(\cdot)$ the gamma function [53, Eq. (8.310.1)], m is the fading severity parameter ($m \geq 0.5$) and Ω is the mean power. It includes as special cases a number of other well-known distributions such as one-sided Gaussian ($m = 0.5$) and Rayleigh ($m = 1$) [47]. The Nakagami-m distribution has the merit of being able to model fading which is worse than Rayleigh (i.e. $0.5 \leq m < 1$).

There exist a number of studies on characterizing the multipath fading experienced in wearable communications channels using the Nakagami-m distribution [21, 51, 52, 54]. For example, in [54], an extensive set of wearable on-body channel measurements were performed at 2.48 GHz for two user states (i.e. stationary and mobile) within three different indoor environments. Here, the TX was positioned at the test subject's left waist and the RX was alternated between seven different body locations, namely right head, left head, front-right chest, front-left chest, front-right wrist, front-right ankle and back-right chest. It was found that the Nakagami-m distribution was chosen as the optimum model to describe multipath fading for the majority of wearable on-body channels over all the measurement scenarios. Additionally, it was also shown that mobile user scenario has relatively more cases, where the Nakagami-m distribution was selected as the best model, compared to stationary user scenario.

2.2.4 κ-μ Fading

The κ-μ distribution has recently been proposed to represent the random variation of the multipath fading signal under LOS channel conditions [48]. The received signal in a κ-μ fading channel is composed of separable clusters of multipath waves propagating in a homogeneous environment, within which the scattered waves have similar delay times, with the delay spreads of different clusters being relatively large. The power of the scattered waves from the multipath clusters is assumed to be identical whereas the power of the dominant wave within each cluster is assumed to be arbitrary. Given the physical signal model for the κ-μ distribution, the signal envelope, R, can be expressed in terms of the in-phase and quadrature components as

$$R = \sqrt{\sum_{i=1}^{n_s} (I_i + p_i)^2 + (Q_i + q_i)^2} \tag{2.5}$$

where n_s represents the number of clusters of multipath ($n_s > 0$), I_i and Q_i are mutually independent Gaussian random variables with $\mathbb{E}[I_i] = \mathbb{E}[Q_i] = 0$ and $\mathbb{E}[I_i^2] = \mathbb{E}[Q_i^2] = \sigma^2$ with $\mathbb{E}[\cdot]$ denoting statistical expectation while p_i and q_i are the mean values of the in-phase and quadrature components of the multipath cluster i, respectively.

The corresponding κ-μ envelope PDF can be written as follows [48]

$$f_R(r) = \frac{2\mu(\kappa+1)^{\frac{\mu+1}{2}} r^{\mu}}{\kappa^{\frac{\mu-1}{2}} \exp(\mu\kappa)\, \Omega^{\frac{\mu+1}{2}}}, \exp\left(-\mu(\kappa+1)\frac{r^2}{\Omega}\right) I_{\mu-1}\left(2\mu\sqrt{\kappa(\kappa+1)}\frac{r}{\sqrt{\Omega}}\right) \tag{2.6}$$

where $I_v(\cdot)$ is the modified Bessel function of the first kind and order v [50, Eq. (9.6.20)]. In terms of its physical interpretation, $\kappa > 0$ is the ratio of the total power of the dominant components ($\delta^2 = \sum_{i=1}^{n_s} p_i^2 + q_i^2$) to the total power of the scattered waves ($2\mu\sigma^2$) while μ is related to the number of multipath clustering, with $2\sigma^2$ denoting the power of the scattered waves in each of the clusters. In this model, the mean signal power is given by $\mathbb{E}[R^2] = \Omega = \delta^2 + 2\mu\sigma^2$. The

κ-μ distribution is an extremely generalized fading distribution and includes as special cases all of the aforementioned distributions, such as one-sided Gaussian, Rayleigh, Rice and Nakagami-m distributions [48].

The κ-μ fading model has relatively recently been utilised to characterize the multipath fading behaviour experienced in wearable off-body communications channels at 2.45 GHz [26]. The κ-μ distribution was found to provide the best fit to wearable channel data for an indoor sweep and search scenario for fire and rescue personnel, suggesting that wearable communications channels may be more appropriately modelled by a clusterised signal reception model. This also indicates that there may persist a signal component which predominates over all of the others within each of these clusters.

2.2.5 η-μ Fading

The η-μ distribution has recently been proposed to represent the random variation of the multipath fading signal under NLOS channel conditions [48]. The received signal in an η-μ fading channel is composed of clusters of multipath waves propagating in a non-homogeneous environment, within which the scattered waves have similar delay times, with the delay spreads of different clusters being relatively large. As shown in Table 2.1, the η-μ distribution may appear in two different formats according to two corresponding physical models. In *Format* 1, the in-phase and quadrature components of the fading signal within each cluster are assumed to be independent from each other and to have different power. On the other hand, in *Format* 2, the in-phase and quadrature components of the fading signal within each cluster are assumed to be correlated with each other and to have identical power. Given the physical signal model for the η-μ distribution, the signal envelope, R, can be expressed in terms of the in-phase and quadrature components as

$$R = \sqrt{\sum_{i=1}^{n_s} I_i^2 + Q_i^2} \tag{2.7}$$

Table 2.1: Summary of two different formats for the $\eta - \mu$ distribution [48]

	***Format* 1**	***Format* 2**
Physical Model	In-phase and quadrature components of the fading signal within each multipath cluster are assumed to be independent to each other and have different powers.	In-phase and quadrature components of the fading signal within each multipath cluster are assumed to have identical powers and to be correlated to each other.
η	$0 < \eta < \infty$, the scattered wave power ratio between the in-phase and quadrature components of each cluster of multipath	$-1 < \eta < 1$, the correlation coefficient between the scattered wave in-phase and quadrature components of each cluster of multipath
h	$h = \frac{2+\eta^{-1}+\eta}{4}$	$h = \frac{1}{1-\eta^2}$
H	$H = \frac{\eta^{-1}-\eta}{4}$	$H = \frac{\eta}{1-\eta^2}$

where n_s denotes the number of clusters of multipath, I_i and Q_i are mutually independent Gaussian random variables with $\mathbb{E}[I_i] = \mathbb{E}[Q_i] = 0$, $\mathbb{E}[I_i^2] = \sigma_I^2$ and $\mathbb{E}[Q_i^2] = \sigma_Q^2$ in *Format* 1 while I_i and Q_i are mutually correlated Gaussian random variables with $\mathbb{E}[I_i] = \mathbb{E}[Q_i] = 0$, and $\mathbb{E}[I_i^2] = \mathbb{E}[Q_i^2] = \sigma^2$ in *Format* 2.

For both formats, the corresponding η-μ envelope PDF can be expressed as follows [48]

$$f_R(r) = \frac{4\sqrt{\pi}\,\mu^{\mu+\frac{1}{2}}\,h^{\mu}r^{2\mu}}{\Gamma(\mu)\,H^{\mu-\frac{1}{2}}\Omega^{\mu+\frac{1}{2}}}\,\exp\left(-\frac{2\mu h r^2}{\Omega}\right) I_{\mu-\frac{1}{2}}\left(\frac{2\mu H r^2}{\Omega}\right). \tag{2.8}$$

In terms of its physical interpretation, $\eta = \sigma_I^2/\sigma_Q^2$ (i.e. the scattered wave power ratio between the in-phase and quadrature components of each cluster of multipath) in *Format* 1 whereas $\eta = \mathbb{E}[I_i Q_i]/\sigma^2$ (i.e. the correlation coefficient between the in-phase and quadrature components) in *Format* 2. Accordingly, $h = \frac{2+\eta^{-1}+\eta}{4}$ and $H = \frac{\eta^{-1}-\eta}{4}$ in $Format\,1$ while $h = \frac{1}{1-\eta^2}$ and $H = \frac{\eta}{1-\eta^2}$ in $Format\,2$. Based on this, $Format\,1$ can be obtained from $Format\,2$ and vice versa by using the following relationship $\eta_{Format1} = \frac{1-\eta_{Format2}}{1+\eta_{Format2}}$ or, equivalently by $\eta_{Format2} = \frac{1-\eta_{Format1}}{1+\eta_{Format1}}$ where $0 < \eta_{Format1} < \infty$ in $Format\,1$ and $-1 < \eta_{Format2} < 1$ in $Format\,2$. In this model, the mean signal power is given by $\mathbb{E}[R^2] = \Omega = \mu(1+\eta^{-1})\sigma_I^2 = \mu(1+\eta)\sigma_Q^2$ in *Format* 1 whereas it is given by $\mathbb{E}[R^2] = \Omega = 2\mu\sigma^2$ in *Format* 2.

The η-μ distribution is a general fading distribution and thus contains as special cases other important distributions, such as Rayleigh, Hoyt (Nakagami-q) and Nakagami-m distributions. Unlike the κ-μ distribution, the η-μ distribution has not yet been used to characterize the multipath fading signal observed in wearable communications channels.

2.3 Shadowing

Shadowing is often introduced by topographical elements and the presence of obstructions in propagation path. It is commonly modelled using the lognormal distribution [55–58] whose PDF is given by

$$f_X(x) = \frac{1}{x\sqrt{2\pi s_l^2}} \exp\left[-\frac{(\ln x - a_l)^2}{2s_l^2}\right] \tag{2.9}$$

where a_l and s_l^2 denote the area mean and variance of the distribution (in dB), i.e. $a_l = \mathbb{E}[\ln x]$ and $s_l^2 = \mathbb{V}[\ln x]$ with $\mathbb{V}[\cdot]$ denoting the variance operator. Although the lognormal distribution has found popularity to describe shadowing, it is often not convenient for the analytic calculations associated with the performance evaluation of communications systems. Due to the intractability of the lognormal distribution, the gamma [59] and inverse Gaussian [60] distributions, which can exhibit similar semi-heavy-tailed behaviour, have been proposed as an alternative to the lognormal distribution. These distributions can be respectively expressed as follows

$$f_X(x) = \frac{x^{k-1}}{\theta^k \Gamma(k)} \exp\left(-\frac{k^2}{\theta}\right) \tag{2.10}$$

$$f_X(x) = \sqrt{\frac{\lambda_{ig}}{2\pi}} x^{-\frac{3}{2}} \exp\left[-\frac{\lambda_{ig}(x-\mu_{ig})^2}{2\,\mu_{ig}^2\,x}\right] \tag{2.11}$$

where k and θ represent the shape and scale parameters in (2.10); μ_{ig} and λ_{ig} denote the mean and scale parameters in (2.11).

The lognormal and gamma distributions have been used to describe shadowing

observed in wearable communications channels [61]. Here, the wearable on-body channel measurements were performed at three different frequencies using three different types of antennas for two user states (i.e. stationary and mobile) within a laboratory room. Over all of the cases considered in [61], the Kolmogorov-Smirnov (K-S) test suggests that the both lognormal and gamma distributions have successfully characterized the shadowing behaviour of wearable on-body channels. Nevertheless, it was found that the lognormal distribution provided the best fit for more cases compared to the gamma distribution.

2.4 Composite Fading Channel Models

Composite fading typically occurs due to the interaction of signal components created by the multipath and shadowing phenomena. In reality, both multipath and shadowing can co-exist and affect the wireless communications channel simultaneously. Consequently, to characterize the behaviour of the combined multipath and shadowing (i.e. composite fading), a number of studies have proposed the use of composite fading models for both conventional and emerging communications channels. Not only do composite fading models take into account the simultaneous occurrence of multipath and shadowing but they also help circumvent the requirement to determine an appropriate smoothing window size for the computation of the local mean signal. This is particularly important in the characterization of wireless channels as the choice of smoothing window size will affect the parameter estimation process and any inference made from the channel data.

These composite fading models can be broadly divided into two different types according to the condition of shadowing as shown in Table 2.2. The first one is *LOS* shadowing where the dominant signal component is shadowed and fluctuates randomly whereas the second one is multiplicative shadowing in which the total power of the dominant component (if present) and scattered signal components are shadowed and vary randomly [62]. Traditionally, composite fading models have considered that the classical fading models, such as Rayleigh, Rice and

Nakagami-m, encounter *LOS* or *multiplicative* shadowing (where relevant) which is assumed to follow the lognormal distribution [63–67]. However, this approach has a significant drawback in which the mathematical form of lognormal-based composite fading models is not convenient for the analytic calculations associated with the performance evaluation of communications systems.

As discussed in Chapter 2.3, the gamma and inverse Gaussian distributions have been proposed as an alternative to the lognormal distribution. The use of these distributions has led to closed-form expressions being obtained for the PDFs of a number of new composite fading models [62, 68–72]. More recently, in accordance with more general multipath fading models, such as the κ-μ and η-μ fading models, new composite fading models have been proposed, namely κ-μ / lognormal [24], shadowed κ-μ [73,74], κ-μ / gamma [75], η-μ / gamma [76,77], κ-μ / inverse Gaussian [78] and η-μ / inverse Gaussian [79]. Nevertheless, among these composite fading models, only a few models have been used to characterize the composite fading signal observed in wearable communications channels [24, 25].

More specifically, in [24], the κ-μ / lognormal shadowed model has been extensively validated through a series of wearable channel measurements (wearable on-body at 2.45 GHz and wearable off-body at 2.42 GHz) which have been performed in an anechoic chamber environment (i.e. less reduced multipath conditions). For the wearable on-body channel measurements, the TX was located on the central-chest region of the test subject while the RX was alternated between the left-waist, right-head, right-wrist and right-knee regions of the test subject. For the wearable off-body channel measurements, the wearable node was positioned on the central-chest region of the test subject. Interestingly, for both wearable on- and off-body channels, it has been shown that resultant dominant components still exist in wearable channels where the user's body obstructed the direct signal path between the TX and RX.

Similarly in [25], the κ-μ / gamma composite fading model has been verified using an extensive wearable off-body channel measurements at 5.8 GHz. Unlike

Table 2.2: Summary of composite fading models which have been presented in the literature.

Model	Proposers	*LOS* shadowing	*Multiplicative* shadowing
Classic	Suzuki [66]	-	Rayleigh + lognormal
	Hansen *et al* [65]	-	Rayleigh + lognormal
	Loo [63]	Rice + lognormal	-
	Corazza *et al* [64]	-	Rice + lognormal
	Tjhung *et al* [67]	-	Nakagami-m + lognormal
	Abdi *et al* [69]	-	Rayleigh + gamma
	Abdi *et al* [62]	Rice + Nakagami-m	-
	Kostic [68]	-	Nakagami-m + gamma
	Eltoft [70]	Rice + inverse Gaussian	-
	Karmeshu *et al* [71]	-	Rayleigh + inverse Gaussian
	Laourine *et al* [72]	-	Nakagami-m + inverse Gaussian
New	Sofotasios *et al* [75]	-	κ-μ + gamma
	Sofotasios *et al* [76]	-	η-μ + gamma
	Zhang *et al* [77]	-	η-μ + gamma
	Sofotasios *et al* [78]	-	κ-μ + inverse Gaussian
	Sofotasios *et al* [79]	-	η-μ + inverse Gaussian
	Cotton [24]	κ-μ + lognormal	-
	Paris [73]	κ-μ + Nakagami-m	-
	Cotton [74]	κ-μ + Nakagami-m	-

the measurements performed in [24], the experiments were conducted in more realistic indoor environments (e.g. a seminar room and an open office area) in which there exist more multipath signal contributions. Here, the wearable node was alternated between three different locations, namely central-chest, central-waist and right-wrist regions of the test subject. Most importantly, in [25], it was shown that the κ-μ / gamma composite fading model outperformed the κ-μ / lognormal shadowed fading model for approximately two-thirds of all the wearable off-body channels. This suggests that it is more appropriate to assume that both the dominant and scattered signal components (i.e. *multiplicative* shadowing) are shadowed together in wearable communications channels.

2.5 Diversity Combining

One well-known method of mitigating the deleterious effects of fading and improving the signal reliability and the performance of wireless systems is to employ diversity reception techniques [80, 81]. While there are many different diversity reception techniques currently in use including time, frequency and polarization techniques, it is spatial diversity which is the most commonly applied as there is no need to increase transmit power or bandwidth [82]. When combining the signals received at multiple spatially separated antennas, two different categories of combining are prevalently used, namely switched combining and gain combining [83]. In general, a better performance can be achieved by gain combining schemes compared to switched combining schemes.

2.5.1 Switched Combining

In the switched combining grouping, which includes PSC and threshold selection combining (TSC) schemes, the RX chooses one of the available diversity paths according to a predefined criterion. A selection process needs to be occur within a time slot which is generally assumed to be in the order of the channel coherence time so that the channel quality stays roughly stationary over a time slot and is independent from one time slot to the next [84]. In a PSC system, the combiner monitors the input signal level of all the diversity paths simultaneously and selects the branch with the highest signal-to-noise ratio (SNR). Thus, for an array consisting of L branches, the PSC output SNR is

$$\gamma_{PSC} = \max\left(\gamma_1, \gamma_2, ..., \gamma_L\right) \tag{2.12}$$

where, γ_L is the input SNR observed in the L^{th} branch of the diversity RX.

Unlike a PSC system, an RX employing a TSC system switches from one branch to another only when the SNR of the currently selected branch falls below the predetermined threshold [83]. This approach has the advantage that the RX

is not needlessly monitoring the SNR of all the diversity paths and switching between branches when the SNR of the currently selected branch is at a level which is acceptable for supporting the desired information recovering capability. A TSC system can be broadly divided into three different schemes, namely SSC, SEC and SECps.

In an SSC scheme, when the SNR of the currently selected branch drops below the predetermined switching threshold the RX simply switches from one branch to another branch and then stays with that branch, irrespective of its channel condition. When the fading observed at each of the branches is assumed to be i.n.i.d. the PDF of the output SNR at an L-branch SSC combiner can be written as follows [85]

$$f_{\mathrm{SSC}}(\gamma) = \begin{cases} \displaystyle\sum_{i=0}^{L-1} \left(\sum_{j=0}^{L-1} \frac{1}{F_j(\gamma_T)} \right)^{-1} f_i(\gamma), & \gamma < \gamma_T \\ \displaystyle\sum_{i=0}^{L-1} \left[\pi_i + \left(\sum_{j=0}^{L-1} \frac{1}{F_j(\gamma_T)} \right)^{-1} \right] f_i(\gamma), & \gamma \geq \gamma_T \end{cases} \tag{2.13}$$

where L is the number of branches, γ_T is the fixed switching threshold, $f_i(\cdot)$ and $F_i(\cdot)$ denote PDF and CDF for i^{th} branch, respectively, and π_i is the probability that the i^{th} base station is used in the SSC scheme, which can be obtained using an L-state Markov chain such that

$$\pi_i = \left(\sum_{j=0}^{L-1} \frac{1}{F_j(\gamma_T)} \right)^{-1} \frac{1}{F_i(\gamma_T)}, i = 0, 1, \ldots, L-1. \tag{2.14}$$

With an SEC scheme, when the received SNR at the currently selected branch falls below the predetermined switching threshold the RX switches from the current branch to another branch and examines its SNR. If it is not above the predetermined switching threshold, the RX switches to another branch and examines its SNR again. The RX repeats this process until either it finds an acceptable branch whose SNR is above the switching threshold or determines that all

branches are not acceptable. In the latter case, it usually uses the last examined branch. For i.n.i.d. fading at each of the branches, the PDF of the output SNR at an L-branch SEC combiner can be expressed as [85]

$$f_{\mathrm{SEC}}(\gamma) = \begin{cases} \displaystyle\sum_{i=0}^{L-1} \chi_i \left[\prod_{k=0,k\neq i}^{L-1} F_k(\gamma_T) \right] f_i(\gamma), & \gamma < \gamma_T \\ \displaystyle\sum_{i=0}^{L-1} \left[\sum_{j=0}^{L-1} \chi_{[(i-j)]_L} \prod_{k=0}^{j-1} F_{[(i-j+k)]_L}(\gamma_T) \right] f_i(\gamma), & \gamma \geq \gamma_T \end{cases} \tag{2.15}$$

where $[(u)]_c$ denotes u modulo c and χ_i is the stationary distribution of an L-state Markov chain and is defined as follows

$$\chi_i = \left[\sum_{j=0}^{L-1} \frac{F_{L-1}(\gamma_T)\left(1 - F_j(\gamma_T)\right)}{F_j(\gamma_T)\left(1 - F_{L-1}(\gamma_T)\right)} \right]^{-1} \frac{F_{L-1}(\gamma_T)\left(1 - F_i(\gamma_T)\right)}{F_i(\gamma_T)\left(1 - F_{L-1}(\gamma_T)\right)}. \tag{2.16}$$

When the received SNR at the currently selected branch falls below the predetermined switching threshold an RX utilising an SECps scheme switches from the current branch to another branch and examines its SNR in exactly the same manner as an SEC scheme. However, when there is no acceptable branch available after examining all branch, the SECps scheme selects the best performing branch, i.e. the branch with the highest SNR, instead of the last examined one. For an L-branch SECps system in which the SNR is i.n.i.d. at each of the L branches, the PDF of the output SNR can be expressed as [86]

$$f_{\mathrm{SECps}}(\gamma) = \begin{cases} \displaystyle\sum_{i=1}^{L} \left[\prod_{j=1,j\neq i}^{L} F_j(\gamma) \right] f_i(\gamma), & \gamma < \gamma_T \\ \displaystyle\sum_{i=1}^{L} \left[\prod_{j=1}^{i-1} F_j(\gamma_T) \right] f_i(\gamma), & \gamma \geq \gamma_T. \end{cases} \tag{2.17}$$

2.5.2 Gain Combining

In the gain combining grouping, the output of combiner is a linear combination of the signals received by all of the diversity paths. This category of combining techniques includes EGC and MRC schemes. In an MRC scheme, the signals from all of the L branches are co-phased to provide coherent voltage addition and weighted according to their individual signal voltage to noise power ratio to provide the optimal SNR before being summated. If it is assumed that noise power is equal on all branches then the output SNR of the L branches is

$$\gamma_{MRC} = \sum_{l=1}^{L} \gamma_l. \tag{2.18}$$

In certain cases, it is not convenient to provide the variable weighting capability required for an MRC scheme. In such cases, the branch weights are all set to unity and the signals form each branch are co-phased with unity gain to provide EGC diversity combining. Thus the EGC output SNR is

$$\gamma_{EGC} = \frac{\sum_{l=1}^{L} \sqrt{\gamma_l}}{\sqrt{L}}. \tag{2.19}$$

2.6 Diversity Gain

The DG is commonly utilised to evaluate the potential improvement in the received signal reliability that could be obtained using diversity techniques. This is defined as the difference in signal level at the output of the diversity combiner and the signal level received at the reference RX for a given probability or signal reliability [87] and can be expressed as follows

$$\mathrm{DG_{dB}} = 20 \log_{10} \left(\frac{F^{-1}_{\gamma_{output}}(y)}{F^{-1}_{\gamma_{ref}}(y)} \right) \tag{2.20}$$

where $F^{-1}_{\gamma_{output}}(y)$ and $F^{-1}_{\gamma_{ref}}(y)$ represent the inverse transforms of the empirical CDFs of the diversity combiner output and the reference RX at a cumulative probability of y, respectively.

2.7 Correlation and Power Imbalance

The correlation and power imbalance between diversity branches can affect the achievable DG [87]. For a diversity scheme to be effective, each antenna element should receive statistically independent versions of the transmitted signal (i.e. low correlation) and should have similar average received power (i.e. low power imbalance). The cross-correlation coefficient between the fading envelopes r_1 and r_2 consisting of N samples can be expressed [87]

$$\rho = \frac{\sum_{i=1}^{N} [r_1(i) - \bar{r}_1][r_2(i) - \bar{r}_2]}{\sqrt{\sum_{i}^{N} [r_1(i) - \bar{r}_1]^2} \sqrt{\sum_{i}^{N} [r_2(i) - \bar{r}_2]^2}}. \tag{2.21}$$

where i is the instantaneous sample value, $\bar{r}_1$ and $\bar{r}_2$ are the respective means of the fading envelopes. The power imbalance is defined as the difference between the mean signal levels of two different branches [87].

2.8 Resistor-Average Distance

The Kullback Leibler divergence (KLD) is the most frequently used information-theoretic distance measure from a viewpoint of theory [88]. Due to its geometric importance, computational and theoretical advantages, the KLD is more attractive compared to other distance measures such as the Chernoff and Bhattacharyya distances. Nevertheless, due to its lack of symmetry, the KLD becomes a nuisance in applications. Consequently, a symmetric version of the KLD, namely RAD, has been proposed [88]. Unlike the KLD, the RAD satisfies the triangle inequality

and thus is a true distance metric. The RAD can be defined as follows [88]

$$\mathrm{RAD}\left(f_1, f_2\right) = \left(\frac{1}{\mathrm{KLD}\left(f_1, f_2\right)} + \frac{1}{\mathrm{KLD}\left(f_2, f_1\right)}\right)^{-1} \tag{2.22}$$

where $\mathrm{KLD}\left(f_1, f_2\right) = \int_{-\infty}^{\infty} f_1(x) \log_2\left(\frac{f_1(x)}{f_2(x)}\right) \mathrm{d}x$ with $f_1\left(x\right)$ and $f_2\left(x\right)$ denoting the true PDF of the measurement data and test PDF [i.e. the approximated PDF of $f_1\left(x\right)$], respectively [89].

2.9 Second-order Akaike Information Criterion

The AICc is one of the most common methods employed in statistics to perform model selection. The AICc can be defined as follows [90]

$$\mathrm{AIC_C} = -2\ln\left(l\left(\phi|data\right)\right) + 2n_p + \frac{2n_p\left(n_p+1\right)}{N-n_p-1} \tag{2.23}$$

where $\ln\left(l\left(\phi|data\right)\right)$ is the value of the maximized log-likelihood over the unknown parameter ϕ of the model given the data, n_p is the number of estimated parameters available in the model, and N is the sample size. In (2.23), the first term indicates that better models have a lower AICc because the log-likelihood reflects the overall fit of the model to the data while the second term penalizes additional parameters ensuring that the model, which best fits the data with the least number of parameters, is selected [90].

Chapter 3

A New Composite Fading Model for LOS Wearable Channels

When the optical LOS path between the TX and RX exists the wearable link is mainly supported by a direct LOS signal path and dominant signal paths created by strong specular reflections. As these travel from the TX to RX, the multipath clusters are also created by signal components being reflected and scattered by the human body and local surroundings. In this case, it is more appropriate to assume that both the dominant and scattered signal components exist and its mean power is subjected to shadowing. In order to investigate the behaviour of the composite fading signal observed in LOS wearable communications channels, this Chapter presents the κ-μ / inverse gamma composite fading model along with its key statistics such as the PDF, CDF, MGF, higher order moments and AF. The utility of the κ-μ / inverse gamma composite fading model is validated using an extensive set of field measurements. Furthermore, in this Chapter, the best model between the κ-μ / inverse gamma composite fading model and other composite fading models associated with the κ-μ fading model is evaluated using the AICc analysis.

3.1 Introduction

The κ-μ distribution was recently proposed to represent the random variation of the multipath fading signal under LOS channel conditions [48]. It is an extremely generalized fading distribution which includes as special cases other important distributions, such as one-sided Gaussian, Rayleigh, Rice and Nakagami-m distributions. Subsequently, new composite fading models based on the κ-μ distribution have been proposed [24, 73–75, 78]. From among these, the κ-μ / lognormal [24] and the κ-μ / gamma [25] composite fading models have been utilised to characterize the composite fading signal experienced in wearable communications channels. However, unfortunately, their PDFs are not available in closed-form and they must be computed numerically. Similarly, there exists no closed-form for the PDF of the κ-μ / inverse Gaussian composite fading model proposed in [78]. Consequently, they are not convenient for the analytical calculations required to evaluate the performance of wireless systems operating in their respective fading channels.

Closed-form expressions for the shadowed κ-μ composite fading model are available in [73, 74]. This model assumes that the resultant dominant component of a κ-μ fading signal is subject to random variation induced by a Nakagami-m random variable. This statistical model has recently been utilised to characterize the composite fading experienced in wireless communications channels, particularly in device-to-device (D2D) communications channels [74]. Nevertheless, in [25], it was shown that the κ-μ / gamma composite fading model (i.e. *multiplicative* shadowing) outperformed the κ-μ / lognormal shadowed model (i.e. *LOS* shadowing) for wearable communications channels, which suggests that it is more realistic to assume that both the dominant and scattered signal components are shadowed together in wearable communications channels (i.e. *multiplicative* shadowing). Accordingly, a new composite fading model, namely κ-μ / inverse gamma composite fading model, is proposed in this Chapter. This has led to several novel contributions which are summarized as follows

- The PDF, CDF, MGF, higher order moments and AF of the κ-μ / inverse gamma composite fading model have been obtained in convenient closed-form expressions.

- The generality of the κ-μ / inverse gamma composite fading model has been demonstrated. A number of distributions which appear as special cases and the ability to approximate other composite fading models are highlighted.

- An important empirical validation of the κ-μ / inverse gamma composite fading model for use in wearable communications channels is performed.

- Using the AICc, it is also shown that this new model is regularly selected as the most likely candidate model compared to other composite fading distributions which are based on the κ-μ fading, e.g. κ-μ / lognormal, κ-μ / gamma and shadowed κ-μ models.

3.2 Fundamental Statistics of the κ-μ / Inverse Gamma Composite Fading Model

3.2.1 Signal Model

Similar to the physical signal model proposed for the κ-μ fading channel given in [48], the received signal in a κ-μ / inverse gamma composite fading channel is composed of separable clusters of multipath in a homogeneous environment. The power of the scattered waves from the multipath clusters is assumed to be identical whereas the power of the dominant wave within each cluster is assumed to be arbitrary. Unlike the κ-μ fading channel, however, in the κ-μ / inverse gamma composite fading channel, the mean power of the multipath waves (i.e. both the dominant and scattered waves) is randomly fluctuated due to shadowing. Therefore the composite signal envelope, R, in a κ-μ / inverse gamma composite fading

channel can be expressed in terms of the in-phase and quadrature components as

$$R = \sqrt{\sum_{i=1}^{n_s} A(I_i + p_i)^2 + A(Q_i + q_i)^2} \tag{3.1}$$

where n_s represents the number of clusters of multipath, I_i and Q_i are mutually independent Gaussian random variables with $\mathbb{E}[I_i] = \mathbb{E}[Q_i] = 0$ and $\mathbb{E}[I_i^2] = \mathbb{E}[Q_i^2] = \sigma^2$ while p_i and q_i are the mean values of the in-phase and quadrature components of the multipath cluster i, respectively. In (3.1), A denotes an inverse gamma random variable[1] with the shape parameter m_s and scale parameter m_s/Ω_s where Ω_s is set equal to unity (i.e. $\Omega_s = 1$) whose PDF can be written as follows

$$f_A(\alpha) = \frac{{m_s}^{m_s}}{\Gamma(m_s)\,\alpha^{m_s+1}} \exp\left(-\frac{m_s}{\alpha}\right). \tag{3.2}$$

3.2.2 PDF and CDF

The PDF of the composite signal envelope in a κ-μ / inverse gamma composite fading channel, R, can be determined by averaging the infinite integral of the conditional probability density of the κ-μ fading process with respect to the random variation of the mean signal power, A, as follows

$$f_R(r) = \int_0^\infty f_{R|A}(r|\alpha) f_A(\alpha)\,\mathrm{d}\alpha \tag{3.3}$$

where, using the signal model given in (3.3), this insinuates that

$$f_{R|A}(r|\alpha) = \frac{2\mu\, r^\mu}{\kappa^{\frac{\mu-1}{2}} \exp(\mu\kappa)} \left(\frac{\kappa+1}{\alpha\,\Omega}\right)^{\frac{\mu+1}{2}} \exp\left(-\frac{\mu(\kappa+1)r^2}{\alpha\,\Omega}\right) I_{\mu-1}\left(2\mu r\sqrt{\frac{\kappa(\kappa+1)}{\alpha\,\Omega}}\right). \tag{3.4}$$

[1]The inverse gamma distribution can exhibit adequate semi heavy-tailed characteristics similar to those observed for the lognormal and gamma distributions and can be efficiently used to describe shadowing [91].

By substituting (3.2) and (3.4) into (3.3), the PDF of the proposed κ-μ / inverse gamma composite fading model can be expressed as follows

$$f_R(r) = \frac{2\mu(\kappa+1)^{\frac{\mu+1}{2}} {m_s}^{m_s} r^{\mu}}{\kappa^{\frac{\mu-1}{2}} \exp(\mu\kappa)\,\Gamma(m_s)\,\Omega^{\frac{\mu+1}{2}}} \int_0^{\infty} \left(\frac{1}{\alpha}\right)^{\frac{2m_s+\mu+3}{2}} \exp\left(-\frac{\mu(\kappa+1)r^2}{\alpha\,\Omega}\right) \times \exp\left(-\frac{m_s}{\alpha}\right) I_{\mu-1}\left(2\mu r\sqrt{\frac{\kappa(\kappa+1)}{\alpha\,\Omega}}\right) \mathrm{d}\alpha. \tag{3.5}$$

Now, performing a simple transformation of variables and applying equation [92, Eq. (2.15.5.4)] along with some algebraic manipulation, (3.5) can be rewritten in closed-form as follows

$$f_R(r) = \frac{2\mu^{\mu}(\kappa+1)^{\mu}(m_s\Omega)^{m_s} r^{2\mu-1}\exp(-\mu\kappa)}{B(m_s,\mu)\left[\mu(\kappa+1)r^2 + m_s\Omega\right]^{m_s+\mu}} {}_1F_1\left(m_s+\mu;\mu;\frac{\mu^2\kappa(\kappa+1)r^2}{\mu(\kappa+1)r^2+m_s\Omega}\right) \tag{3.6}$$

where $B(\cdot,\cdot)$ and ${}_1F_1(\cdot;\cdot;\cdot)$ denote the Beta function a [53, Eq. (8.384.1)] and the Kummer confluent hypergeometric function [53, Eq. (9.210.1)], respectively. Additionally, the corresponding PDF of the instantaneous SNR of the κ-μ / inverse gamma composite fading model is also readily obtained by letting $\gamma = \bar{\gamma}r^2/\Omega$ where $\bar{\gamma} = \mathbb{E}[\gamma]$, yielding

$$f_{\gamma}(\gamma) = \frac{\mu^{\mu}(\kappa+1)^{\mu}(m_s\bar{\gamma})^{m_s}\gamma^{\mu-1}\exp(-\mu\kappa)}{B(m_s,\mu)\left[\mu(\kappa+1)\gamma + m_s\bar{\gamma}\right]^{m_s+\mu}} {}_1F_1\left(m_s+\mu;\,\mu;\,\frac{\mu^2\kappa(\kappa+1)\gamma}{\mu(\kappa+1)\gamma+m_s\bar{\gamma}}\right). \tag{3.7}$$

It is noted that the resultant PDF[1] in (3.7) is functionally equivalent to the singly non-central $\mathcal{F}$ distribution[2] that arises as a result of the ratio of a non-central chi-squared variable and a central chi-squared variable [93].

The CDF of the instantaneous SNR of the κ-μ / inverse gamma composite model can be expressed as follows

[1] It has been analytically confirmed that $\int_0^{\infty} f_{\gamma}(\gamma)\,\mathrm{d}\gamma = 1$.

[2] Using [55, Eq. (2.312)], i.e. $f_X(x) = \bar{\gamma}\, f_{\gamma}(\bar{\gamma}\gamma)$, letting $\gamma(1+\kappa) = x$ and then performing the requisite transformation along with the following substitutions $\mu = d_1/2,\ m_s = d_2/2,\ \mu\kappa = \lambda/2$, the singly non-central $\mathcal{F}$ distribution, $f_x(x)$ with parameters d_1, d_2 and λ, can be obtained.

$$F_{\gamma}(\gamma) = \frac{\mu^{\mu}(\kappa+1)^{\mu}(m_s\bar{\gamma})^{m_s}}{B\left(m_s,\mu\right)\exp\left(\mu\kappa\right)} \int_0^{\gamma} \frac{\gamma^{\mu-1}}{\left[\mu\left(\kappa+1\right)\gamma + m_s\bar{\gamma}\right]^{m_s+\mu}} \times {}_1F_1\left(m_s+\mu;\, \mu;\, \frac{\mu^2\kappa\left(\kappa+1\right)\gamma}{\mu\left(\kappa+1\right)\gamma + m_s\bar{\gamma}}\right) \mathrm{d}\gamma. \tag{3.8}$$

The Kummer confluent hypergeometric function in (3.8) can be expanded in terms of the series representation such that [94, Eq. (07.20.02.0001.01)]

$${}_1F_1\left(a\,;\, b\,;\, z\right) = \sum_{i=0}^{\infty} \frac{(a)_i z^i}{(b)_i\, i!} \tag{3.9}$$

where $(\cdot)_i$ denotes the Pochhammer symbol [94, Eq. (06.10.02.0001.01)]. Consequently, (3.8) can be re-expressed as[1]

$$F_{\gamma}(\gamma) = \sum_{i=0}^{\infty} \frac{(m_s+\mu)_i[\mu\left(\kappa+1\right)]^{\mu+i}\left(\mu\kappa\right)^i\left(m_s\bar{\gamma}\right)^{m_s}}{i!\;(\mu)_i B\left(m_s,\mu\right)\exp\left(\mu\kappa\right)} \int_0^{\gamma} \frac{\gamma^{\mu+i-1}}{\left[\mu\left(\kappa+1\right)\gamma + m_s\bar{\gamma}\right]^{m_s+\mu+i}} \mathrm{d}\gamma. \tag{3.10}$$

With the aid of [53, Eq. (3.194.5)], the CDF of the instantaneous SNR of the κ-μ / inverse gamma model can be obtained as

$$F_{\gamma}(\gamma) = \sum_{i=0}^{\infty} \frac{\exp\left(-\mu\kappa\right)\left(\mu\kappa\right)^i}{i!\;\left(\mu+i\right)B\left(m_s,\mu+i\right)} \left(\frac{\mu\left(\kappa+1\right)\gamma}{m_s\bar{\gamma}}\right)^{\mu+i} \times {}_2F_1\left(m_s+\mu+i,\, \mu+i;\, \mu+i+1;\, -\frac{\mu\left(\kappa+1\right)\gamma}{m_s\bar{\gamma}}\right) \tag{3.11}$$

where ${}_2F_1\left(\cdot,\cdot;\cdot;\cdot\right)$ the Gauss hypergeometric function [53, Eq. (9.111)]. Similarly, the Gauss hypergeometric function in (3.11) can also be expanded in terms of the series representation as follows [94, Eq. (07.23.02.0001.01)]

$${}_2F_1\left(a,b\,;\, c;\, z\right) = \sum_{i=0}^{\infty} \frac{(a)_i(b)_i z^i}{(c)_i\, i!} \text{ for } |\mathrm{z}| < 1 \tag{3.12}$$

$${}_2F_1\left(a,b;c;x\right) = \frac{\Gamma(b-a)\Gamma(c)}{\Gamma(b)\Gamma(c-a)} \sum_{l=0}^{\infty} \frac{(a)_l(a-c+1)_l x^{-l}}{l!(a-b+1)_l(-x)^a} + \frac{\Gamma(a-b)\Gamma(c)}{\Gamma(a)\Gamma(c-b)} \sum_{l=0}^{\infty} \frac{(b)_l(b-c+1)_l x^{-l}}{l!(b-a+1)_l(-x)^b} \text{ for } |\mathrm{z}| \geq 1. \tag{3.13}$$

[1] The order of the summation and integral operators was exchanged according to the dominated convergence theorem.

Consequently, for the case of $m_s\bar{\gamma} > \mu(\kappa+1)\gamma$, (3.13) can be re-written in closed-form as follows

$$F_\gamma(\gamma) = \frac{\exp(-\mu\kappa)}{\mu B(m_s,\mu)}\left(\frac{\mu(\kappa+1)\gamma}{m_s\bar{\gamma}}\right)^{\mu} \times F_{1,1,0}^{2,0,0}\left(\begin{matrix} m_s+\mu,\mu; & -; & -; \\ \mu+1; & \mu; & -; \end{matrix} \frac{\mu^2\kappa(\kappa+1)\gamma}{m_s\bar{\gamma}}, -\frac{\mu(\kappa+1)\gamma}{m_s\bar{\gamma}}\right) \tag{3.14}$$

where $F_{\mathcal{P},\mathcal{Q},\mathcal{S}}^{\mathcal{A},\mathcal{B},\mathcal{C}}\left(\begin{matrix} a_1,\ldots,a_{\mathcal{A}}; & b_1,\ldots,b_{\mathcal{B}}; & c_1,\ldots,c_{\mathcal{C}}; \\ p_1,\ldots,p_{\mathcal{P}}; & q_1,\ldots,q_{\mathcal{Q}}; & s_1,\ldots,s_{\mathcal{S}}; \end{matrix} \cdot,\cdot\right)$ represents the Kampé de Fériet function [95]. On the other hand, for the case of $m_s\bar{\gamma} \leq \mu(\kappa+1)\gamma$, $F_\gamma(\gamma)$ can be expressed in closed-form as

$$F_\gamma(\gamma) = \exp(-\mu\kappa)\,\Psi_1\left(\mu;0;1-m_s,\mu,-\frac{m_s\bar{\gamma}}{\mu(\kappa+1)\gamma},\mu\kappa\right) - \frac{\exp(-\mu\kappa)}{m_s B(m_s,\mu)}\left(\frac{m_s\bar{\gamma}}{\mu(\kappa+1)\gamma}\right)^{m_s}\Psi_1\left(m_s+\mu;m_s;1+m_s,\mu,-\frac{m_s\bar{\gamma}}{\mu(\kappa+1)\gamma},\mu\kappa\right) \tag{3.15}$$

where $\Psi_1(\cdot;\cdot;\cdot,\cdot,\cdot,\cdot)$ denotes the Humbert Ψ_1 function [96].

3.2.3 Higher Order Moments and AF

The higher order moments of the instantaneous SNR of the proposed κ-μ / inverse gamma composite fading model can be expressed using an infinite series expansion of the Kummer confluent hypergeometric function given in (3.9), such that

$$\mathbb{E}[\gamma^n] = \sum_{i=0}^{\infty}\frac{(m_s+\mu)_i[\mu(\kappa+1)]^{\mu+i}(\mu\kappa)^i(m_s\bar{\gamma})^{m_s}}{i!\,(\mu)_i B(m_s,\mu)\exp(\mu\kappa)}\int_0^{\infty}\frac{\gamma^{\mu+n+i-1}}{[\mu(\kappa+1)\gamma+m_s\bar{\gamma}]^{m_s+\mu+i}}\mathrm{d}\gamma. \tag{3.16}$$

With the aid of [53, Eq. (3.251.11)] and using the series representation of the Kummer confluent hypergeometric function given in (3.9), (3.16) can be re-expressed in closed-form as follows

$$\mathbb{E}[\gamma^n] = \left(\frac{m_s\bar{\gamma}}{\mu(\kappa+1)}\right)^n\frac{B(m_s-n,\mu+n)}{\exp(\mu\kappa)\,B(m_s,\mu)}\,{}_1F_1(\mu+n;\mu;\mu\kappa). \tag{3.17}$$

It is recalled here that the AF is often used as a relative measure of the severity of fading encountered in wireless transmission over fading channels and it is defined as AF $= \frac{\mathbb{E}[\gamma^2]}{\mathbb{E}^2[\gamma]} - 1$, [16, Eq. (1.27)] where $\mathbb{E}[\gamma]$ and $\mathbb{E}[\gamma^2]$ denote the first and second moments respectively. By substituting $n = 1$ and $n = 2$ in (3.17), for the case of a κ-μ / inverse gamma composite fading channel, $\mathbb{E}[\gamma]$ and $\mathbb{E}[\gamma^2]$ are simply given as

$$\mathbb{E}[\gamma] = \left(\frac{m_s\bar{\gamma}}{\mu\left(\kappa+1\right)}\right)\frac{B\left(m_s-1,\mu+1\right)}{\exp\left(\mu\kappa\right)B\left(m_s,\mu\right)}\,{}_1F_1\left(\mu+1;\mu;\mu\kappa\right) \tag{3.18}$$

$$\mathbb{E}[\gamma^2] = \left(\frac{m_s\bar{\gamma}}{\mu\left(\kappa+1\right)}\right)^2\frac{B\left(m_s-2,\mu+2\right)}{\exp\left(\mu\kappa\right)B\left(m_s,\mu\right)}\,{}_1F_1\left(\mu+2;\mu;\mu\kappa\right). \tag{3.19}$$

Using the Kummer's transformation [94, Eq. (07.20.17.0013.01)]

$${}_1F_1\left(a;b;z\right) = \exp\left(z\right){}_1F_1\left(b-a;b;-z\right) \tag{3.20}$$

(3.18) and (3.19) can be rewritten as follows

$$\mathbb{E}[\gamma] = \left(\frac{m_s\bar{\gamma}}{\mu\left(\kappa+1\right)}\right)\frac{B\left(m_s-1,\mu+1\right)}{B\left(m_s,\mu\right)}\,{}_1F_1\left(-1;\mu;-\mu\kappa\right) \tag{3.21}$$

$$\mathbb{E}[\gamma^2] = \left(\frac{m_s\bar{\gamma}}{\mu\left(\kappa+1\right)}\right)^2\frac{B\left(m_s-2,\mu+2\right)}{B\left(m_s,\mu\right)}\,{}_1F_1\left(-2;\mu;-\mu\kappa\right). \tag{3.22}$$

Using the special representations of the Kummer confluent hypergeometric function [94, Eq. (07.20.03.0017.01)] [94, Eq. (07.20.03.0018.01)]

$${}_1F_1\left(-1;b;z\right) = 1-\frac{z}{b} \tag{3.23}$$

$${}_1F_1\left(-2;b;z\right) = 1-\frac{2z}{b}+\frac{z^2}{b\left(1+b\right)} \tag{3.24}$$

and carrying out some algebraic manipulation, the AF of the κ-μ / inverse gamma composite fading model can be obtained as

$$AF = \frac{\mu(\kappa+1)^2 + (m_s-1)(1+2\kappa)}{\mu(\kappa+1)^2(m_s-2)}. \tag{3.25}$$

3.2.4 MGF

The MGF of the κ-μ / inverse gamma composite fading model can be derived from (3.7) using an infinite series expansion of the Kummer confluent hypergeometric function given in (3.9)

$$\begin{aligned} M_\gamma(-s) = \sum_{i=0}^{\infty} \frac{(m_s+\mu)_i [\mu(\kappa+1)]^{\mu+i} (\mu\kappa)^i (m_s\bar{\gamma})^{m_s}}{i!\ (\mu)_i B(m_s,\mu)\exp(\mu\kappa)} \\ \times \int_0^{\infty} \frac{\gamma^{\mu+i-1}\exp(-s\gamma)}{[\mu(\kappa+1)\gamma + m_s\bar{\gamma}]^{m_s+\mu+i}} \mathrm{d}\gamma. \end{aligned} \tag{3.26}$$

With the aid of [53, Eq. (3.383.5)], and making use of the generalized Laguerre polynomials [94, Eq. (07.03.02.0001.01)], $L_n^m(z) = \frac{\Gamma(m+n+1)}{\Gamma(m+1)\Gamma(n+1)} {}_1F_1(-n; m+1; z)$; now performing the necessary change of variables and carrying out some long, but basic algebraic manipulation, the corresponding MGF can be obtained as

$$\begin{aligned} M_\gamma(-s) = \sum_{i=0}^{\infty} \frac{(\mu\kappa)^i}{i!\exp(\mu\kappa)} \Bigg[{}_1F_1\left(\mu+i;\, 1-m_s;\, \frac{sm_s\bar{\gamma}}{\mu(\kappa+1)}\right) \\ + \left(\frac{sm_s\bar{\gamma}}{\mu(\kappa+1)}\right)^{m_s} \frac{\Gamma(-m_s)}{B(m_s,\mu+i)} {}_1F_1\left(m_s+\mu+i;\, 1+m_s;\, \frac{sm_s\bar{\gamma}}{\mu(\kappa+1)}\right)\Bigg]. \end{aligned} \tag{3.27}$$

It should be noted that [53, Eq. (3.383.5)] is only valid when $m_s+\mu+i$ is a positive non-integer number, i.e. $m_s+\mu+i \neq \mathbb{N}$. Moreover, in (3.27), m_s must not be a positive integer number as the gamma function is not defined for negative integer arguments. Nonetheless, these potential singularities can be straightforwardly circumvented by introducing infinitely small perturbation terms which can be added to $m_s+\mu+i$ and m_s respectively if required.

By expanding the Kummer confluent hypergeometric function in terms of the series representation given in (3.9) and using the definition of the Humbert Ψ_2 function [96], the MGF of the κ-μ / inverse gamma composite fading model can

be obtained in closed-form as follows

$$M_{\gamma}(-s) = \exp\left(-\mu\kappa\right)\Psi_2\left(\mu;\mu,1-m_s;\mu\kappa,\frac{sm_s\bar{\gamma}}{\mu(\kappa+1)}\right) + \frac{\exp\left(-\mu\kappa\right)}{B(m_s,\mu)}\left(\frac{sm_s\bar{\gamma}}{\mu(\kappa+1)}\right)^{m_s}\Gamma(-m_s)\Psi_2\left(m_s+\mu;\mu,1+m_s;\mu\kappa,\frac{sm_s\bar{\gamma}}{\mu(\kappa+1)}\right). \tag{3.28}$$

3.3 Special Cases and Approximations

The PDF given in (3.6) represents an extremely versatile model which inherits all of the generality of the κ-μ distribution. In (3.6), the m_s parameter controls the amount of the shadowing of the mean signal power. As m_s tends towards zero (i.e. $m_s \to 0$), the dominant (if applicable) and scattered signal components are completely shadowed. On the other hand, as m_s approaches infinity (i.e. $m_s \to \infty$), there is no shadowing present in the channel and thus the mean signal power becomes deterministic. In this case, the κ-μ / inverse gamma PDF given in (3.6) coincides with the κ-μ PDF given in (2.5) as illustrated in Figure 3.1(a). Likewise, by setting $\mu = 1$ and again letting $m_s \to \infty$, the Rice PDF is deduced, where κ becomes equivalent to the Rice K factor. Based on this, the Rayleigh distribution can be readily obtained by setting $\kappa = K = 0$. Similarly, the Nakagami-m distribution can be obtained by letting $m_s \to \infty$ and $\kappa \to 0$ with the μ parameter becoming equivalent to the m parameter of Nakagami-m distribution.

It is worth highlighting that the κ-μ / inverse gamma composite fading model can also be used to provide an accurate approximation of other lognormal- and gamma-based composite fading models. For example, Figure 3.1(b) shows that the κ-μ / inverse gamma (κ, μ, Ω, m_s) composite fading model provides a good match to the Rayleigh / lognormal (a_l, s_l) [65], Rayleigh / gamma (k, θ) [69] and Nakagami-m / gamma (m, k, θ) [68] composite fading models. For this comparison, the m_s and Ω parameters of the κ-μ / inverse gamma composite fading model were estimated from the a_l and s_l parameters of the Rayleigh / lognormal distribution by matching their first and second moments, such that

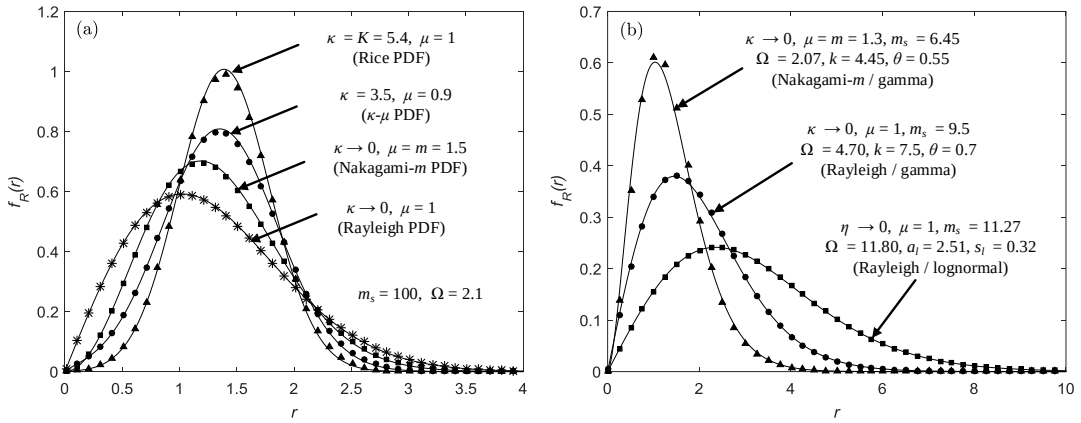

Figure 3.1: PDFs of the κ-μ / inverse gamma composite fading model for (a) special cases with well-known distributions and (b) approximation of other composite fading models.

$$m_s = \frac{2\exp\left(s_l^2\right) - 1}{\exp\left(s_l^2\right) - 1} \tag{3.29}$$

$$\Omega = \frac{\exp\left(a_l + \frac{3}{2}s_l^2\right)}{m_s[\exp\left(s_l^2\right) - 1]} \tag{3.30}$$

Similarly, they were also estimated from the k and θ parameters of the Rayleigh / gamma and Nakagami-m / gamma distributions as follows

$$m_s = k + 2 \tag{3.31}$$

$$\Omega = \frac{k\theta\left(k+1\right)}{m_s}. \tag{3.32}$$

3.4 LOS Wearable Channel Measurements

3.4.1 Measurement Setup

The TX section of the channel measurement system consisted of an ML5805[1], single chip fully integrated Frequency Shift Keyed (FSK) transceiver, manufactured by RF Micro Devices (RFMD). It was configured to transmit a continuous wave signal with a power level of +17.6 dBm at 5.8 GHz. The TX antenna was mounted tangentially with respect to the body surface of an adult male of height

[1] `http://www.datasheets360.com/pdf/6743097625932420971` (visited on 11/06/2017).

1.83 m and mass 73 kg using a small strip of Velcro®. During the measurements, the TX was alternated between two different body locations on the test subject as shown in Figure 3.2(a). These were: the central-chest region at a height of 1.42 m; the central-waist region at a height of 1.15 m. Each of these hypothetical wearable node locations is likely to be used in future wearable systems. For example, the chest region is a suitable location for monitoring electrocardiogram (ECG) while the waist region is a possible mounting point for a gateway node in a BAN.[1] It should be noted that in order to provide a as realistic characterization of the wearable channel as possible, the TX was attached to the test subject's clothing using a small strip of Velcro®. The separation distances between the TX and the body for the two different wearable node locations were 5.8 mm and 7.5 mm for the chest and waist positions, respectively.

It is well-known that an antenna operating in the vicinity of the human body can introduce antenna-body interaction effects such as radiation pattern distortion. Figure 3.2(b) shows the measured azimuthal radiation patterns for the sleeve dipole antenna in free space and positioned at each wearable location. It should be noted that the black arrow in (b) represents the direction that the test subject was facing. Due to the presence of the human body, it is clear that the radiation patterns obtained for both of the wearable locations were significantly distorted when compared to the radiation pattern in free space (particularly in the posterior direction between 90° and 270°). Moreover, it was also observed that the radiation pattern in the anterior facing direction for the chest region was slightly more directional than that for the waist region.

The RX section of the channel measurement system, consisted of an antenna which was mounted vertically on a non-conductive polyvinyl chloride (PVC) stand at an elevation of 1.10 m above the floor level so that the antenna was vertically polarized. The antenna was connected to port 1 of a Rohde & Schwarz ZVB-8 vector network analyzer (VNA) using a low-loss coaxial cable. A pre-measurement

[1]The observed channel characteristics in these scenarios may be present in indoor wearable applications such as patient tracking in hospitals.

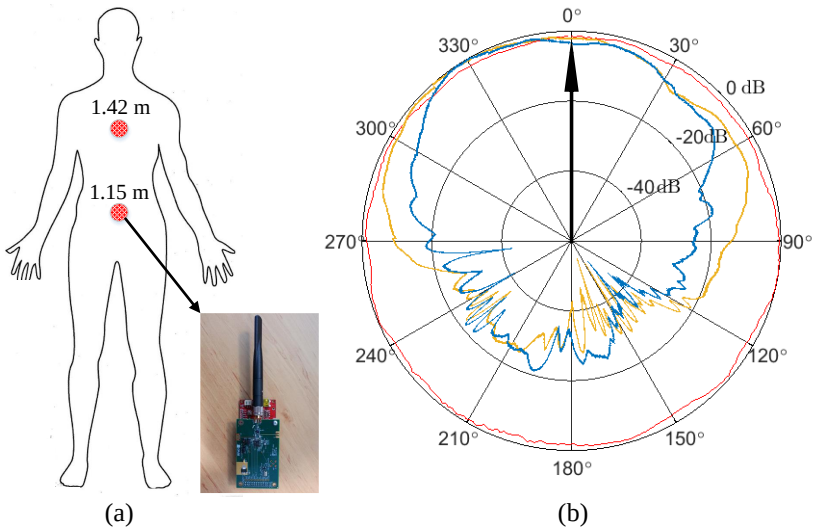

Figure 3.2: (a) Two different hypothetical wearable node locations along with the wearable wireless node used in the measurements: (b) the measured azimuthal radiation patterns for the sleeve dipole antenna in free space (red continuous lines) and situated on the chest (blue continuous lines) and waist (yellow continuous lines) positions.

calibration was performed to reduce the effects of known system based errors using a Rohde & Schwarz ZV-Z513 calibration unit. This also enabled the elimination of the effects of the power amplifier and cable loss. The VNA was configured as a sampling receiver, recording the magnitude of the b_1 wave quantity incident on port 1 with a bandwidth of 10 kHz, which was centred at the operation frequency. The magnitude of the b_1 measurements were automatically collected and stored on a laptop through a local area network (LAN) connection, providing an effective channel sampling frequency of 425.6 Hz (or equivalently a channel sample period of 2.3 ms). The average walking speed estimated from the channel data was 1.19 m/s, which equates to an average Doppler frequency [36] of 23.0 Hz. According to the Nyquist theorem, the required minimum sampling frequency must be at least twice the maximum Doppler frequency to avoid aliasing [97]; therefore, assuming that the human body was the main scattering object in the test environments, the given sampling frequency was more than adequate to characterize the time varying nature of the wearable communications channels studied in this Chapter. The antennas used by both the TX and RX were omnidirectional sleeve

dipole antennas with +2.3 dBi gain (Mobile Mark model PSKN3-24/55S4)[1] in free space.

3.4.2 Environments and Experiments

The experiments were conducted within three different indoor environments, namely a laboratory, a seminar room and an open office area, in order to fully encapsulate variations in room size, materials and furniture. These locations were situated within the Institute of Electronics, Communications and Information Technology (ECIT) at Queen's University Belfast in the United Kingdom. The laboratory (floor area of 4.75 m $\times$ 9.14 m) is situated on the second floor of the ECIT building. As shown in Figure 3.3(a), it contained a number of chairs, boxes, lab equipment, metal cabinets and desks constructed from medium density fibreboard. The laboratory was unoccupied for the duration of the experiments facilitating pedestrian free wearable channel measurements.

The seminar room with a floor area of 7.92 m $\times$ 12.58 m is located on the first floor of the ECIT building. As shown in Figure 3.3(b), the seminar room contained a large number of chairs, desks, a projector and a white board. It also featured an external facing boundary wall constructed entirely from glass with some metallic supporting pillars. Again, the seminar room was unoccupied for the duration of the experiments. The open office area (floor area of 10.62 m $\times$ 12.23 m) situated on the first floor of the ECIT building is illustrated using the red rectangular outline in Figure 3.3(c). The open office area contained a number of soft partitions, cabinets, PCs, chairs and desks. During the channel measurements, one person was working at his desk, as indicated with the red fill in Figure 3.3(c). It is worth noting that all three indoor environments consisted of metal studded dry walls with a metal tiled floor covered with polypropylene-fibre, rubber backed carpet tiles, and metal ceiling with mineral fibre tiles and recessed louvred luminaries suspended 2.70 m above floor level.

[1] `http://www.mobilemark.com/wp-content/uploads/2015/04/antenna-spec-117-pskn3-2400.pdf` (visited on 11/06/2017).

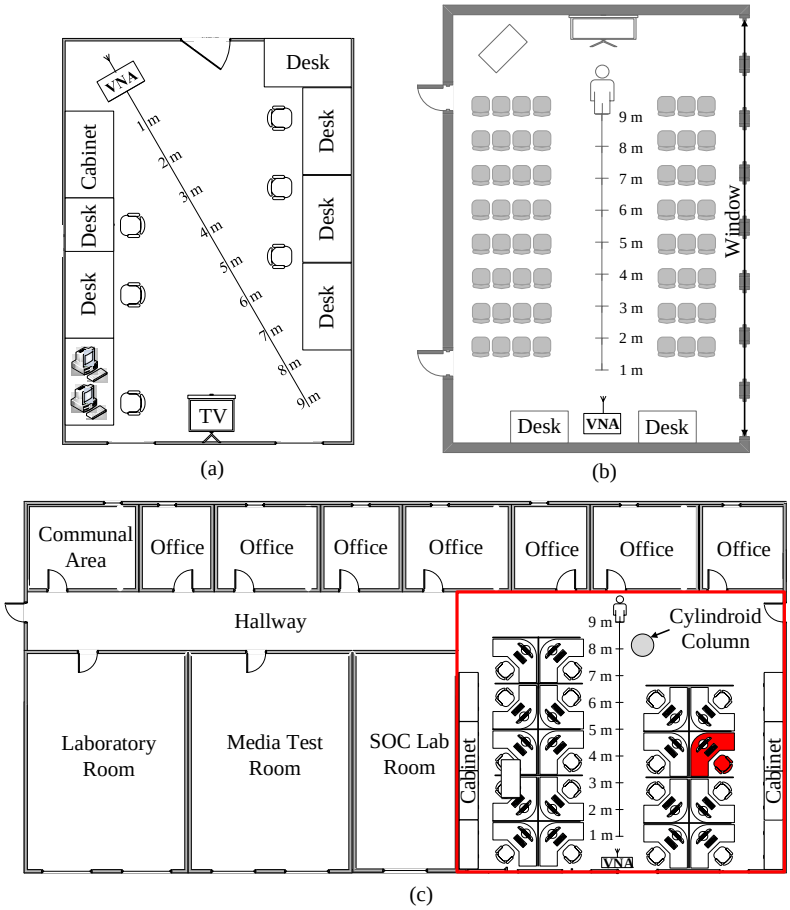

Figure 3.3: Three indoor measurement environments: (a) laboratory (43.42 m^2), (b) seminar room (99.63 m^2) and (c) open office (red rectangle: 129.88 m^2).

To improve the generality of the field validations conducted here, another wearable channel measurement was performed in a more sparse environment, namely an outdoor car park area adjacent to the ECIT building as shown in Figure 3.4. For the LOS wearable channel conditions, as shown in Figures 3.3 and 3.4, the test subject walked towards the RX in a straight line in each environment (i.e. from 9 m point to 1 m point). It is worth remarking that the LOS wearable channel measurement was conducted once for each environment.

3.5 Results

To abstract the composite fading signal for the wearable measurements, the estimated path loss was removed from the raw measurement data using the log-distance path loss given in (2.1). To this end, the elapsed time was first converted

Figure 3.4: Outdoor car park area environment used for the wearable channel measurements.

into a distance based upon an estimate of the test subject's velocity. The corresponding parameter estimates for the κ-μ / inverse gamma composite fading model were obtained using a non-linear least squares routine programmed in MATLAB to fit (3.6) to the wearable measurement data. As an example of the model fitting, Figures 3.5 and 3.6 show that the PDFs of the κ-μ / inverse gamma composite fading model fitted to the measurement data for the chest (Figure 3.5) and waist (Figure 3.6) positioned antenna within each environment. It is obvious that the κ-μ / inverse gamma composite fading model provided an excellent fit to the measurement data for all of the considered cases.

Table 3.1 provides the parameter estimates for the κ-μ / inverse gamma model for all of the considered wearable channels. As shown in Table 3.1, the κ parameter[1] obtained for the indoor hallway, seminar and open office environments were much lower than that for the outdoor car park environment. This is most likely due to the fact that the outdoor environment exhibits the relatively anechoic conditions (i.e. less multipath) compared to the indoor environments. This observation can be supported by the μ parameters for the indoor environments, which were greater than those obtained for the outdoor environment. Consequently, the total power of the scattered signal components in the outdoor car park environment was lower than those for the indoor environments.

[1]The κ parameter, which defines the ratio of the total power of the dominant signal components (δ^2) to the total power of the scattered signal components ($2\mu\sigma^2$), is equivalent to the K factor of the Rice distribution when $\mu = 1$.

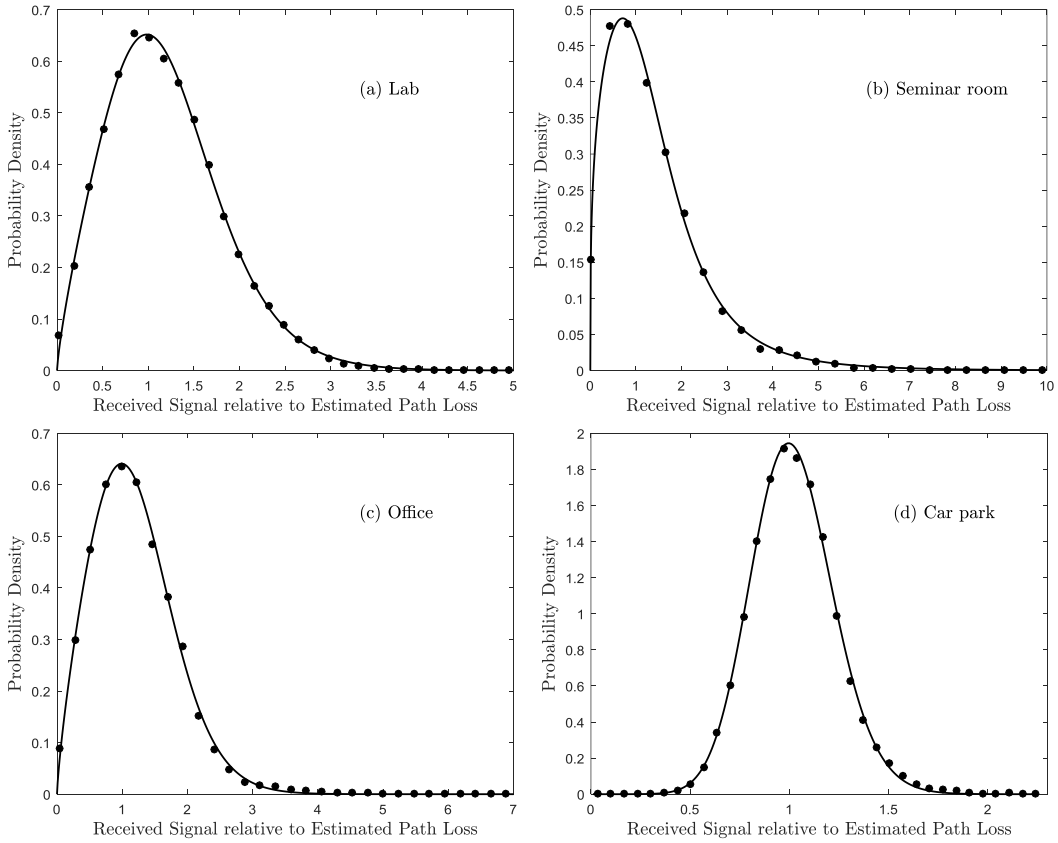

Figure 3.5: Empirical PDFs (circles) of the composite fading signal observed in the LOS wearable links for the chest positioned antenna in the (a) laboratory, (b) seminar room, (c) open office and (d) car park environments compared to the theoretical probability of the κ-μ / inverse gamma composite fading model (continuous lines).

Also, the m_s parameters obtained for the indoor hallway, seminar and open office environments were found to be lower than that for the outdoor car park environment. This suggests that the indoor LOS radio link still experienced some shadowing even if a direct signal path existed. This observation was most likely caused by the fact that contributing signal components other than those arriving via LOS propagation, i.e. multipath components including both the dominant and scattered signal contributions, were shadowed by the human body and the surrounding obstacles in the indoor environments. On the other hand, the outdoor LOS link suffered less from a fluctuation of the mean signal power due to the relatively anechoic conditions which offered less opportunity for the generation of shadowed multipath components.

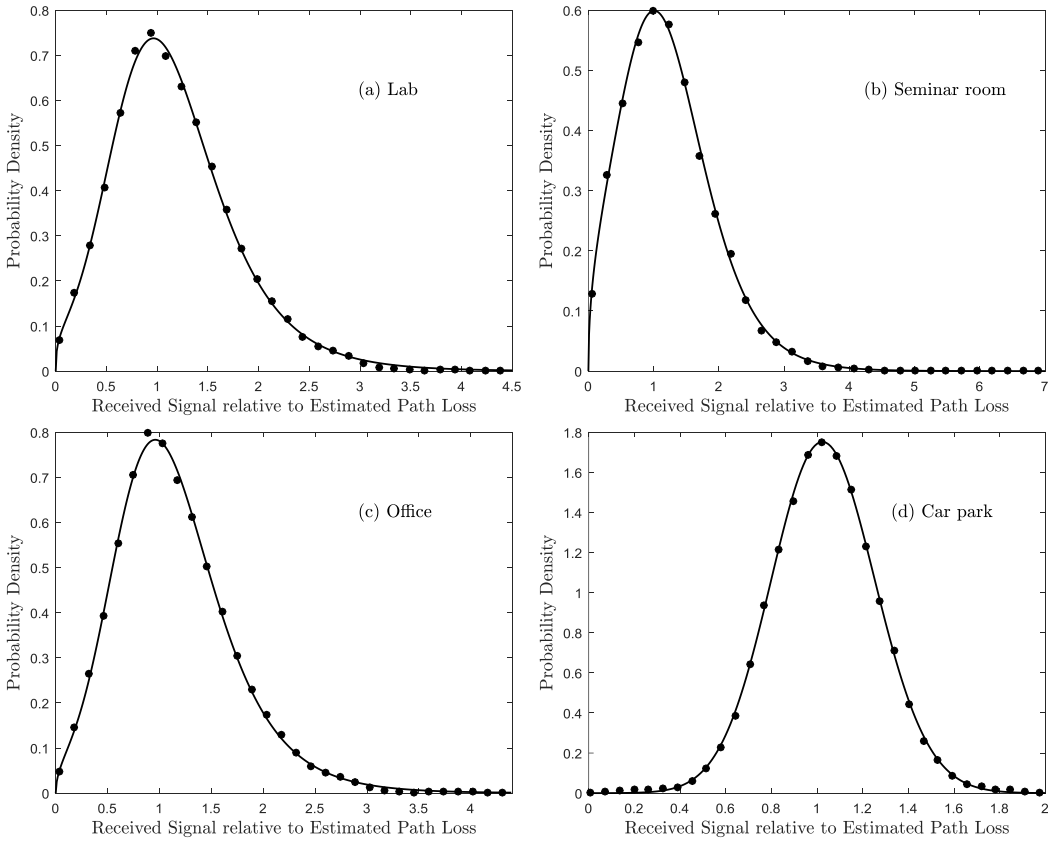

Figure 3.6: Empirical PDFs (circles) of the composite fading signal observed in the LOS wearable links for the waist positioned antenna in the (a) laboratory, (b) seminar room, (c) open office and (d) car park environments compared to the theoretical probability of the κ-μ / inverse gamma composite fading model (continuous lines).

3.6 A Comparison with other Composite Fading Models

To further demonstrate the versatility of the proposed composite fading model, the κ-μ / inverse gamma composite fading model was compared with other composite fading models based on the κ-μ distribution, namely κ-μ / lognormal [24], κ-μ / gamma [75] and shadowed κ-μ [73] models. To this end, the AICc was utilised to ascertain the most probable model among these composite fading distributions for characterizing LOS wearable channels. Similarly, the respective parameters for other composite fading models were firstly estimated using a non-linear least squares routine programmed in MATLAB.

According to the calculated AICc values, the four candidate models were

Table 3.1: Parameter estimates of the κ-μ / inverse gamma composite fading model for all of the considered LOS wearable channel measurement data.

Environments	Positions	κ	μ	Ω	m_s
Laboratory	Chest	1.16	0.89	1.57	6.93
	Waist	3.36	0.69	1.33	3.78
Seminar	Chest	0.78	0.65	1.80	1.87
	Waist	1.62	0.74	1.67	5.51
Open Office	Chest	0.97	0.89	1.64	11.79
	Waist	3.20	0.76	1.28	4.24
Car park	Chest	50.00	0.30	1.05	32.53
	Waist	50.00	0.22	1.10	100.00

Table 3.2: AICc rank for all of the considered LOS wearable channel measurement data.

Environments	Positions	κ-μ / lognormal	κ-μ / inverse gamma	κ-μ / gamma	shadowed κ-μ
Laboratory	Chest	4	**1**	2	3
	Waist	4	2	**1**	3
Seminar	Chest	2	**1**	4	3
	Waist	4	**1**	2	3
Open Office	Chest	4	**1**	2	3
	Waist	4	**1**	2	3
Car park	Chest	3	**1**	2	4
	Waist	3	**1**	4	2

ranked as shown in Table 3.2. It was found that the κ-μ / inverse gamma composite fading model was selected as the best model for all of the cases considered in this Chapter with the exception of the waist position in the laboratory environment (i.e. 87.5% of the considered cases). In this case, the κ-μ / gamma composite fading model provided the best representation of the measurement data while the κ-μ / inverse gamma composite fading model was chosen as the second best model. Nevertheless, as shown in Figure 3.7, the κ-μ / inverse gamma composite fading model also provides an excellent fit to measurement data.

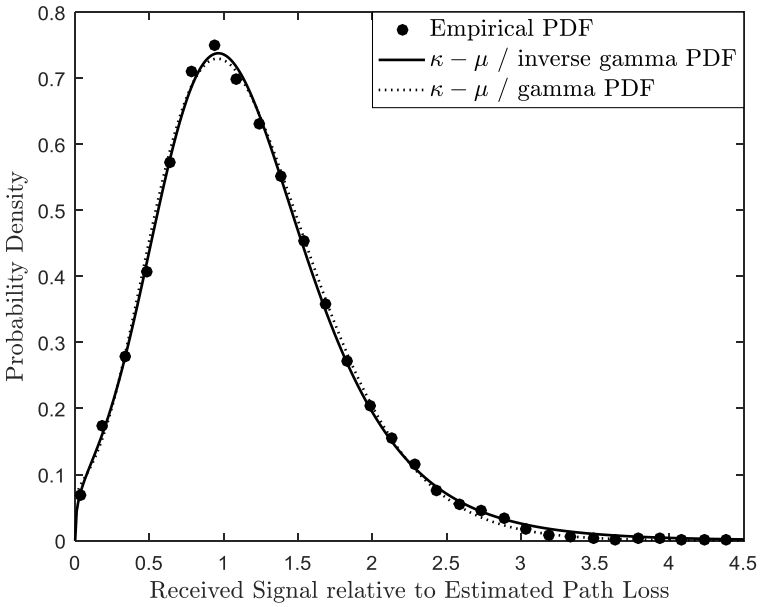

Figure 3.7: Empirical PDF (circles), the κ-μ / inverse gamma PDF (continuous lines) and the κ-μ / gamma PDF (dotted lines) for the waist positioned antenna in the laboratory environment.

3.7 Conclusion

In this Chapter, a new composite fading model, namely κ-μ / inverse gamma composite fading model, has been proposed to characterize the composite fading signal observed in LOS wearable communications channels. This model assumes that the mean power of the both dominant and scattered signal components is subject to shadowing and weighted by an inverse gamma random variable. The fundamental statistics of the κ-μ / inverse gamma composite fading model, such as the PDF, CDF, MGF, higher order moments and AF, have been obtained in convenient closed-form expressions.

The versatility of the proposed κ-μ / inverse gamma composite fading model has been validated using a diverse range of LOS wearable channel measurements. By considering the composite fading signal, it was able to take into account the simultaneous impact of multipath and shadowing. Over all of the LOS wearable channel measurements undertaken, the observed composite fading was well described using the newly proposed model, i.e. κ-μ / inverse gamma composite fading model. Most importantly though, using the AICc, it has been shown that

the κ-μ / inverse gamma composite fading model was chosen as the most likely candidate model for the majority of cases.

The κ-μ fading model has been proven to model multipath for both conventional and emerging wireless communications channels. Additionally, the κ-μ / inverse gamma composite fading model includes other well-known distributions as special cases (e.g. κ-μ, Rice, Rayleigh, Nakagami-m, etc.) and is also able to approximate other composite fading models, which have been used in the general area of wireless communications. Consequently, the κ-μ / inverse gamma model will also find application in the general area of wireless communications and beyond although its applicability is restricted to wearable applications in this thesis.

Chapter 4

New Composite Fading Models for NLOS Wearable Channels

Quite often in wearable communications channels, there may exist no direct signal path between the TX and RX. This may happen for example when the user's body or building structures obstruct the optical LOS path between the TX and RX. In this instance, it is more reasonable to assume that scattered multipath components exist only, i.e. the wearable link is maintained by NLOS channel conditions. Here, the mean power will be subject to shadowing which can be induced by the user's body or the local surroundings (or a combination of both). In order to investigate the characteristics of the composite fading signal experienced in NLOS wearable channels, this Chapter proposes two different composite fading models, namely $\mathcal{F}$ and η-μ/ inverse gamma composite fading models. Subsequently their fundamental statistics such as the PDF, CDF, MGF, higher order moments and AF are derived. Additionally, this Chapter also demonstrates the applicability of the new NLOS models using an extensive set of field measurements. In particular, it compares the proposed composite fading models with other composite fading models which are traditionally associated with NLOS channel conditions using the AICc.

4.1 Introduction

The Nakagami-m distribution has gained widespread use to characterize multipath fading in NLOS channel conditions. Accordingly, there exist a number of composite fading models associated with the Nakagami-m distribution, namely Nakagami-m / lognormal model [67], Nakagami-m / gamma model [68] known as the generalized K distribution (K_G) and Nakagami-m / inverse Gaussian model [72] known as the G distribution. Notably, their PDFs have been obtained in closed-form with the exception of the Nakagami-m / lognormal model.

Recently, the η-μ distribution was proposed to represent the random variation of the multipath fading signal under NLOS channel conditions. It is a generalized fading distribution which includes as special cases other important distributions, such as Rayleigh, Hoyt (Nakagami-q) and Nakagami-m distributions. Due to its generality, new composite fading models based on the η-μ distribution have been subsequently proposed. For example, the η-μ / gamma [76, 77] and η-μ / inverse Gaussian [79] composite fading models were derived under the assumption that the scattered signal components are subject to η-μ fading and its mean power is shadowed. The derived PDFs in [76, 79] are expressed using infinite series expansions (i.e. not in closed-form) and thus their PDFs must be computed numerically, rendering them intractable for use in the analytical calculations associated with the performance evaluation of wireless systems. It is worth remarking that closed-form for the PDF of the η-μ / gamma composite fading model was presented in [77], but the resulting formulation is only valid for integer values of the μ parameter.

Therefore, in this Chapter, new composite fading models, namely $\mathcal{F}$ and η-μ / inverse gamma composite fading models, have been proposed to characterize the composite fading signal observed in NLOS wearable channels. The main contributions of this Chapter can be summarized as follows

- The PDF, CDF, MGF, higher order moments and AF of the $\mathcal{F}$ composite fading model have been obtained in simple and convenient closed-form

expressions.

- Closed-form expressions for the PDF, higher order moments and AF of the η-μ / inverse gamma composite fading model have been obtained along with exact analytic expressions for the corresponding CDF and MGF.

- The generality of the $\mathcal{F}$ and η-μ / inverse gamma composite fading models has been demonstrated through reduction to some special cases with a number of distributions as well as its ability to approximate other composite fading models.

- An important empirical validation of the $\mathcal{F}$ and η-μ / inverse gamma composite fading models for use in wearable communications channels is performed.

- Using the AICc, it is also shown that these new models are regularly selected as the most likely candidate model compared to other composite fading distributions which are associated with the NLOS channel conditions, e.g. K_G, η-μ / gamma and η-μ / inverse Gaussian models.

4.2 Fundamental Statistics of the $\mathcal{F}$ Composite Fading Model

4.2.1 Signal Model

In an $\mathcal{F}$ composite fading channel, the multipath fading is manifested by the same propagation mechanisms responsible for Nakagami-m fading whereas the root-mean-square (rms) power of the received signal is subject to random variation induced by shadowing. Based on this, the composite signal envelope, R, can be defined as

$$R = \sqrt{\sum_{i=1}^{n_s} A_m^2 I_i^2 + A_m^2 Q_i^2} \tag{4.1}$$

where n_s represents the number of multipath clusters, I_i and Q_i are independent Gaussian random variables which denote the in-phase and quadrature phase components of the cluster i, with $\mathbb{E}[I_i] = \mathbb{E}[Q_i] = 0$, $\mathbb{E}[I_i^2] = \mathbb{E}[Q_i^2] = \sigma^2$. Moreover, A_m is an inverse Nakagami-m random variable[1] with the shape parameter m_s and spread parameter $1/\Omega_s$ where Ω_s is set equal to unity (i.e. $\Omega_s = 1$) and therefore the PDF of A_m is given as follows

$$f_{A_m}(\alpha_m) = \frac{2{m_s}^{m_s}}{\Gamma(m_s)\,{\alpha_m}^{2m_s+1}} \exp\left(-\frac{m_s}{{\alpha_m}^2}\right). \tag{4.2}$$

4.2.2 PDF and CDF

Using the aforementioned signal model in (4.1), this insinuates that

$$f_{R|A_m}(r|\alpha_m) = \frac{2m^m r^{2m-1}}{\Gamma(m)\;{\alpha_m}^{2m}\,\Omega^m} \exp\left(-\frac{m\,r^2}{{\alpha_m}^2\,\Omega}\right). \tag{4.3}$$

Now, substituting (4.3) and (4.2) into (3.3), performing a simple transformation of variables and using [53, Eq. (3.326.2)] along with some algebraic manipulation, closed-form for the PDF of the $\mathcal{F}$ composite fading model can be obtained as

$$f_R(r) = \frac{2m^m (m_s\Omega)^{m_s} r^{2m-1}}{B(m,m_s)(mr^2 + m_s\Omega)^{m+m_s}}. \tag{4.4}$$

The form of the PDF in (4.4) is functionally equivalent to the Fisher-Snedecor $\mathcal{F}$ distribution[2]. The corresponding PDF of the instantaneous SNR of the $\mathcal{F}$ composite fading model can be readily obtained by letting $\gamma = \bar{\gamma} r^2/\Omega$, yielding

$$f_\gamma(\gamma) = \frac{m^m (m_s\,\bar{\gamma})^{m_s} \gamma^{m-1}}{B(m,m_s)\,(m\gamma + m_s\,\bar{\gamma})^{m+m_s}}. \tag{4.5}$$

[1] As mentioned in Chapter 3, the inverse gamma distribution can be efficiently used to model shadowing of the signal power. The inverse gamma and inverse Nakagami-m random variables are related by a simple quadratic transformation. Accordingly, the inverse Nakagami-m distribution can be used to model shadowing of the rms signal power.

[2] Letting $r^2 = \Omega x$, $m = d_1/2$, $m_s = d_2/2$ and performing the required transformation yields the Fisher-Snedecor PDF, $f_x(x)$, with parameters d_1 and d_2.

It is worth highlighting that the area under the resultant PDF has been analytically confirmed such that $\int_0^\infty f_\gamma(\gamma)\,\mathrm{d}\gamma = 1$. Based on (4.5), the CDF of the instantaneous SNR of the $\mathcal{F}$ composite fading model can be obtained with the aid of [53, Eq. (3.194.1)], such that

$$F_\gamma(\gamma) = \frac{m^{m-1}\gamma^m}{B\left(m, m_s\right)\left(m_s\,\bar{\gamma}\right)^m}{}_2F_1\left(m + m_s, m; m+1; -\frac{m\gamma}{m_s\,\bar{\gamma}}\right). \tag{4.6}$$

4.2.3 Higher Order Moments and AF

The higher order moments and AF of the instantaneous SNR of the $\mathcal{F}$ composite fading model can be derived using [53, Eq. (3.194.3)] and [16, Eq. (1.27)] respectively,

$$\mathbb{E}\left[\gamma^n\right] = \left(\frac{m_s\,\bar{\gamma}}{m}\right)^n \frac{B\left(m+n, m_s-n\right)}{B\left(m, m_s\right)} \tag{4.7}$$

$$AF = \frac{\mathbb{E}\left[\gamma^2\right]}{\mathbb{E}[\gamma]^2} - 1 = \frac{m + m_s - 1}{m\left(m_s - 2\right)}. \tag{4.8}$$

4.2.4 MGF

With the aid of [53, Eq. (3.383.5)], making use of the generalized Laguerre polynomials [94, Eq. (07.03.02.0001.01)] and carrying out some algebraic manipulation, the MGF of the $\mathcal{F}$ composite fading model can be obtained in closed-form as

$$\begin{aligned} M_\gamma(-s) = {}&{}_1F_1\left(m; 1-m_s; \frac{s\bar{\gamma}m_s}{m}\right) \\ &+ \frac{\Gamma\left(-m_s\right)}{B\left(m, m_s\right)}\left(\frac{s\bar{\gamma}m_s}{m}\right)^{m_s}{}_1F_1\left(m+m_s; 1+m_s; \frac{s\bar{\gamma}m_s}{m}\right) \end{aligned} \tag{4.9}$$

which is valid for $m + m_s \neq \mathbb{N}$ and $m_s \neq \mathbb{N}$. Nonetheless, these potential singularities can be straightforwardly circumvented by introducing infinitely small perturbation terms which can be added to $m + m_s$ and m_s respectively.

4.3 Fundamental Statistics of the η-μ / Inverse Gamma Composite Fading Model

4.3.1 Signal Model

Similar to the physical signal model proposed for the η-μ fading channel [48], the received signal in an η-μ / inverse gamma composite fading channel is composed of separable clusters of multipath waves propagating in a non-homogeneous environment. As discussed in Chapter 2.2.5, there exist two different formats according to two corresponding physical models. It is worth highlighting that the *Format* 1 is only considered in this Chapter. Therefore, the in-phase and quadrature components of the fading signal within each cluster are assumed to be independent from each other and to have different power. Unlike the η-μ fading model, in the η-μ / inverse gamma composite fading model, the mean power of the scattered waves is randomly fluctuated by shadowing. Following this definition, the composite signal envelope, R, in an η-μ / inverse gamma fading channel can be expressed as

$$R = \sqrt{\sum_{i=1}^{n_s} AI_i^2 + AQ_i^2} \tag{4.10}$$

where n_s represents the number of clusters of multipath, I_i and Q_i are mutually independent Gaussian random variables which denote the in-phase and quadrature components of the cluster i, with $E[I_i] = E[Q_i] = 0$, $E[I_i^2] = \sigma_I^2$ and $E[Q_i^2] = \sigma_Q^2$ while A denotes an inverse gamma random variable with the shape parameter m_s and scale parameter m_s/Ω_s where Ω_s is set equal to unity (i.e. $\Omega_s = 1$) which is given in (3.2).

4.3.2 PDF and CDF

Using the signal model given in (4.10), for the η-μ / inverse gamma composite fading model, this insinuates that

$$f_{R|\Omega}(r|\omega) = \frac{4\sqrt{\pi}\,\mu^{\mu+\frac{1}{2}}\,h^{\mu}r^{2\mu}}{\Gamma(\mu)\,H^{\mu-\frac{1}{2}}(\alpha\,\Omega)^{\mu+\frac{1}{2}}}\,\exp\left(-\frac{2\mu h r^2}{\alpha\,\Omega}\right) I_{\mu-\frac{1}{2}}\left(\frac{2\mu H r^2}{\alpha\,\Omega}\right). \tag{4.11}$$

By substituting (4.11) and (3.2) into (3.3), the PDF of the composite signal envelope in an η-μ / inverse gamma composite fading channel, R, can be obtained as follows

$$\begin{aligned} f_R(r) = \frac{4\sqrt{\pi}\,\mu^{\mu+\frac{1}{2}}\,h^{\mu}{m_s}^{m_s}r^{2\mu}}{\Gamma(\mu)\,\Gamma(m_s)\,H^{\mu-\frac{1}{2}}\,\Omega^{\mu+\frac{1}{2}}} \int_0^{\infty}\left(\frac{1}{\alpha}\right)^{m_s+\mu+\frac{3}{2}}\exp\left(-\frac{m_s}{\alpha}\right) \\ \times\exp\left(-\frac{2\mu h r^2}{\alpha\,\Omega}\right) I_{\mu-\frac{1}{2}}\left(\frac{2\mu H r^2}{\alpha\,\Omega}\right)\mathrm{d}\alpha. \end{aligned} \tag{4.12}$$

Now, performing a simple transformation of variables and applying equation [92, Eq. (2.15.3.2)] along with some algebraic manipulation, (4.12) can be expressed in closed-form as

$$\begin{aligned} f_R(r) = \frac{2^{2\mu+1}\mu^{2\mu}\,h^{\mu}(m_s\Omega)^{m_s}r^{4\mu-1}}{B(m_s,2\mu)\,(2\mu h r^2+m_s\Omega)^{m_s+2\mu}} \\ \times\,{}_2F_1\left(\frac{m_s+2\mu}{2},\frac{m_s+2\mu+1}{2};\frac{2\mu+1}{2};\frac{(2\mu H r^2)^2}{(2\mu h r^2+m_s\Omega)^2}\right). \end{aligned} \tag{4.13}$$

By letting $\gamma = \bar{\gamma}r^2/\Omega$, the corresponding PDF of the instantaneous SNR of the η-μ / inverse gamma composite fading channel can be expressed as follows

$$\begin{aligned} f_{\gamma}(\gamma) = \frac{2^{2\mu}\mu^{2\mu}\,h^{\mu}(m_s\bar{\gamma})^{m_s}\gamma^{2\mu-1}}{B(m_s,2\mu)\,(2\mu h\gamma+m_s\bar{\gamma})^{m_s+2\mu}} \\ \times\,{}_2F_1\left(\frac{m_s+2\mu}{2},\frac{m_s+2\mu+1}{2};\frac{2\mu+1}{2};\frac{(2\mu H\gamma)^2}{(2\mu h\gamma+m_s\bar{\gamma})^2}\right). \end{aligned} \tag{4.14}$$

Again, it is worth remarking that the resultant PDF has been analytically confirmed that $\int_0^{\infty} f_{\gamma}(\gamma)\,\mathrm{d}\gamma = 1$. The CDF of the instantaneous SNR of the η-μ /

inverse gamma composite model can be obtained such that

$$F_{\gamma}(\gamma) = \int_0^{\gamma} \frac{2^{2\mu}\,\mu^{2\mu}\,h^{\mu}(m_s\bar{\gamma})^{m_s}\gamma^{2\mu-1}}{B\left(m_s,2\mu\right)\left(2\mu h\gamma + m_s\bar{\gamma}\right)^{m_s+2\mu}} \times {}_2F_1\left(\frac{m_s+2\mu}{2}, \frac{m_s+2\mu+1}{2}; \frac{2\mu+1}{2}; \left(\frac{2\mu H\gamma}{2\mu h r^2 + m_s\bar{\gamma}}\right)^2\right) \mathrm{d}\gamma. \tag{4.15}$$

By expanding the Gauss hypergeometric function in (4.15) in terms of the series representation[1] given in (3.12), (4.15) can be rewritten as follows

$$F_{\gamma}(\gamma) = \sum_{i=0}^{\infty} \frac{\left(\frac{m_s+2\mu}{2}\right)_i \left(\frac{m_s+2\mu+1}{2}\right)_i (2\mu)^{2\mu+2i}\,h^{\mu}H^{2i}\,(m_s\bar{\gamma})^{m_s}}{i!\left(\frac{2\mu+1}{2}\right)_i B\left(m_s,2\mu\right)} \times \int_0^{\gamma} \frac{\gamma^{2\mu+2i-1}}{\left(2\mu h\gamma + m_s\bar{\gamma}\right)^{m_s+2\mu+2i}}\,\mathrm{d}\gamma. \tag{4.16}$$

With the aid of [53, Eq. (3.194.1)], the CDF of the η-μ / inverse gamma composite fading model can be obtained as

$$F_{\gamma}(\gamma) = \frac{2^{2\mu-1}\,h^{\mu}}{\Gamma\left(m_s\right)\Gamma\left(2\mu\right)} \sum_{i=0}^{\infty} \frac{\Gamma\left(m_s+2\mu+2i\right)H^{2i}}{i!\left(\frac{2\mu+1}{2}\right)_i\left(\mu+i\right)} \left(\frac{\mu\gamma}{m_s\bar{\gamma}}\right)^{2\mu+2i} \times {}_2F_1\left(m_s+2\mu+2i, 2\mu+2i; 2\mu+2i+1; -\frac{2\mu h\gamma}{m_s\bar{\gamma}}\right). \tag{4.17}$$

4.3.3 Higher Order Moments and AF

Similarly, the higher order moments of the instantaneous SNR of the proposed η-μ / inverse gamma composite fading model can be expressed using an infinite series expansion of the Gauss hypergeometric function given in (3.12) such that

$$\mathbb{E}\left[\gamma^n\right] = \sum_{i=0}^{\infty} \frac{\left(\frac{m_s+2\mu}{2}\right)_i \left(\frac{m_s+2\mu+1}{2}\right)_i (2\mu)^{2\mu+2i}\,h^{\mu}H^{2i}\,(m_s\bar{\gamma})^{m_s}}{i!\left(\frac{2\mu+1}{2}\right)_i B\left(m_s,2\mu\right)} \times \int_0^{\infty} \frac{\gamma^{2\mu+n+2i-1}}{\left(2\mu h\gamma + m_s\bar{\gamma}\right)^{m_s+2\mu+2i}}\,\mathrm{d}\gamma. \tag{4.18}$$

[1] For $|z| < 1$, the Gauss hypergeometric function ${}_2F_1\left(\cdot,\cdot;\cdot;z\right)$ is defined as an infinite sum (that is convergent). In this case, as shown in (4.15), $z = \left(\frac{2\mu H\gamma}{2\mu h\gamma + m_s\bar{\gamma}}\right)^2$. Since $h = \frac{2+\eta^{-1}+\eta}{4}$, $H = \frac{\eta^{-1}-\eta}{4}$ and $\mu, \gamma, m_s, \bar{\gamma} > 0$, the denominator $(2\mu h\gamma + m_s\bar{\gamma})$ is always greater than the numerator $(2\mu H\gamma)$ and thus z is always smaller than 1.

With the aid of [53, Eq. (3.194.3)] and using the series representation of the Gauss hypergeometric function given in (3.12), (4.18) can be reduced to

$$\mathbb{E}\left[\gamma^n\right] = \frac{B\left(m_s - n, 2\mu + n\right)}{B\left(m_s, 2\mu\right) h^{\mu}} \left(\frac{m_s \bar{\gamma}}{2\mu h}\right)^n {}_2F_1\left(\mu + \frac{n}{2}, \mu + \frac{n}{2} + \frac{1}{2}; \mu + \frac{1}{2}; \frac{H^2}{h^2}\right). \tag{4.19}$$

By substituting $n = 1$ and $n = 2$ in (4.19) respectively, $\mathbb{E}\left[\gamma\right]$ and $\mathbb{E}\left[\gamma^2\right]$ are simply given as

$$\mathbb{E}\left[\gamma\right] = \frac{B\left(m_s - 1, 2\mu + 1\right)}{h^{\mu} B\left(m_s, 2\mu\right)} \left(\frac{m_s \bar{\gamma}}{2\mu h}\right) {}_2F_1\left(\mu + \frac{1}{2}, \mu + 1; \mu + \frac{1}{2}; \frac{H^2}{h^2}\right) \tag{4.20}$$

$$\mathbb{E}\left[\gamma^2\right] = \frac{B\left(m_s - 2, 2\mu + 2\right)}{h^{\mu} B\left(m_s, 2\mu\right)} \left(\frac{m_s \bar{\gamma}}{2\mu h}\right)^2 {}_2F_1\left(\mu + 1, \mu + \frac{3}{2}; \mu + \frac{1}{2}; \frac{H^2}{h^2}\right). \tag{4.21}$$

Using the following representation of the Gauss hypergeometric function [94, Eq. (07.23.17.0054.01)],

$${}_2F_1\left(c - a\,, c - b\,;\, c\,;\, z\right) = (1 - z)^{a+b-c}\, {}_2F_1\left(a\,, b\,;\, c\,;\, z\right) \tag{4.22}$$

the Gauss hypergeometric functions in (4.20) and (4.21) can be rewritten as

$${}_2F_1\left(\mu + \frac{1}{2}, \mu + 1\ \mu + \frac{1}{2}; \frac{H^2}{h^2}\right) = \left(1 - \frac{H^2}{h^2}\right)^{-(\mu+1)} {}_2F_1\left(0, -\frac{1}{2}; \mu + \frac{1}{2}; \frac{H^2}{h^2}\right) \tag{4.23}$$

$${}_2F_1\left(\mu + 1, \mu + \frac{3}{2}; \mu + \frac{1}{2}; \frac{H^2}{h^2}\right) = \left(1 - \frac{H^2}{h^2}\right)^{-(\mu+2)} {}_2F_1\left(-\frac{1}{2}, -1; \mu + \frac{1}{2}; \frac{H^2}{h^2}\right). \tag{4.24}$$

By substituting the series expansion of the Gauss hypergeometric function [94, Eq. (07.23.02.0001.01)] and then simplifying the Pochhammer terms, the following representations of the Gauss hypergeometric function in (4.23) and (4.24) can be obtained as

$${}_2F_1\left(0, -\frac{1}{2}; \mu + \frac{1}{2}; \frac{H^2}{h^2}\right) = 1 \tag{4.25}$$

$${}_2F_1\left(-\frac{1}{2}, -1; \mu + \frac{1}{2}; \frac{H^2}{h^2}\right) = \frac{h^2 + H^2 + 2\mu h^2}{h^2\left(1 + 2\mu\right)}. \tag{4.26}$$

The corresponding AF of the η-μ / inverse gamma composite fading model can eventually be obtained in closed-form as follows

$$AF = \frac{h^{-(\mu+2)}\left(h^2 - H^2\right)^{\mu}\left(H^2 + 2\mu h^2 + h^2\right)(m_s - 1)}{2\mu\,(m_s - 2)} - 1. \tag{4.27}$$

4.3.4 MGF

The MFG of the proposed η-μ / inverse gamma composite fading model can be derived from (4.14) using the exact infinite series expansion of the Gauss hypergeometric function given in (3.12) as follows

$$\begin{aligned} M_s(-s) = \sum_{i=0}^{\infty} \frac{\left(\frac{m_s+2\mu}{2}\right)_i \left(\frac{m_s+2\mu+1}{2}\right)_i (2\mu)^{2\mu+2i}\, h^{\mu} H^{2i} \left(m_s\bar{\gamma}\right)^{m_s}}{i!\left(\frac{2\mu+1}{2}\right)_i B\left(m_s, 2\mu\right)} \\ \times \int_0^{\infty} \frac{\gamma^{2\mu+2i-1}\exp\left(-s\gamma\right)}{\left(2\mu h\gamma + m_s\bar{\gamma}\right)^{m_s+2\mu+2i}}\,\mathrm{d}\gamma. \end{aligned} \tag{4.28}$$

With the aid of [53, Eq. (3.383.5)], making use of the generalized Laguerre polynomials [94, Eq. (07.03.02.0001.01)], performing the necessary change of variables and carrying out some algebraic manipulation, the corresponding MGF can be obtained as

$$\begin{aligned} M_{\gamma}(-s) = \sum_{i=0}^{\infty} \frac{\Gamma\left(\mu + i\right) H^{2i}}{i!\,\Gamma\left(\mu\right) h^{\mu+2i}} \Bigg[{}_1F_1\left(2\mu + 2i;\, 1 - m_s;\, \frac{s m_s \bar{\gamma}}{2\mu h}\right) \\ + \left(\frac{s m_s \bar{\gamma}}{2\mu h}\right)^{m_s} \frac{\Gamma\left(-m_s\right)}{B\left(m_s, 2\mu + 2i\right)} {}_1F_1\left(m_s + 2\mu + 2i;\, 1 + m_s;\, \frac{s m_s \bar{\gamma}}{2\mu h}\right)\Bigg]. \end{aligned} \tag{4.29}$$

Similar to (3.27) and (4.9), the terms of $m_s + 2\mu + 2i$ and m_s in (4.29) must not equate to a positive integer. Again, these potential singularities can be straightforwardly circumvented by introducing infinitely small perturbation terms which can be added to $m_s + 2\mu + 2i$ and m_s respectively if required.

4.4 Special Cases and Approximations

4.4.1 $\mathcal{F}$ Composite Fading Model

In (4.4), the m_s parameter controls the amount of shadowing of the rms signal power. As m_s tends towards zero (i.e. $m_s \to 0$), the rms signal power in an $\mathcal{F}$ composite fading channel is observed to undergo very heavy shadowing. Conversely, as m_s approaches infinity (i.e. $m_s \to \infty$) there is no shadowing of the rms signal power and thus the PDF given in (4.4) becomes equivalent to the Nakagami-m PDF given in (2.4). Consequently, the $\mathcal{F}$ composite fading model inherits all of the characteristics of the Nakagami-m fading model. Figure 4.1(a) shows some examples for the special cases of the $\mathcal{F}$ composite fading model. It is also worth highlighting the ability of the $\mathcal{F}$ composite fading model to approximate other more complicated composite fading models found in the literature. As an example, Figure 4.1(b) shows that the $\mathcal{F}$ composite fading model (m, Ω, m_s) provides a good approximation to the Rayleigh / gamma (k, θ) [69], Nakagami-m / lognormal (m, a_l, s_l) [67] and Nakagami-m / gamma (m, k, θ) [68] composite fading models. It should be noted that the m_s and Ω parameters of the $\mathcal{F}$ composite fading model were estimated using (3.29), (3.30), (3.31) and (3.32).

4.4.2 η-μ / Inverse Gamma Composite Fading Model

The PDF given in (4.13) represents an extremely versatile model as it inherits all of the generality of the η-μ model. In (4.13), the m_s parameter controls the amount of the shadowing of the mean signal power. As $m_s \to 0$, the scattered signal components are completely shadowed while as $m_s \to \infty$, there is no shadowing present in the channel. Some special cases of the η-μ / inverse gamma composite model are illustrated in Figure 4.2(a). When there is no shadowing of the mean signal power, i.e. $m_s \to \infty$ (in reality, m_s becomes large), the mean signal power becomes deterministic and thus the η-μ / inverse gamma PDF given in (4.13) coincides with the η-μ fading PDF in (2.8). It is worth highlighting that

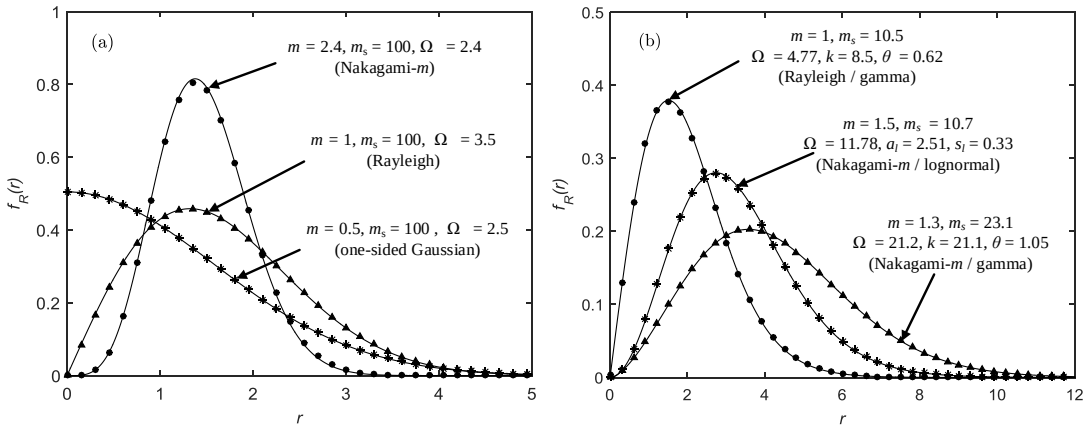

Figure 4.1: PDFs of the $\mathcal{F}$ composite fading model for the (a) special cases with well-known distributions and (b) approximation of other composite fading models.

it can be also used to provide an accurate approximation of other lognormal- and gamma-based composite fading models. For example, Figure 4.2(b) shows that the η-μ / inverse gamma (η, μ, Ω, m_s) composite fading model is in good agreement with the Rayleigh / lognormal (a_l, s_l) [65], Rayleigh / gamma (k, θ) [69] and Nakagami-m / gamma (m, k, θ) [68] composite fading models. Again, the m_s and Ω parameters of the η-μ / inverse gamma composite fading model were estimated by matching their first and second moments and the corresponding formulations are given in (3.29), (3.30), (3.31) and (3.32).

4.5 NLOS Wearable Channel Measurements

The same measurement setup and environments described in Chapter 3.4 was again utilised for the NLOS wearable channel measurements presented here. The same two wearable node positions were considered, namely the central-chest and central-waist regions. To create the NLOS wearable channel conditions, the test subject walked away from the RX in a straight line in each environment, i.e. from 1 m point to 9 m point. It is worth remarking that NLOS channel conditions only occured when the direct optical path between the wearable node and RX was obstructed by the test subject's body.

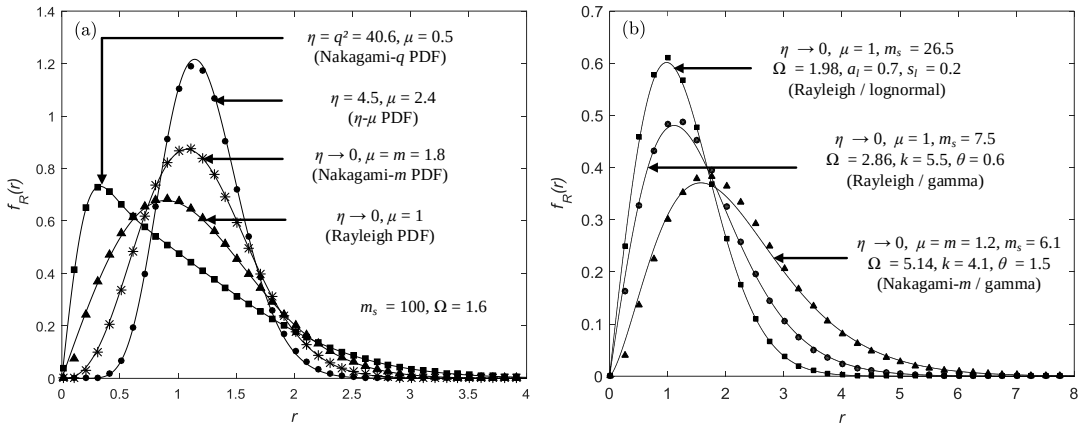

Figure 4.2: PDFs of the η-μ / inverse gamma composite fading model for the (a) special cases with well-known distributions and (b) approximation of other composite fading models.

4.6 Results

Similar to the data analysis performed for the LOS wearable channel measurements in Chapter 3.5, the composite fading signal was extracted by removing the estimated path loss from the raw measurement data using the log-distance path loss. Following this, the corresponding parameter estimates for the $\mathcal{F}$ and η-μ / inverse gamma composite fading models were obtained using a non-linear least squares routine programmed in MATLAB to fit (4.4) and (4.13) to the NLOS wearable measurement data.

As an example of the model fitting, Figures 4.3 and 4.4 show that the PDFs of the $\mathcal{F}$ and η-μ / inverse gamma composite fading models fitted to the measurement data for the chest (Figure 4.3) and waist (Figure 4.4) positioned antenna within each environment. It is clear that both the $\mathcal{F}$ and η-μ / inverse gamma composite fading models provided an excellent agreement with the empirical data for all of the considered cases.

Tables 4.1 provides the parameter estimates for the $\mathcal{F}$ and η-μ / inverse gamma composite models for all of the wearable channels. For all of the considered wearable channels, the m parameters were found to be approximately 1, suggesting that the composite fading conditions observed in wearable channels are similar to those for the Rayleigh / inverse gamma fading channels. Inspecting Table 4.1, it

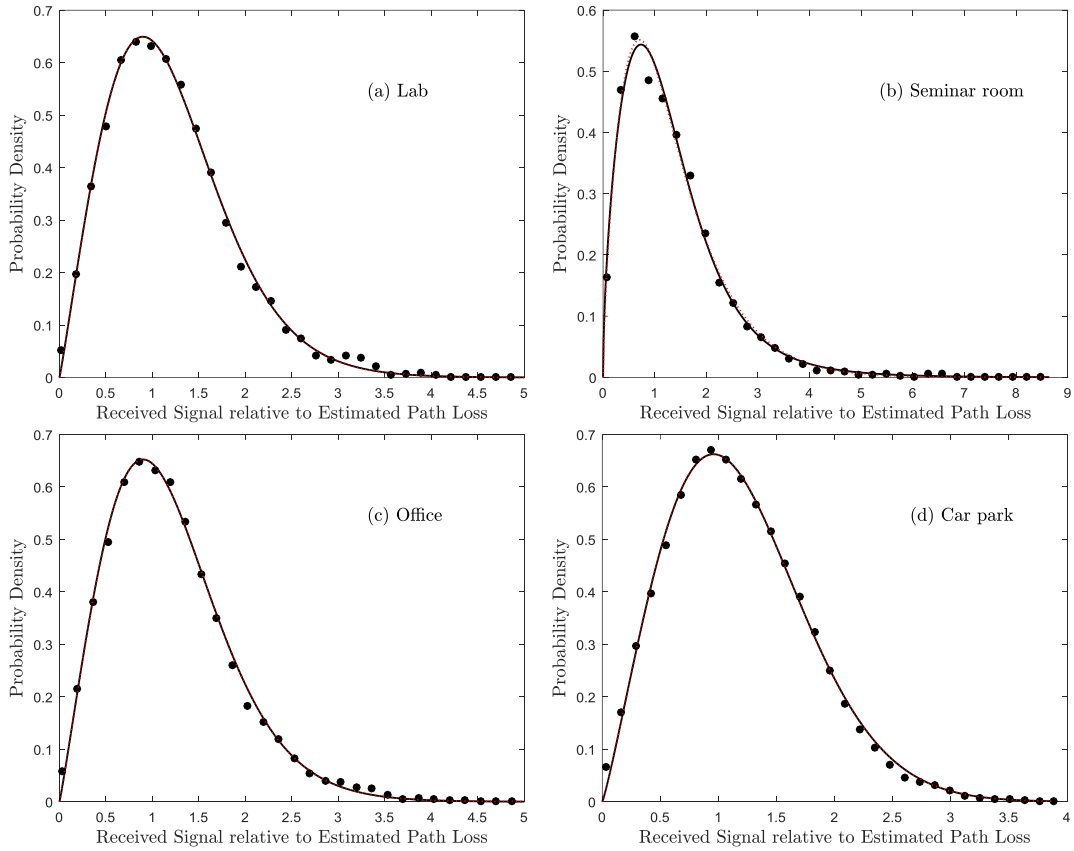

Figure 4.3: Empirical PDFs (circles) of the composite fading signal observed in the NLOS wearable links for the chest positioned antenna in the (a) laboratory, (b) seminar room, (c) open office and (d) car park environments compared to the theoretical PDFs of the $\mathcal{F}$ (black continuous lines) and η-μ / inverse gamma (red dotted lines) composite fading models.

can be seen that the η parameters were observed to be unity (i.e. $\eta = 1$) with the exception of the chest positioned antenna in the seminar environment, indicating that the scattered wave power of the in-phase and quadrature components was found to be identical. As expected, when $\eta = 1$ the parameter estimates for the η-μ / inverse gamma composite model were equivalent to those for the $\mathcal{F}$ composite fading model. For example, for the case of the chest positioned antenna in the open office environment, the η and μ parameters were 1.00 and 0.52 respectively and the m parameter was 1.04 while the m_s and Ω parameters were the same (i.e. $m_s = 9.04$ and $\Omega = 1.64$). The Nakagami-m distribution can be obtained by setting $\mu = m$ and $\mu \to 0$ or $\mu \to \infty$ in *Format* 1 as well as $\mu = m/2$ and $\eta \to 1$ in *Format* 1. Consequently, the η-μ / inverse gamma composite fading model ($\eta = 1$, $\mu = 0.52$, Ω =1.64 and $m_s = 9.04$) can be reduced to the $\mathcal{F}$ composite

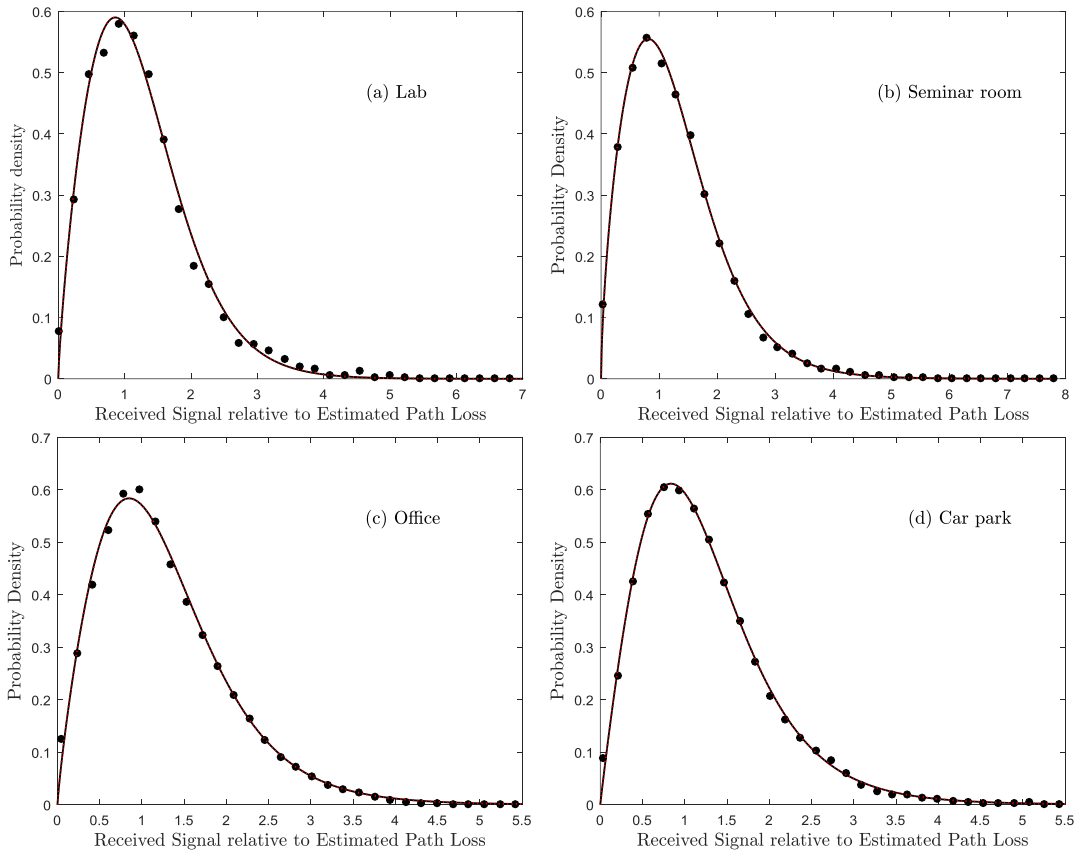

Figure 4.4: Empirical PDFs (circles) of the composite fading signal observed in the NLOS wearable links for the waist positioned antenna in the (a) laboratory, (b) seminar room, (c) open office and (d) car park environments compared to the theoretical PDFs of the $\mathcal{F}$ (black continuous lines) and η-μ / inverse gamma (red dotted lines) composite fading models.

fading model (m = 1.04, Ω =1.64 and m_s = 9.04).

4.7 A Comparison with other Composite Fading Models

To demonstrate the utility of the $\mathcal{F}$ and η-μ / inverse gamma composite fading models, their AICc values were evaluated and compared with those for other composite fading models associated with the NLOS channel conditions, namely K_G, η-μ / gamma and η-μ / inverse Gaussian composite fading models. To this end, their respective parameters were first estimated using the same approach (i.e. a non-linear least squares) used for the parameter estimates of the $\mathcal{F}$ and η-μ /

Table 4.1: Parameter estimates of the $\mathcal{F}$ and η-μ / inverse gamma models for all of the considered NLOS wearable channel measurement data.

Environments	Positions	$\mathcal{F}$ model			η-μ / inverse gamma model			
		m	Ω	m_s	η	μ	Ω	m_s
Laboratory	Chest	1.04	1.65	8.92	1.00	0.52	1.65	8.92
	Waist	0.90	1.78	7.05	1.00	0.45	1.78	7.05
Seminar	Chest	0.79	1.74	2.54	0.21	0.41	2.17	5.4
	Waist	0.82	1.86	5.01	1.00	0.41	1.86	5.01
Office	Chest	1.04	1.64	9.04	1.00	0.52	1.64	9.04
	Waist	0.92	1.76	4.29	1.00	0.46	1.76	4.29
Car park	Chest	1.07	1.74	50.00	1.00	0.53	1.74	50.00
	Waist	0.98	1.62	3.80	1.00	0.49	1.62	3.80

inverse gamma composite fading models. Then the five candidate models were ranked according to their AICc values as given in Table 4.2. It was observed that either the $\mathcal{F}$ composite fading model or the η-μ / inverse gamma composite fading model was determined as the best model for all of the considered cases with the exception of the waist positioned antenna in office area and car park environments in which the K_G model was selected as the best model. Nevertheless, as shown in Figure 4.5, the $\mathcal{F}$ and η-μ / inverse gamma composite fading models also provided an excellent fit to measurement data compared to the K_G model.

As discussed in Section 4.6, when η is equal to unity (i.e. $\eta = 1$) the η-μ / inverse gamma model is equivalent to the $\mathcal{F}$ composite fading model and thus they provided the same fit to the measurement data as shown in Figures 4.4 and 4.5. However, the $\mathcal{F}$ composite fading model has three parameters (i.e. m, Ω and m_s) while the η-μ / inverse gamma model contains four parameters (i.e. η, μ, Ω and m_s). As a result, although they provided the same fit to measurement data, the $\mathcal{F}$ composite fading model was selected as the best model because the $\mathcal{F}$ composite fading model has less number of parameters compared to the η-μ / inverse gamma model. In contrast, when η is not equal to unity (i.e. $\eta \neq 1$) the η-μ / inverse gamma model was selected as the best model (e.g. the chest positioned antenna in the seminar environment).

Table 4.2: AICc rank for all of the considered NLOS wearable channel measurement data

Environments	Positions	$\mathcal{F}$	η-μ / inverse gamma	K_G	η-μ / gamma	η-μ / inverse Gaussian
Laboratory	Chest	**1**	2	4	5	3
	Waist	**1**	2	4	5	3
Seminar	Chest	2	**1**	3	5	4
	Waist	**1**	2	3	4	5
Office	Chest	**1**	2	4	5	3
	Waist	3	4	**1**	2	5
Car park	Chest	**1**	2	5	3	4
	Waist	2	3	**1**	5	4

4.8 Conclusion

In this Chapter, two composite fading models, namely $\mathcal{F}$ and η-μ / inverse gamma composite fading models, have been presented to characterize the composite fading signal observed in NLOS wearable communications channels. The fundamental statistics of the $\mathcal{F}$ composite fading model, such as the PDF, CDF, MGF, higher order moments and AF, have been obtained in convenient closed-form expressions. For the η-μ / inverse gamma composite fading model, the PDF, higher order moments and AF have been obtained in closed-form while the CDF and MGF have been expressed using infinite series representations (i.e. in analytical solutions). Both the $\mathcal{F}$ and η-μ / inverse gamma composite fading models include many well-known distributions as special cases when they coincide with the Nakagami-m and η-μ fading models respectively. Furthermore, it has also been shown that they can be used to approximate other composite fading models found in the literature.

The versatility of the proposed $\mathcal{F}$ and η-μ / inverse gamma composite fading models has been validated using a range of the NLOS wearable channel measurements. It has been shown that the parameter estimates for the η-μ / inverse gamma composite model were equivalent to those for the $\mathcal{F}$ composite fading model when $\eta = 1$ (i.e. the scattered wave power ratio between the in-phase

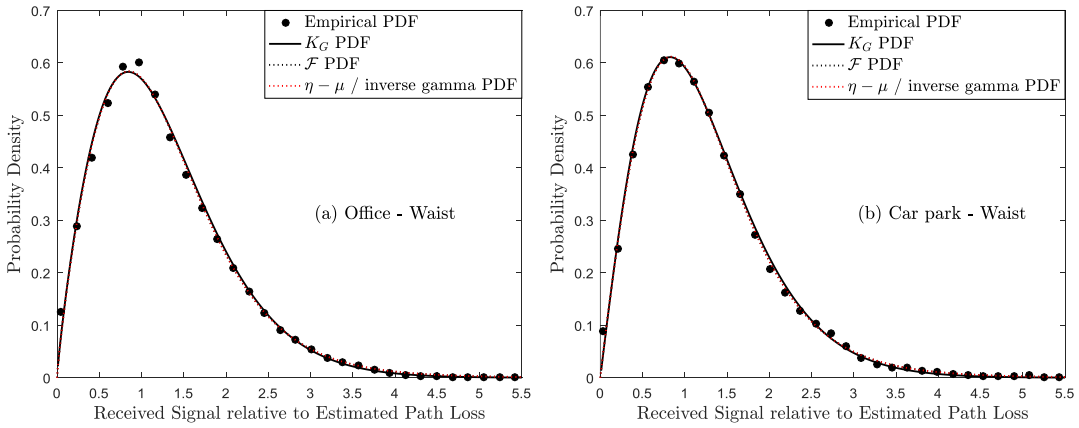

Figure 4.5: Empirical PDF (circles), the K_G (black continuous lines), $\mathcal{F}$ (black dotted lines) and η-μ / inverse gamma PDFs (red dotted lines) for the waist positioned antenna in the open office and car park environments.

and quadrature components of each cluster of multipath was found to be unity). Consequently, the $\mathcal{F}$ and η-μ / inverse gamma composite fading models provided the same fit to the measurement data when $\eta = 1$. Nonetheless, using an analysis of the AICc, it has been found that the $\mathcal{F}$ composite fading model was determined as the most likely candidate model due to its reliance on a fewer number of parameters compared to the η-μ / inverse gamma model (i.e. parsimony). On the contrary, the η-μ / inverse gamma model was selected as the best model when $\eta \neq 1$ (i.e. the scattered wave power of the in-phase and quadrature components of each cluster of multipath was found to be different).

Chapter 5

Mitigation of Micro and Macro Fading

In wearable communications, the received signal can be subject to both multipath and shadowing. At microwave frequencies, multipath fading is manifested by scattering and reflections from the human body and nearby objects. In contrast, shadowing is caused when the dominant and scattered components are obscured by the wearer's body and surrounding obstacles and people. All of these factors can significantly impact the overall performance of wearable systems.

One well-known method of mitigating the deleterious effects of fading and improving the signal reliability and the performance of wireless communications systems is to employ diversity reception techniques. For wearable systems, spatial diversity schemes are commonly applied compared to other diversity techniques as they generally require no additional transmit power or bandwidth. These are often implemented using two main configurations, namely micro- and macro-diversity, which are differentiated according to the allocations of the antennas. Therefore, in this Chapter, micro-diversity and macro-diversity systems are utilised to investigate the potential improvement in signal reliability which may be achieved for wearable communications channels through the mitigation of multipath and shadowing respectively.

5.1 Micro-Diversity

In a micro-diversity system, the antennas are typically positioned within a single base station with a separation distance of the order of (or shorter than) the signal wavelength. Micro-diversity is generally employed to overcome the effect of multipath fading since sufficiently separated antennas within a single base station are expected to experience different multipath. Over the last few years, a number of studies on micro-diversity techniques have been conducted in the context of wearable communications [26–31, 98, 99]. Although an improvement in outage probability, a reduction in power consumption and a low switching rate were investigated using cooperative diversity with an SEC scheme in [98, 99], the majority of studies on micro-diversity techniques for wearable communications have considered only PSC, EGC and MRC schemes [26–31]. As discussed in Chapter 1.2, these combining schemes can be resource consuming compared to simpler TSC schemes and therefore they may be impractical for implementation in wearable communications systems which favour low complexity, low cost and ultra-low power architecture.

Therefore, this Chapter investigates the possible signal reliability improvement for indoor wearable communications channels operating at 5.8 GHz using a switched combining based micro-diversity system. Since no further benefit can be obtained from having more than two signal branches in an SSC scheme, dual-branch SSC, L-branch SEC and L-branch SECps schemes are considered. Furthermore the fading observed at the output of each switched diversity combiner for wearable communications systems operating in Nakagami-m multipath fading channels has been statistically characterized using diversity specific analytical equations. It is worth highlighting that analytical expressions for the output envelope are presented instead of those for the output SNR since it is difficult to measure the time-varying SNR in practice.

5.1.1 Dual-branch SSC, L-branch SEC and L-branch SECps Operating over Nakagami-m Multipath Fading Channels

There are a number of studies which describe the statistical behaviour of multipath fading in wearable communications channels using the Nakagami-m distribution [21, 51, 52, 54]. The PDF and CDF of the instantaneous SNR over a Nakagami-m multipath fading channel can be expressed as follows

$$f_{\gamma}(\gamma) = \frac{m^{m}\gamma^{m-1}}{\Gamma(m)\,\bar{\gamma}^{m}} \exp\left(-\frac{m\gamma}{\bar{\gamma}}\right) \tag{5.1}$$

$$F_{\gamma}(\gamma) = \frac{\Gamma_{l}\left(m, \frac{m\gamma}{\bar{\gamma}}\right)}{\Gamma(m)} \tag{5.2}$$

where $\Gamma_{l}(\cdot,\cdot)$ represents the lower incomplete gamma function [53, Eq. (8.350.1)]. For dual-branch SSC systems in which the input SNR is i.i.d. at both branches, the PDF of the output SNR can be expressed from (2.13) such that[1]

$$f_{SSC}(\gamma) = \begin{cases} F_{\gamma}(\gamma_{T})\, f_{\gamma}(\gamma), & \gamma < \gamma_{T} \\ \left[1 + F_{\gamma}(\gamma_{T})\right] f_{\gamma}(\gamma), & \gamma \geq \gamma_{T}. \end{cases} \tag{5.3}$$

By substituting (5.1) and (5.2) into (5.3), the PDF of the output SNR for dual-branch SSC operating over i.i.d. Nakagami-m multipath fading channels can be obtained as follows

$$f_{SSC}(\gamma) = \begin{cases} \left[\dfrac{\Gamma_{l}\left(m, \frac{m\gamma_{T}}{\bar{\gamma}}\right)}{\Gamma(m)}\right] \dfrac{m^{m}\gamma^{m-1}}{\Gamma(m)\,\bar{\gamma}^{m}} \exp\left(-\dfrac{m\gamma}{\bar{\gamma}}\right), & \gamma < \gamma_{T} \\ \left[1 + \dfrac{\Gamma_{l}\left(m, \frac{m\gamma_{T}}{\bar{\gamma}}\right)}{\Gamma(m)}\right] \dfrac{m^{m}\gamma^{m-1}}{\Gamma(m)\,\bar{\gamma}^{m}} \exp\left(-\dfrac{m\gamma}{\bar{\gamma}}\right), & \gamma \geq \gamma_{T}. \end{cases} \tag{5.4}$$

[1] For i.i.d case, π_{i} in (2.14) is equivalent to $1/L$ (i.e. $\pi_{i} = 1/2$ for dual-branch SSC systems).

Then, performing a simple transformation of variables using the relationship of $\gamma = r^2\bar{\gamma}/\Omega$, the PDF of dual-branch SSC envelope, R, can be obtained as follows

$$f_{SSC}(r) = \begin{cases} \left[\dfrac{\Gamma_l\left(m, \frac{mr_T^2}{\Omega}\right)}{\Gamma(m)}\right] \dfrac{2m^m r^{2m-1}}{\Gamma(m)\,\Omega^m} \exp\left(-\dfrac{mr^2}{\Omega}\right), & r < r_T \\ \left[1 + \dfrac{\Gamma_l\left(m, \frac{mr_T^2}{\Omega}\right)}{\Gamma(m)}\right] \dfrac{2m^m r^{2m-1}}{\Gamma(m)\,\Omega^m} \exp\left(-\dfrac{mr^2}{\Omega}\right), & r \geq r_T. \end{cases} \tag{5.5}$$

For L-branch SEC systems in which the SNR is i.i.d. at each of the L branches, the PDF of output SNR can be expressed from (2.15) as follows[1]

$$f_{SEC}(\gamma) = \begin{cases} \left[F_\gamma(\gamma_T)\right]^{L-1} f_\gamma(\gamma), & \gamma < \gamma_T \\ \sum\limits_{i=0}^{L-1} \left[F_\gamma(\gamma_T)\right]^i f_\gamma(\gamma), & \gamma \geq \gamma_T. \end{cases} \tag{5.6}$$

Similarly, the PDF of the output envelope, R, of an L-branch SEC operating over i.i.d. Nakagami-m multipath fading channels can be obtained by substituting (5.1) and (5.2) into (5.6), such that

$$f_{SEC}(\gamma) = \begin{cases} \left[\dfrac{\Gamma_l\left(m, \frac{m\gamma_T}{\bar{\gamma}}\right)}{\Gamma(m)}\right]^{L-1} \dfrac{m^m \gamma^{m-1}}{\Gamma(m)\,\bar{\gamma}^m} \exp\left(-\dfrac{m\gamma}{\bar{\gamma}}\right), & \gamma < \gamma_T \\ \sum\limits_{i=0}^{L-1} \left[\dfrac{\Gamma_l\left(m, \frac{m\gamma_T}{\bar{\gamma}}\right)}{\Gamma(m)}\right]^i \dfrac{m^m \gamma^{m-1}}{\Gamma(m)\,\bar{\gamma}^m} \exp\left(-\dfrac{m\gamma}{\bar{\gamma}}\right), & \gamma \geq \gamma_T. \end{cases} \tag{5.7}$$

Then the PDF of output envelope of an L-branch SEC can be obtained by performing the same transformation of variables as follows

[1]For i.i.d case, χ_i in (2.16) is equivalent to $1/L$ (i.e. $\chi_i = 1/L$ for L-branch SEC systems).

$$f_{SEC}(r) = \begin{cases} \left[\dfrac{\Gamma_l\left(m, \frac{mr_T{}^2}{\Omega}\right)}{\Gamma(m)}\right]^{L-1} \dfrac{2m^m r^{2m-1}}{\Gamma(m)\Omega^m} \exp\left(-\dfrac{mr^2}{\Omega}\right), & r < r_T \\ \sum\limits_{i=0}^{L-1} \left[\dfrac{\Gamma_l\left(m, \frac{mr_T^2}{\Omega}\right)}{\Gamma(m)}\right]^i \dfrac{2m^m r^{2m-1}}{\Gamma(m)\Omega^m} \exp\left(-\dfrac{mr^2}{\Omega}\right), & r \geq r_T. \end{cases} \tag{5.8}$$

It has been shown that an SEC scheme with two branches can provide the same performance as a dual-branch SSC scheme, accordingly (5.7) and (5.8) reduces to (5.4) and (5.5) respectively when $L = 2$.

For L-branch SECps systems in which the SNR is i.i.d. at each of the L branches, the PDF of output SNR can be expressed from (2.17) as follows

$$f_{SECps}(\gamma) = \begin{cases} L\left[F_\gamma(\gamma)\right]^{L-1} f_\gamma(\gamma), & \gamma < \gamma_T \\ \sum\limits_{i=0}^{L-1} \left[F_\gamma(\gamma_T)\right]^i f_\gamma(\gamma), & \gamma \geq \gamma_T. \end{cases} \tag{5.9}$$

Again, using the same approach used for SSC and SEC schemes above, the PDFs of the output SNR and envelope of an L-branch SECps over i.i.d. Nakagami-m multipath fading channels can be obtained respectively

$$f_{SECps}(\gamma) = \begin{cases} L\left[\dfrac{\Gamma_l\left(m, \frac{m\gamma}{\bar{\gamma}}\right)}{\Gamma(m)}\right]^{L-1} \dfrac{m^m \gamma^{m-1}}{\Gamma(m)\bar{\gamma}^m} \exp\left(-\dfrac{m\gamma}{\bar{\gamma}}\right), & \gamma < \gamma_T \\ \sum\limits_{i=0}^{L-1} \left[\dfrac{\Gamma_l\left(m, \frac{m\gamma_T}{\bar{\gamma}}\right)}{\Gamma(m)}\right]^i \dfrac{m^m \gamma^{m-1}}{\Gamma(m)\bar{\gamma}^m} \exp\left(-\dfrac{m\gamma}{\bar{\gamma}}\right), & \gamma \geq \gamma_T \end{cases} \tag{5.10}$$

$$f_{SECps}(r) = \begin{cases} L\left[\dfrac{\Gamma_l\left(m, \frac{mr^2}{\Omega}\right)}{\Gamma(m)}\right]^{L-1} \dfrac{2m^m r^{2m-1}}{\Gamma(m)\Omega^m} \exp\left(-\dfrac{mr^2}{\Omega}\right), & r < r_T \\ \sum\limits_{i=0}^{L-1} \left[\dfrac{\Gamma_l\left(m, \frac{mr_T^2}{\Omega}\right)}{\Gamma(m)}\right]^i \dfrac{2m^m r^{2m-1}}{\Gamma(m)\Omega^m} \exp\left(-\dfrac{mr^2}{\Omega}\right), & r \geq r_T. \end{cases} \tag{5.11}$$

5.1.2 Measurement Setup and Experiments

The field measurements were conducted at 5.8 GHz in an indoor laboratory room (4.75 m × 9.14 m × 2.70 m) as shown in Figure 5.1(a). The hypothetical base station RX consisted of four identical sleeve dipole antennas aligned horizontally along a straight line with an equal spacing of half-wavelength. These four RX antennas were mounted such that they were vertically polarized on a non-conductive height adjustable stand at an elevation of 0.83 m above the floor level. They were connected to ports 1, 2, 3 and 4 of a Rohde & Schwarz ZVB-8 VNA using low-loss coaxial cables and configured to record the magnitude of the b_1 wave quantity incident on ports 1, 2, 3 and 4 with a bandwidth of 10 kHz. The magnitude of the b_1 measurements were automatically collected and stored on a laptop through a LAN connection, providing an effective channel sampling frequency of 56 Hz. A pre-measurement calibration was performed to reduce the effects of known systematic errors and cable loss using a Rohde & Schwarz ZV-Z51 calibration unit.

For the TX, an ML5805 transceiver manufactured by RFMD was configured to generate a continuous wave signal with a power level of +17.6 dBm at 5.8 GHz. It was mounted in a vertically polarized orientation and parallel to the central-chest region of an adult male of height 1.83 m and weight 80 kg. The antennas used by both the TX and hypothetical base station RX were omnidirectional sleeve dipole antennas with +2.3 dBi gain (Mobile Mark model PSKN3-24/55S2). The measured azimuthal radiation patterns for the sleeve dipole antenna in free space and placed at the central-chest region are presented in Figure 5.1(b). It should be noted that the black arrow in Figure 5.1(b) denotes the direction that the test subject was facing. In the experiments conducted here, two different measurement scenarios were considered. These were LOS and NLOS walking movements where the test subject walked towards and then away from the RX in a straight line (between 1 m point and 9 m point away from the RX). They are designed to emulate the channel characteristics which may be present in indoor

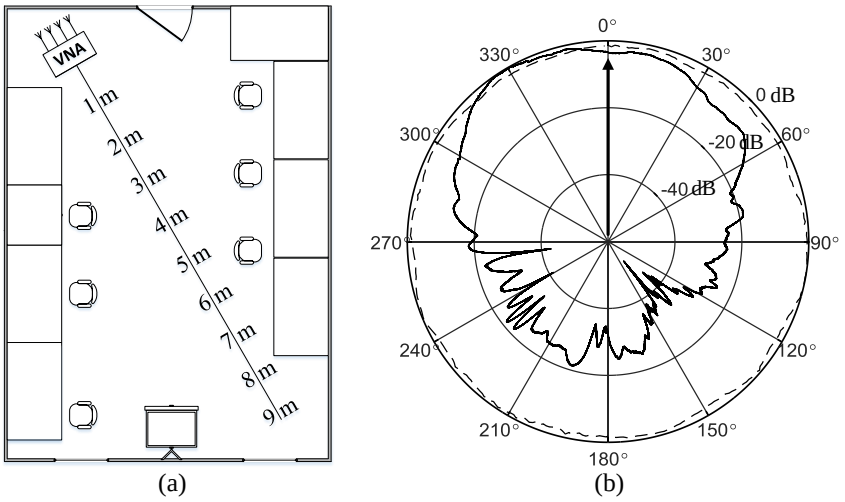

Figure 5.1: (a) Indoor laboratory environment (43.42 m^2) and (b) the measured azimuthal radiation patterns for the sleeve dipole antenna in free space (dashed lines) and located on the central-chest region (continuous lines) of the test subject.

wearable applications such as people tracking, fitness, monitoring systems for safety etc. To improve the validity and robustness of the parameter estimates obtained in this study, all measurements were repeated five times for each of the scenarios. The mean recorded noise thresholds were observed to be −98.5 dBm, −98.6 dBm, −98.6 dBm and −98.5 dBm for branches 1, 2, 3 and 4, respectively. The minimum data set sizes (from the individual trials) were 2417 and 2119 for the LOS and NLOS walking scenarios, respectively.

5.1.3 Correlation and Power Imbalance

For a micro-diversity system to be effective, each RX branch should receive statistically independent versions of the transmitted signal reducing the likelihood that all branches are experiencing correlated fading. In general, two signals are said to be *effectively* de-correlated if their cross-correlation coefficient is less than a certain threshold (typically 0.7[1]) [80]. Furthermore, each RX branch should have similar average received power (i.e. low power imbalance). The cross-correlation coefficient and power imbalance between all possible pairs of RX branches were calculated using the approach described in Chapter 2.7 and their mean values av-

[1]To provide sufficient diversity gain, the envelope correlation coefficient should be 0.7 or less.

Table 5.1: Mean cross-correlation coefficient and mean power imbalance between all possible pairs of branches.

All Possible Pairs	Cross-Correlation Coefficient		Power Imbalance (dB)	
	LOS	NLOS	LOS	NLOS
(1,2)	0.06	0.17	2.0	0.6
(1,3)	0.13	0.12	3.7	1.2
(1,4)	0.04	0.03	1.1	0.4
(2,3)	0.06	0.04	1.9	0.5
(2,4)	0.05	0.04	0.7	0.5
(3,4)	0.07	0.11	2.3	1.1

eraged over all of the trials are shown in Table 5.1. It is clear that the estimated cross-correlation coefficients were always less than 0.2 for all of the considered cases. Additionally, the mean power imbalances averaged over all possible pairs were 2.0 dB (LOS) and 0.7 dB (NLOS) while the maximum power imbalances were 3.7 dB (LOS) and 1.2 dB (NLOS). The low cross-correlation coefficients and power imbalances obtained suggest that an RX equipped with multiple antennas should be adequately positioned to supply a worthwhile DG.

5.1.4 Diversity Gain

The performance of SSC, SEC and SECps schemes for use in wearable communications was empirically evaluated in terms of their DGs. Here, the DG is defined as the ratio of the signal level of the diversity combiner and that of the branch with the highest mean for a given probability of signal reliability. It is worth highlighting that all DG calculations were made at a signal reliability of 90 %. As an additional quantitative measure, the DGs of SSC, SEC and SECps schemes were compared with those calculated for a PSC scheme.

Figure 5.2 shows a short excerpt of the received signal power at branches 1 and 4 along with the output signal power of the hypothetical dual-branch SSC, SEC and SECps with a switching threshold of -66 dBm for the LOS walking scenario during the first trial. As shown in Figure 5.2, when branch switching occurs the

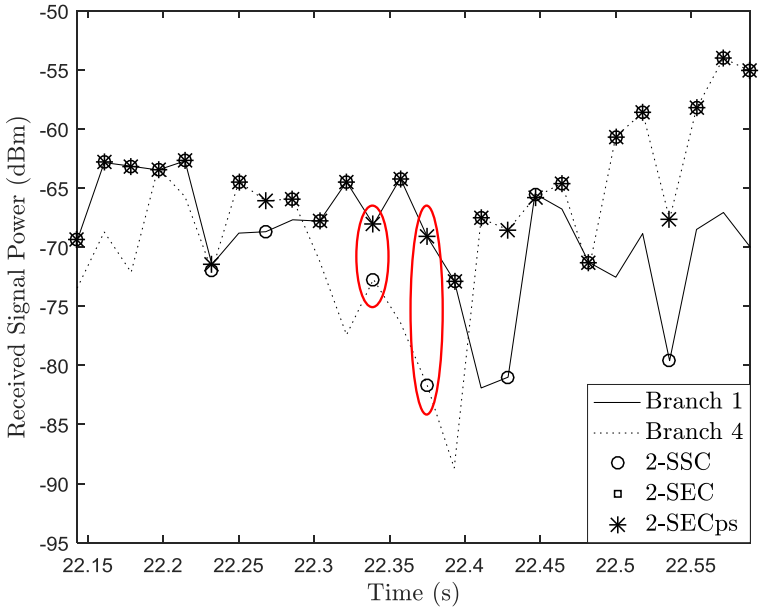

Figure 5.2: Received signal power at branches 1 and 4 alongside the output signal power of dual-branch SSC, SEC and SECps with a switching threshold of −66 dBm for the LOS walking scenario during the first trial.

dual-branch SSC and SEC schemes operate identically, but dual-branch SECps works slightly differently. This can be explained from the way that the TSC system with dual-branch SSC and SEC switches to the other branch whenever the signal level of currently selected branch falls below the predetermined switching threshold. This path switching occurs irrespective of whether the signal level of the other branch is above or below the switching threshold. Moreover, the signal level of the other branch can be even lower than the one for currently selected branch. In this case, the performance of TSC systems is degraded instead of improved.

Similar to dual-branch SEC, a TSC system using a dual-branch SECps scheme examines and finds an acceptable branch which is above the switching threshold. However, unlike the SEC scheme, after examining all branches, the SECps scheme switches to the branch with the highest signal level instead of the last examined branch when no acceptable one is found. As an example of this behaviour, consider two red ellipses shown in Figure 5.2, here, the dual-branch SSC and SEC systems switched from branch 1 to 4 despite the fact that branch 4 had an even lower signal level compared to branch 1 whereas the dual-branch SECps stayed

Table 5.2: Mean DGs for dual-branch SSC, dual- and four-branch SEC, dual- and four-branch SECps, dual- and four-branch PSC in the LOS and NLOS walking scenarios with three different switching thresholds.

Scenarios	Threshold (dBm)	Diversity Gain (dB)						
		Dual-Branch				Four-Branch		
		SSC	SEC	SECps	PSC	SEC	SECps	PSC
LOS	−80	−0.1	−0.1	−0.1	4.2	−0.5	−0.5	5.8
	−60	1.8	1.8	4.1		2.7	5.4	
	−40	−0.9	−0.9	4.2		−2.2	5.8	
NLOS	−80	1.6	1.6	1.6	5.4	1.5	1.5	7.9
	−60	1.1	1.1	5.4		2.2	7.9	
	−40	0.1	0.1	5.4		0.1	7.9	

with branch 1.

Table 5.2 shows the mean DG statistics for dual-branch SSC, SEC and SECps and four-branch SEC and SECps for both the LOS and NLOS walking scenarios with three different switching thresholds, namely low (−80 dBm), medium (−60 dBm) and high (−40 dBm). These values were determined based on the average received signal power levels measured at each branch which ranged from −65.9 dBm to −55.0 dBm. For comparison, the mean DGs for dual- and four-branch PSC are also shown in Table 5.2. It should be noted that branches 1 and 4 were chosen for the analysis of dual-branch SSC, SEC, SECps and PSC. As expected, the DGs for dual-branch SSC were the same as those for dual-branch SEC. Among the three different TSC schemes, the SECps scheme provided the highest DG. Also from Table 5.2, it is clear that the estimated DGs for both the dual- and four-branch TSC systems were different according to the switching threshold.

To further investigate the effect of different switching thresholds on the achievable DG, Figure 5.3 shows the mean DGs for dual-branch SSC, four-branch SEC and SECps with different switching threshold values ranging between −90 dBm and −30 dBm for both the LOS and NLOS walking scenarios. As shown in Figure 5.3, the performance of all the TSC schemes strongly depends on the pre-

determined switching threshold and there exists an optimum switching threshold which maximizes the DG. It is clear that a greater DG was achieved by all combiners for the NLOS scenario compared to the LOS scenario when the optimum switching threshold was chosen. It was also observed that the DG obtained for four-branch SECps with the optimum switching threshold was the same as the one for the respective PSC system presented in Table 5.2.

However, when the switching threshold was considerably low or high compared to the average received signal power level, there was no benefit to using a TSC scheme. Interestingly, in contrast with dual-branch SSC and four-branch SEC, the DG for four-branch SECps kept the same DG beyond the optimum switching threshold. This is most likely due to the fact that the SECps scheme examines all branches and selects the branch with the highest signal level when there is no acceptable branch available. Therefore, when the switching threshold is high and the signal level of all diversity branches are below the predetermined switching threshold, it operates as a PSC scheme, monitoring the signal level of all branches continuously and selecting the branch with the highest signal level.

5.1.5 Modelling of the Fading Observed at the Combiner Output

Modelling of the fading characteristics at the output of the hypothetical combiners was performed using the models presented in Chapter 5.1.1. The Nakagami m and Ω parameters were estimated using a non-linear least squares routine programmed in MATLAB to fit (5.5), (5.8) and (5.11) to the measured data. To allow a direct comparison between the fading signals, the rms signal level was removed from the output envelope. As an example of the results of the model fitting, the PDFs of four-branch SEC and SECps with three different switching thresholds for the LOS walking scenario during the second trial are presented in Figure 5.4. The PDFs of four-branch SEC and SECps were in very good agreement with the measured data confirming the validity of the modelling approach utilised

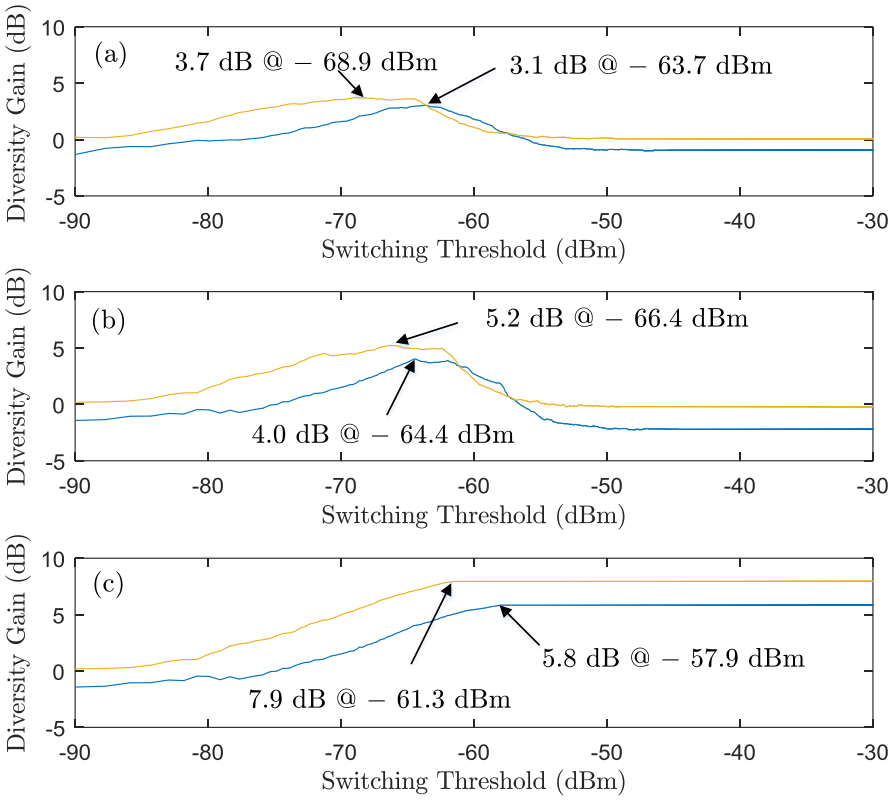

Figure 5.3: Mean DG of (a) dual-branch SSC, (b) four-branch SEC and (c) four-branch SECps for increasing values of the switching threshold for the LOS (blue continuous lines) and NLOS (yellow continuous lines) walking scenarios along with the maximum achievable DG at the optimum switching threshold.

here. As a measure of the goodness-of-fit, the RAD between the empirical and theoretical PDFs was calculated using (2.22) and the corresponding RAD results are presented in Table 5.3. For all the measurements, the estimated RAD values were always less than 0.04, indicating that the theoretical models provided an adequate fit to the measured wearable channel data.

Table 5.3 also provides the mean parameter estimates averaged over all of the trials for dual-branch SSC, four-branch SEC and four-branch SECps in the LOS and NLOS walking scenarios with three different switching thresholds. It is clear that the mean Ω parameters (i.e. spread parameter) for the medium switching threshold (-60 dBm) were smaller than those obtained for the low and high switching thresholds with the exception of the SECps scheme. The subsequent narrowing effect on the output envelopes can be observed in Figures 5.4(b) and 5.4(e). When compared with the PDFs for the low switching threshold shown in

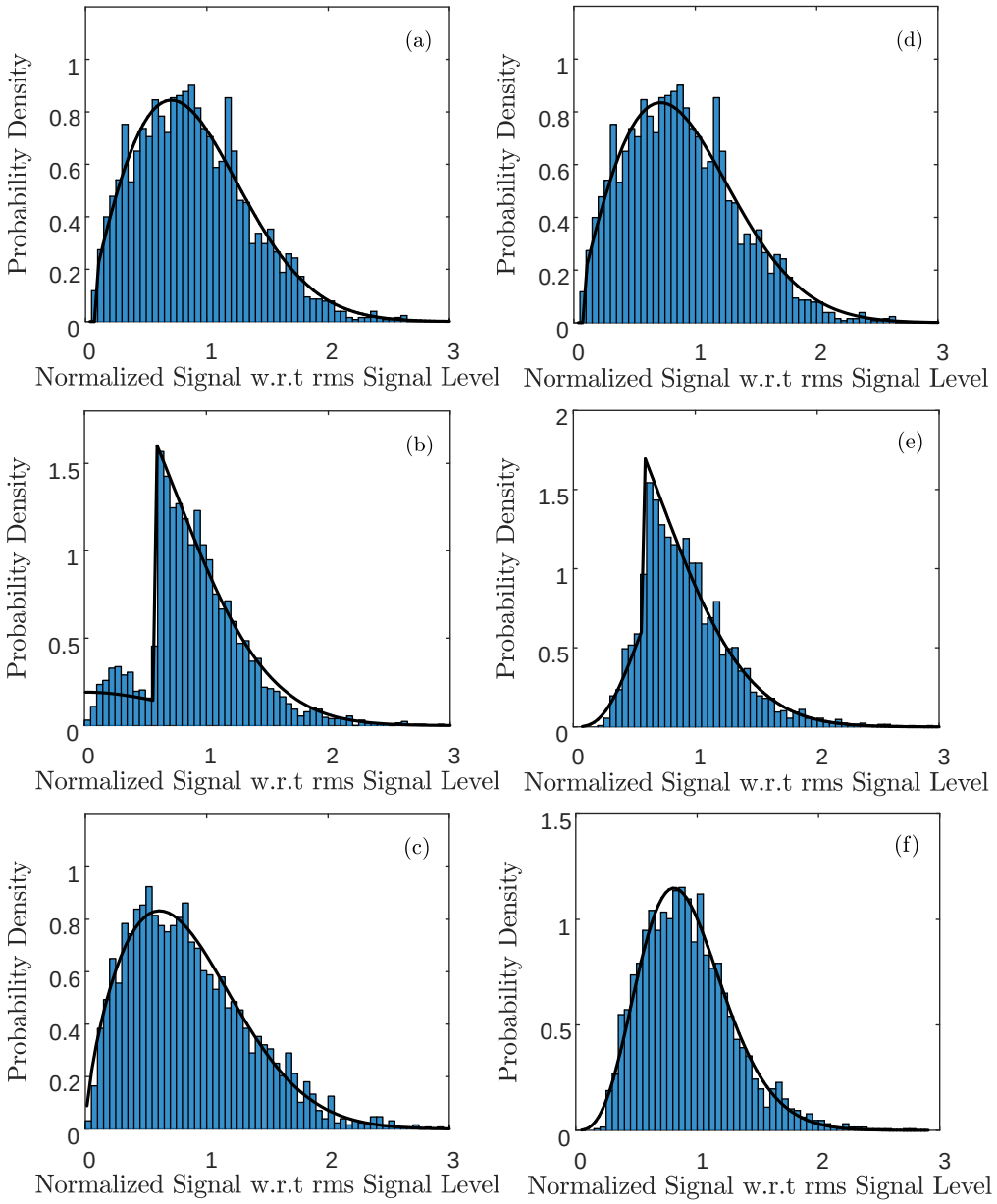

Figure 5.4: Empirical (bars) and theoretical (continuous lines) PDFs for the LOS walking scenario during the second trial: (a) 4-SEC with low threshold (−80 dBm); (b) 4-SEC with medium threshold (−60 dBm); (c) 4-SEC with high threshold (−40 dBm); (d) 4-SECps with low threshold (−80 dBm); (e) 4-SECps with medium threshold (−60 dBm); (f) 4-SECps with high threshold (−40 dBm).

Figures 5.4(a) and 5.4(d), it is obvious that they had a lower number of signal observations at low levels, suggesting that improvements in the received signal were achieved. As shown in Table 5.3, this observation is also supported by the mean signal power of the output envelopes ($\overline{P}$) for the medium switching threshold which were greater than those for the low switching threshold.

Table 5.3: Mean parameter estimates, mean signal power of the output envelopes and mean RAD for dual-branch SSC, four-branch SEC and four-branch SECps in the LOS and NLOS scenarios for different switching thresholds.

Threshold (dBm)	Dual-Branch SSC				Four-Branch SEC				Four-Branch SECps			
	$\overline{m}$	$\overline{\Omega}$	$\overline{P}$ (dBm)	$\overline{\text{RAD}}$	$\overline{m}$	$\overline{\Omega}$	$\overline{P}$ (dBm)	$\overline{\text{RAD}}$	$\overline{m}$	$\overline{\Omega}$	$\overline{P}$ (dBm)	$\overline{\text{RAD}}$
LOS Walking Scenario												
−80	0.90	0.92	−65.1	0.009	0.94	0.93	−66.4	0.018	0.94	0.93	−66.4	0.018
−60	0.74	0.71	−63.3	0.016	0.78	0.61	−63.3	0.037	0.76	0.58	−63.1	0.028
−40	0.88	0.88	−65.6	0.010	0.85	0.85	−67.4	0.020	0.53	0.36	−61.1	0.021
NLOS Walking Scenario												
−80	0.92	0.86	−74.3	0.014	0.94	0.84	−75.1	0.019	0.94	0.83	−75.1	0.022
−60	0.73	0.63	−71.7	0.014	0.60	0.46	−70.6	0.038	0.55	0.41	−69.8	0.039
−40	0.84	0.85	−74.2	0.015	0.92	0.89	−75.3	0.008	0.58	0.37	−69.0	0.042

When the switching threshold is high (-40 dBm) the selected branch for four-branch SEC was switched almost every single time slot, even if the currently selected branch had the highest signal level. This unnecessary path switching causes considerable signal fluctuation. However, for the reasons discussed above, the four-branch SECps scheme selects the branch with the highest signal level and thus the selected branch is not switched every single time slot. Therefore four-branch SEC [Figure 5.4(c)] had an empirical PDF with a greater spread and a larger number of signal observations at low signal levels compared to four-branch SECps [Figure 5.4(f)].

5.2 Macro-Diversity

In a macro-diversity system, the antennas are often located in different, spatially separated base stations for which the spacing is much longer than the signal wavelength. In this instance, the antennas are expected to experience different shadowing hence macro-diversity is employed to mitigate these effects. Over the last few decades, a number of studies investigating the use of spatial diversity techniques have been performed in the context of wearable communications.

However, the majority of these studies have focused on micro-diversity systems positioned either on the human body or at a single base station with the aim of mitigating the impact of multipath fading. The use of micro-diversity may not be sufficient to overcome the arguably more critical signal degradations caused by random shadowing events induced by the human body and obstacles in the local surroundings.

To overcome the shadowing experienced in wearable communications channels, spatial diversity using antennas distributed across the human body has been proposed [32, 33]. For example, in [32], front and back positioned antennas used together with a PSC scheme provided mitigation of shadowing and an overall improvement in signal reliability in outdoor wearable communications channels at 2.45 GHz. In [33], six RX antennas were distributed across the front and back torso of the human body to help overcome the detrimental effects of shadowing in wearable communications within an indoor environment at 868 MHz. The benefit of having more than two signal branches was demonstrated by comparing the DGs between dual-branch and six-branch RX configurations. Nonetheless, as mentioned in Chapter 1.2, there are many drawbacks to operating diversity systems which are worn on the human body, including potential obtrusion to the user, the additional weight added to the wearable systems associated circuity and enclosures and also the extra drain on battery life.

Therefore, this Chapter also investigates the potential improvement in signal reliability for outdoor wearable communications channels operating at 868 MHz using macro-diversity arrangements based on L-base station SSC, L-base station SEC and L-base station SECps. The impact of different switching thresholds on the DG, number of path examinations and number of path switches of the various combiner outputs has been studied to emphasize the importance of selecting an appropriate switching threshold. Most importantly though, the fading behaviour observed at the output of switched diversity combiners, i.e. from the perspective of combiner output, has been statistically characterized using the diversity specific

equations which were developed under the assumption of i.n.i.d. Nakagami-m shadowing channels.

5.2.1 L-base Station SSC, SEC and SECps Operating over Nakagami-m Shadowing Channels

As well as modelling multipath fading, the Nakagami-m distribution can be used to describe shadowing of the signal amplitude owing to its relationship with the gamma distribution. It is already well established that the gamma distribution can be used to model shadowing of the signal power [59] and gamma and Nakagami-m random variables are related by a simple quadratic transformation. Accordingly the signal power or equivalently SNR over a Nakagami-m channel is distributed according to the gamma distribution [16, 100].

When the shadowing observed at each of the base stations is assumed to be i.n.i.d. the PDFs of the output SNR at L-base station SSC, L-base station SEC and L-base station SECps systems are given in (2.13), (2.15) and (2.17), respectively. Now substituting the Nakagami-m SNR PDF and CDF given in (5.1) and (5.2) into (2.13), (2.15) and (2.17), the corresponding PDFs of the output SNR of L-base station SSC, L-base station SEC and L-base station SECps systems operating over i.n.i.d. Nakagami-m shadowing channels can be respectively expressed respectively

$$f_{\mathrm{SSC}}(\gamma) = \begin{cases} \displaystyle\sum_{i=0}^{L-1} \left(\sum_{j=0}^{L-1} \frac{\Gamma(m_j)}{\Gamma_l\left(m_j, \frac{m_j \gamma_T}{\bar{\gamma}_j}\right)} \right)^{-1} \frac{m_i^{m_i} \gamma^{m_i - 1}}{\Gamma(m_i)\, \bar{\gamma}_i^{m_i}} \exp\left(-\frac{m_i \gamma}{\bar{\gamma}_i}\right), & \gamma < \gamma_T \\ \displaystyle\sum_{i=0}^{L-1} \left[\pi_i + \left(\sum_{j=0}^{L-1} \frac{\Gamma(m_j)}{\Gamma_l\left(m_j, \frac{m_j \gamma_T}{\bar{\gamma}_j}\right)} \right)^{-1} \right] \frac{m_i^{m_i} \gamma^{m_i - 1}}{\Gamma(m_i)\, \bar{\gamma}_i^{m_i}} \exp\left(-\frac{m_i \gamma}{\bar{\gamma}_i}\right), & \gamma \geq \gamma_T \end{cases} \tag{5.12}$$

where

$$\pi_i = \left(\sum_{j=0}^{L-1} \frac{\Gamma\left(m_j\right)}{\Gamma_l\left(m_j, \frac{m_j \gamma_T}{\bar{\gamma}_j}\right)} \right)^{-1} \frac{\Gamma\left(m_i\right)}{\Gamma_l\left(m_i, \frac{m_i \gamma_T}{\bar{\gamma}_i}\right)}, i = 0, 1, \ldots, L-1. \tag{5.13}$$

$$f_{\mathrm{SEC}}\left(\gamma\right) = \begin{cases} \sum_{i=0}^{L-1} \chi_i \left[\prod_{k=0, k\neq i}^{L-1} \frac{\Gamma_l\left(m_k, \frac{m_k \gamma_T}{\bar{\gamma}_k}\right)}{\Gamma\left(m_k\right)} \right] \frac{{m_i}^{m_i} \gamma^{m_i - 1}}{\Gamma\left(m_i\right) \bar{\gamma}_i^{m_i}} \exp\left(-\frac{m_i \gamma}{\bar{\gamma}_i}\right), & \gamma < \gamma_T \\ \sum_{i=0}^{L-1} \left[\sum_{j=0}^{L-1} \chi_{[(i-j)]_L} \prod_{k=0}^{j-1} \frac{\Gamma_l\left(m_{n_n}, \frac{m_{n_n} \gamma_T}{\bar{\gamma_{n_n}}}\right)}{\Gamma_l\left(m_{n_n}\right)} \right] \frac{{m_i}^{m_i} \gamma^{m_i - 1}}{\Gamma\left(m_i\right) \bar{\gamma}_i^{m_i}} \exp\left(-\frac{m_i \gamma}{\bar{\gamma}_i}\right), & \gamma \geq \gamma_T \end{cases} \tag{5.14}$$

where

$$\chi_i = \left[\sum_{j=0}^{L-1} \frac{\frac{\Gamma_l\left(m_{L-1}, \frac{m_{L-1}\gamma_T}{\bar{\gamma}_{L-1}}\right)}{\Gamma(m_{L-1})} \left(1 - \frac{\Gamma_l\left(m_j, \frac{m_j \gamma_T}{\bar{\gamma}_j}\right)}{\Gamma(m_j)}\right)}{\frac{\Gamma_l\left(m_j, \frac{m_j \gamma_T}{\bar{\gamma}_j}\right)}{\Gamma(m_j)} \left(1 - \frac{\Gamma_l\left(m_{L-1}, \frac{m_{L-1}\gamma_T}{\bar{\gamma}_{L-1}}\right)}{\Gamma(m_{L-1})}\right)} \right]^{-1} \frac{\frac{\Gamma_l\left(m_{L-1}, \frac{m_{L-1}\gamma_T}{\bar{\gamma}_{L-1}}\right)}{\Gamma(m_{L-1})} \left(1 - \frac{\Gamma_l\left(m_i, \frac{m_i \gamma_T}{\bar{\gamma}_i}\right)}{\Gamma(m_i)}\right)}{\frac{\Gamma_l\left(m_i, \frac{m_i \gamma_T}{\bar{\gamma}_i}\right)}{\Gamma(m_i)} \left(1 - \frac{\Gamma_l\left(m_{L-1}, \frac{m_{L-1}\gamma_T}{\bar{\gamma}_{L-1}}\right)}{\Gamma(m_{L-1})}\right)} \tag{5.15}$$

and $n_n = [(i - j + k)]_L$.

$$f_{\mathrm{SECps}}\left(\gamma\right) = \begin{cases} \sum_{i=1}^{L} \left[\prod_{j=1, j\neq i}^{L} \frac{\Gamma_l\left(m_j, \frac{m_j \gamma}{m_j}\right)}{\gamma\left(m_j\right)} \right] \frac{{m_i}^{m_i} \gamma^{m_i - 1}}{\Gamma\left(m_i\right) \bar{\gamma}_i^{m_i}} \exp\left(-\frac{m_i \gamma}{\bar{\gamma}_i}\right), & \gamma < \gamma_T \\ \sum_{i=1}^{L} \left[\prod_{j=1}^{i-1} \frac{\Gamma_l\left(m_j, \frac{m_j \gamma_T}{m_j}\right)}{\Gamma\left(m_j\right)} \right] \frac{{m_i}^{m_i} \gamma^{m_i - 1}}{\Gamma\left(m_i\right) \bar{\gamma}_i^{m_i}} \exp\left(-\frac{m_i \gamma}{\bar{\gamma}_i}\right), & \gamma \geq \gamma_T. \end{cases} \tag{5.16}$$

5.2.2 Measurement Setup and Experiments

The wearable device used in this study was a purposely developed wireless sensor node with dimensions of 45 mm × 60 mm × 1.6 mm as shown in Figure 5.5. The unit consisted of a CC1110F32 RF transceiver manufactured by Texas In-

struments (TI) which was configured to operate at 868 MHz using a printed meander-line PCB monopole antenna. During the measurements, the unit was configured to transmit a 9 byte data packet at a data rate of 500 Kbps using minimum-shift keying. All data transmissions occurred at a regular interval of 20 ms with an output power level of 0 dBm.

The test subject (an adult male of height 1.70 m and mass 75 kg) wore a sports T-shirt (86% polyester / 14% elastane) with a special holding pocket purposely sown on to the garment at the front-central-chest region as shown in Figure 5.5. The wireless sensor node was carefully positioned in the pocket such that the printed antenna was in a plane parallel to the surface of the test subject's body. It is worth highlighting that the battery which was used to power the wireless sensor node ensured that there was at least a 6 mm separation between the body and the RF circuitry.

The hypothetical base station array consisted of 10 identical, equidistant base stations which were positioned in a rectangular configuration with a length of approximately 20 m and a width of 6.6 m as shown in Figure 5.6. The purposely developed base station units also consisted of a CC1110F32 RF transceiver configured to record the received signal strength of each received packet. The antenna used by the base station units was a +3.0 dBi omnidirectional monopole antenna with a 10 dB bandwidth of 61 MHz (833-894 MHz), positioned at a height of 1 m from the ground level using a non-conductive support.

As shown in Figure 5.7, all of the experiments were carried out in an outdoor playing field at the Ormeau Park within the city of Belfast in the United Kingdom. They were designed to emulate the channel characteristics which may be present in outdoor wearable applications such as sports and health monitoring, people tracking and positioning, etc. Five individual measurement scenarios, all based around a walking test subject, were considered as shown in Figure 5.6. These scenarios can be broadly categorized into the walk path which the movement followed. They included a rectangular shaped walk path (scenarios 1 and 2), a

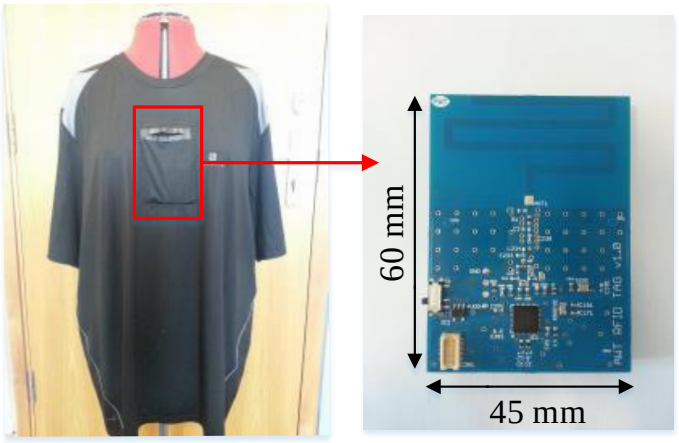

Figure 5.5: Purposely developed garment with mounting pocket at front-central chest and the wearable node used in the measurements.

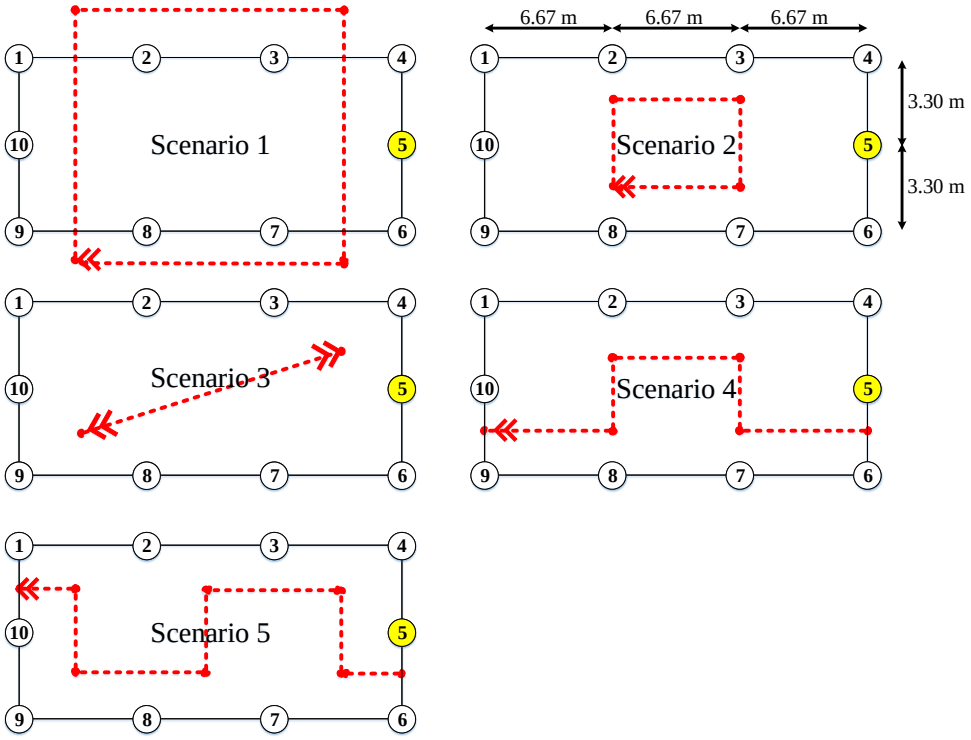

Figure 5.6: Five individual user movement scenarios: a rectangular shape walk path (scenarios 1 and 2); a diagonal-line walk (scenario 3); a meandering walk path (scenarios 4 and 5).

diagonal-line walk path (scenario 3) and a meandering walk path (scenarios 4 and 5). It should be noted that dotted lines in Figure 5.6 and base station 5 represent the test subject's walk path and the target base station, respectively.

Figure 5.7: Satellite view of the measurement environment showing the positions of base stations.

5.2.3 Results

In practice, it is the SNR which is of most interest in the analysis of the performance of wireless systems, although it is difficult to measure SNR. In the study of macro-diversity, the attempt to transform the received signal power into the received SNR was performed. To this end, a number of noise floor measurements were performed prior to the acquisition of the channel data. To improve the robustness of the noise parameter estimates, these measurements were repeated 10 times. The corresponding mean recorded noise threshold was -100.9 dBm while the corresponding lowest received signal power observed in the environment was -94.0 dBm. Following from this, the noise parameters μ_n (mean) and σ_n (standard deviation) were first estimated from noise floor measurements using maximum likelihood estimation (MLE) [101] under the assumption that noise envelope was characterized by a Gaussian distribution [102]. The estimated noise parameters obtained over the 10 repeated trials were then averaged and found to be 0.0021 mV (standard deviation 0.017 uV) and 0.0006 mV (standard deviation 0.009 uV) for the μ_n and σ_n parameters, respectively. The total duration of the 10 repeated noise floor measurements was approximately 10 minutes. From the noise parameter estimates, random variables representing the noise process were then generated. Following from this, the received signal power was then transformed into the received SNR using the definition of SNR (i.e. SNR $= P_{Signal}/P_{Noise}$

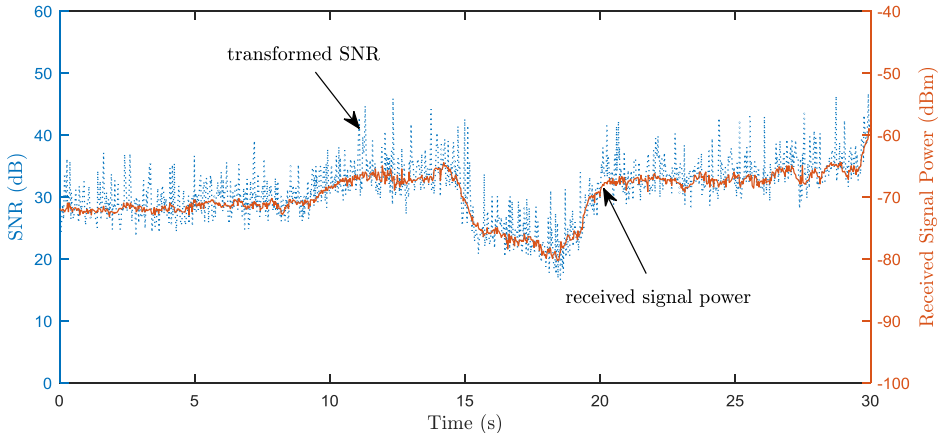

Figure 5.8: Received signal power (continuous lines) at base station 1 for scenario 5 alongside the transformed SNR (dashed lines).

where P_{Signal} and P_{Noise} denote the signal power and noise power, respectively). As an example, Figure 5.8 shows the received signal power at base station 1 for scenario 5 along with its transformed SNR. The average received SNR at each base station for all of the considered scenarios ranged between 22.6 dB and 34.0 dB. Based on these averaged SNR values, three different switching thresholds were determined, namely low (10 dB), medium (30 dB) and high (50 dB) switching thresholds.

5.2.3.1 Base Station Correlation

Since any significant correlation between the signal received at each of the base stations has the potential to degrade the DG, it is important to determine the level of correlation which may exist. For a macro-diversity configuration to be effective, the received signal at each base station should be statistically independent. Figure 5.9 shows the CDFs of the cross-correlation coefficients calculated for all of the considered scenarios. It is clear from the Figure 5.9 that the majority of the estimated cross-correlation coefficients were between -0.7 and 0.7. This result suggests that a switched combining based macro-diversity system equipped with multiple base stations can provide a worthwhile improvement in the received signal reliability.

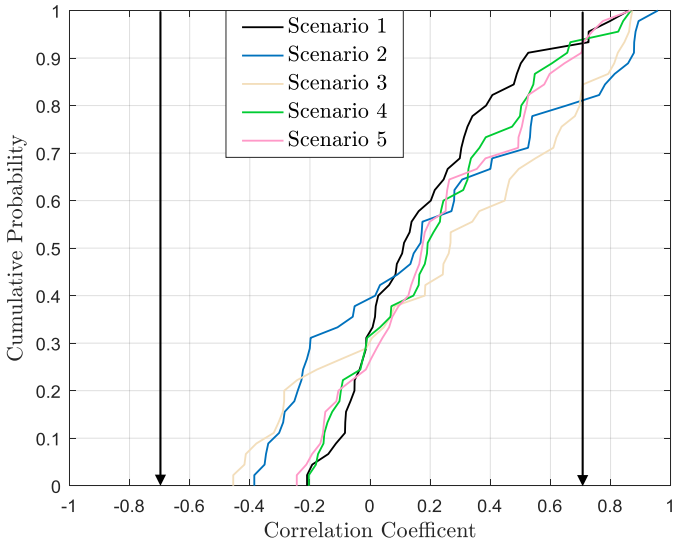

Figure 5.9: CDFs of the calculated cross-correlation coefficients for all of the considered scenarios.

5.2.3.2 Diversity Gain

To evaluate the potential improvement in the received signal reliability that could be obtained using a switched combining based macro-diversity system with SSC, SEC and SECps schemes, the concept of macro-diversity gain was utilised. This is defined as the signal reliability improvement between the SNR of the diversity combiner and that of the target base station for a given probability or signal reliability. It should be noted that base station 5 was considered as the target base station and all macro-diversity gain[1] calculations were made at a signal reliability of 90%. In this analysis, both dual- and four-base station configurations along with two different groupings of base stations have been considered. These were: *group* 1 a dual-base station configuration consisting of base stations 1 and 6; *group* 2 another dual-base station configuration consisting of base stations 5 and 10; *group* 3 a four-base station configuration consisting of base stations 1, 4, 6 and 9; *group* 4 another four-base station configuration consisting of base stations 3, 5, 8 and 10.

Tables 5.4 and 5.5 show the DG statistics for dual-base station SSC, SEC

[1]Herein, for brevity, macro-diversity gain is simply referred as DG.

Table 5.4: DGs for dual-base station SSC, SEC, SECps and PSC systems with three different switching thresholds for all measurement scenarios and groupings.

Scenarios	Switching Threshold (dB)	Macro-Diversity Gain (dB)							
		Group 1 (1, 6)				*Group* 2 (5, 10)			
		SSC	SEC	SECps	PSC	SSC	SEC	SECps	PSC
S1	10	7.7	7.7	7.7	10.6	1.5	1.5	1.5	6.2
	30	2.8	2.8	10.6		−0.9	−0.9	6.2	
	50	−0.4	−0.4	10.6		−2.2	−2.2	6.2	
S2	10	−2.5	−2.5	−2.5	6.4	0.0	0.0	0.0	5.1
	30	6.4	6.4	6.4		3.8	3.8	5.1	
	50	−8.4	−8.4	6.4		−8.5	−8.5	5.1	
S3	10	6.2	6.2	6.2	12.8	1.9	1.9	1.9	11.4
	30	9.8	9.8	12.8		3.2	3.2	11.4	
	50	3.5	3.5	12.8		0.4	0.4	11.4	
S4	10	8.0	8.0	8.0	16.5	9.6	9.6	9.6	15.3
	30	11.1	11.1	16.5		12.2	12.2	15.3	
	50	5.7	5.7	16.5		4.1	4.1	15.3	
S5	10	7.8	7.8	7.8	16.6	6.8	6.8	6.8	15.0
	30	13.9	13.9	16.6		9.0	9.0	15.0	
	50	5.5	5.5	16.6		3.7	3.7	15.0	

and SECps systems with *groups* 1 and 2 (Table 5.4), four-base station SEC and SECps configurations with *groups* 3 and 4 (Table 5.5). For comparison, the DGs for dual- and four-base station PSC are also shown in Tables 5.4 and 5.5. Considering a medium switching threshold, the benefit of having more than two available base stations is demonstrated by comparing the DGs between dual- and four-base station configurations. For example, four-base station SEC with *group* 3 for scenario 1 provided a DG of 13.7 dB whereas dual-base station SEC with *group* 1 achieved a DG of 2.8 dB. Moreover, for all of the groupings and scenarios, dual-base station SEC provided the same performance as dual-base station SSC.

Tables 5.4 and 5.5 also shows that the estimated DG not only varied according to the different scenarios but also with different groupings. This observation can be attributed to the fact that each base station experienced different shadowing

Table 5.5: DGs for four-base station SEC, SECps and PSC configurations with three different switching thresholds for all measurement scenarios and groupings.

Scenarios	Switching Threshold (dB)	Macro-Diversity Gain (dB)					
		Group 3 (1, 4, 6, 9)			*Group* 4 (3, 5, 8, 10)		
		SEC	SECps	PSC	SEC	SECps	PSC
S1	10	−0.5	−0.5	13.7	1.0	1.0	13.2
	30	13.7	13.7		12.3	13.2	
	50	0.2	13.7		−1.0	13.2	
S2	10	−2.5	−2.5	6.9	−3.6	−3.6	7.8
	30	6.8	6.9		7.6	7.6	
	50	−8.2	6.9		−6.5	7.8	
S3	10	1.1	1.1	14.9	1.8	1.8	15.0
	30	14.6	14.7		14.9	14.9	
	50	−2.0	14.9		0.2	15.0	
S4	10	12.2	12.2	18.9	9.3	9.3	19.5
	30	18.8	18.9		19.2	19.2	
	50	4.2	18.9		5.0	19.5	
S5	10	8.0	8.0	18.4	5.2	5.2	18.3
	30	18.2	18.3		18.2	18.2	
	50	4.0	18.4		5.1	18.3	

intensities depending on the position and orientation of the test subject's body during each movement scenario. When comparing the DGs obtained across all scenarios, the values obtained for scenario 4 were the highest. One possible explanation for this is that the average SNR at the target base station (i.e. base station 5) for scenario 4 was smaller than those for the other scenarios. This occurred due to the direct signal path between the body worn node and the target base station existing only for a relatively short length of time compared to those for other scenarios due to the test subject's movement.

To visually investigate the improvement in the received signal reliability using switched diversity schemes, Figure 5.10 shows the received SNR time series at base stations 1, 4, 6 and 9 (*group* 3) along with the output SNR of four-base station SEC and SECps with a medium switching threshold (30 dB) for scenario 2. When the currently selected base station suffered from deep fading due to the

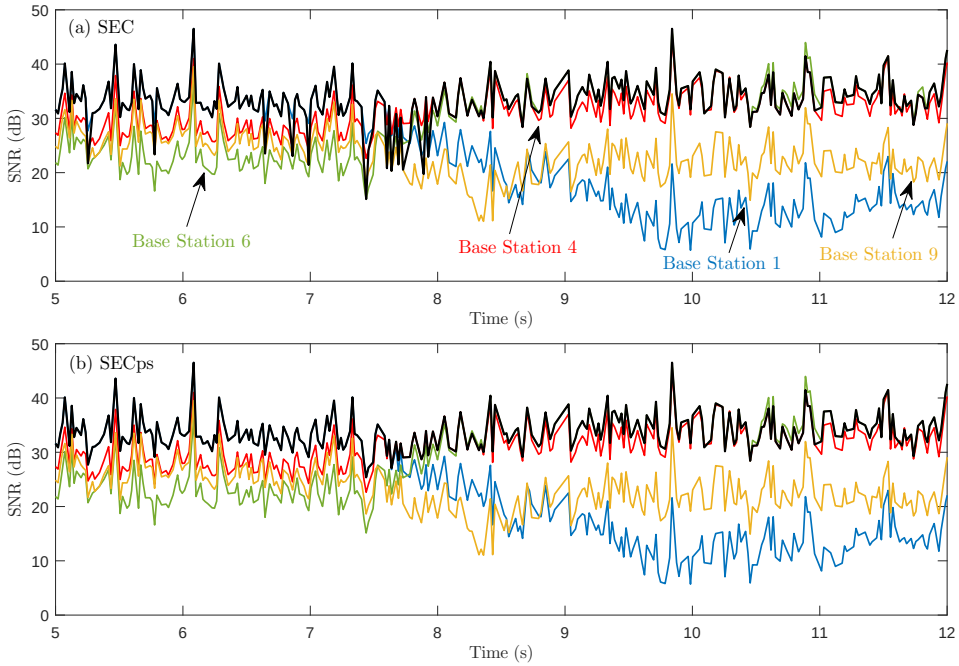

Figure 5.10: Received SNR at base stations 1 (blue), 4 (red), 6 (green) and 9 (yellow) along with the output SNR (black) of four-base station switched diversity schemes for scenario 2: (a) SEC and (b) SECps.

shadowing caused by the test subject's body, switched combining based macro-diversity systems selected and switched to another base station. Consequently, for both the SEC and SECps schemes, the majority of SNR values below the 30 dB level (the predetermined switching threshold) were eliminated. This suggests that a macro-diversity system using either an SEC or SECps scheme made up of base stations 1, 4, 6 and 9 can mitigate shadowing effect of the person's body and achieve a significant improvement in signal reliability.

For a dual-base station configuration operating with a medium switching threshold, *group* 1 always provided a greater DG than *group* 2 with the exception of scenario 4. This suggests that the location of the base stations in *group* 1 was more appropriate compared to *group* 2 in general. However, for a four-base station configuration, *groups* 3 and 4 provided similar DGs for all of the movement scenarios. As well as this, for the majority of the movements considered in this study, adding the two additional base stations also offered no significant difference in the DGs provided by the SEC and SECps schemes when a medium

switching threshold was selected. For example, as shown in Table 5.4, the DGs for dual-base station SEC and SECps with *group* 1 for scenario 1 were 2.8 dB and 10.6 dB, respectively. On the other hand, as shown in Table 5.5, for four-base station SEC and SECps with *group* 3, both had the same DG which was 13.7 dB. These observations suggest that a switched diversity system with more than two base stations is less affected by the location of the base stations and thus provides a more stable performance in terms of signal reliability.

Additionally, it was also found that the estimated DGs for both the dual-base station and four-base station configurations strongly depended on the switching threshold. For example, the DGs for four-base station SEC with *group* 3 for scenario 2 were -2.5, 6.8 and -8.2 dB at the low, medium and high switching thresholds, respectively. Interestingly, negative DGs were also observed at the low and high switching thresholds, indicating that there was no benefit to using a switched diversity scheme with these switching thresholds.

To further examine the effect of different switching thresholds on the achievable DG, Figures 5.11 and 5.12 show the DGs for four-base station SEC and SECps respectively with different switching threshold values ranging between 0 dB and 60 dB for all of scenarios. It is obvious that the estimated DGs varied according to the switching threshold, but there always existed an optimum switching threshold which maximizes the DG. With the optimum switching threshold, both four-base station SEC and SECps systems provided almost the same DG as an equivalent PSC system.

While the DG for four-base station SEC decreases beyond the optimum switching threshold, the DG for four-base station SECps became saturated at the maximum achievable DG level. This was most likely due to the different combining methods implemented by SEC and SECps schemes. The SEC scheme selects the last examined base station when no acceptable base station is found after examining all available options. On the other hand, the SECps scheme selects the best path which has the highest SNR among all paths instead of the last

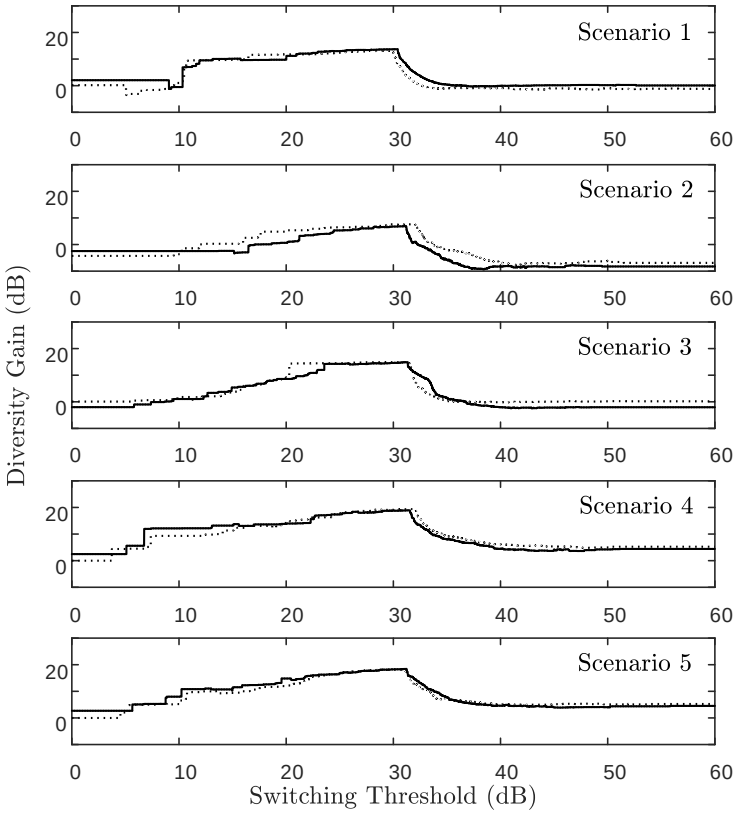

Figure 5.11: Effect of different switching thresholds on achievable DG of four-base station SEC with *group* 3 (continuous lines) and *group* 4 (dashed lines) for all of movement scenarios.

examined base station. The SECps scheme therefore acts as a PSC scheme when the switching threshold is high and no acceptable path is found after examining all diversity paths.

5.2.3.3 Number of Path Examinations and Switches

To evaluate the trade-off between performance and complexity (which is related to energy consumption), the number of path examinations and number of path switches between base stations for SEC and SECps schemes were evaluated. As shown in Figures 5.13 and 5.14, the number of path examinations and switches for the SEC and SECps schemes were almost the same when the switching threshold was low while the SECps scheme had a greater number of path examinations and switches compared to the SEC scheme at the middle and high switching threshold levels. Again, this was most likely due to the fact that when there

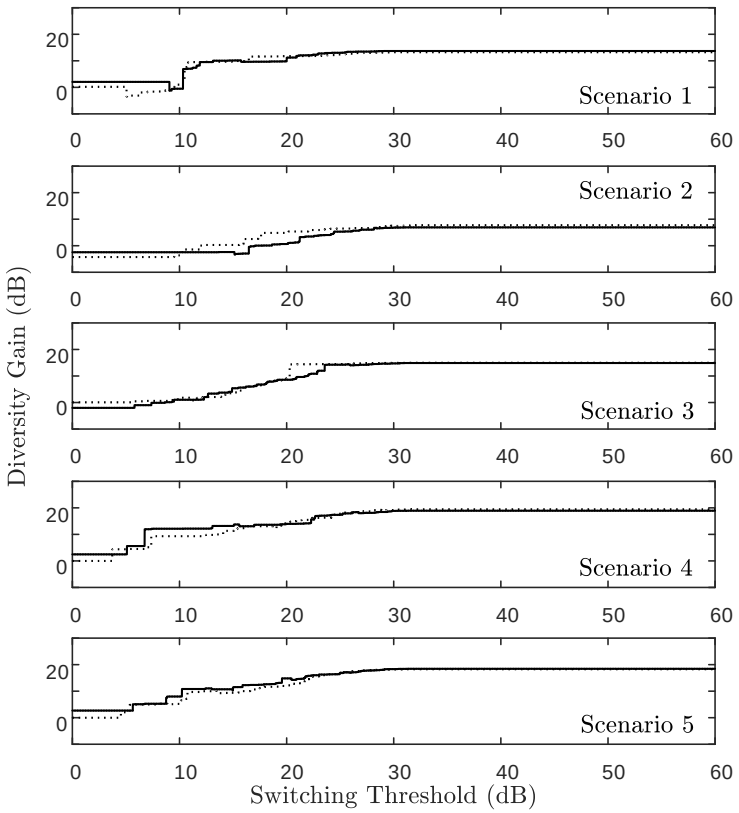

Figure 5.12: Effect of different switching thresholds on achievable DG of four-base station SECps with *group* 3 (continuous lines) and *group* 4 (dashed lines) for all of movement scenarios.

is no acceptable base station available the SEC scheme usually selects the last examined base station while the SECps scheme selects the best performing base station. Consequently, for an L-base station arrangement, the SEC scheme has at most $L-1$ path switches whereas the SECps scheme has at most L path switches, i.e. the number of path switches for the SECps scheme is usually greater than that for the SEC scheme. They are the same only if the last examined base station has the highest SNR.

Likewise, for an L-base station arrangement, when the RX switches from the $(L-1)^{th}$ base station to the L^{th} base station (i.e. last base station), the SECps scheme still needs to monitor the received SNR at the L^{th} base station whereas the SEC scheme does not need to do this because it switches to the L^{th} base station anyway irrespective of whether the received SNR at the L^{th} base station is above the switching threshold or not. Based on the DG, number of path examinations

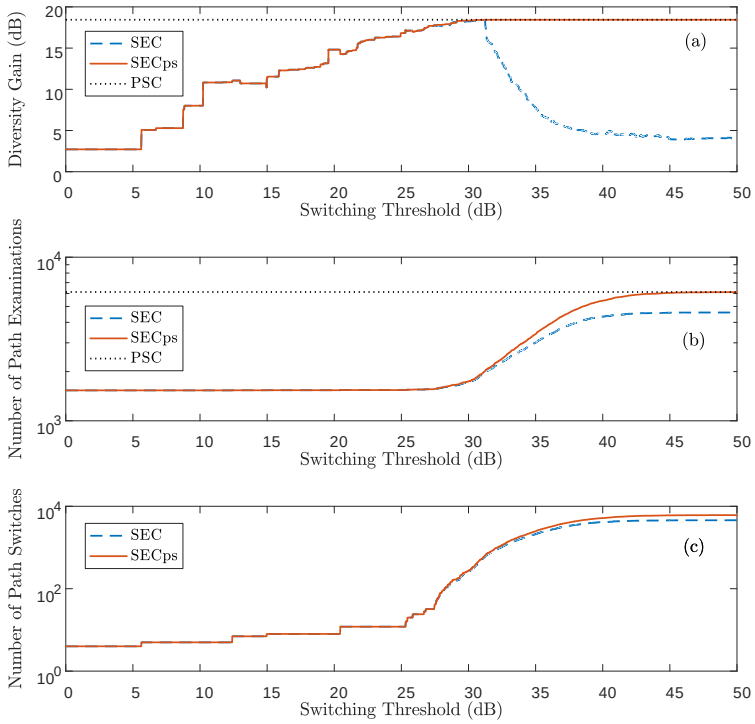

Figure 5.13: DG, the number of path examinations and number of path switches for scenario 5 using the *group* 3 configuration with four-base station SEC and SECps schemes for different switching thresholds. For comparison, four-base station PSC using the *group* 3 is also presented.

and number of path switches, it was observed that the SECps scheme provided a greater DG, but the additional number of path examinations and switches will lead to more energy consumption compared to the SEC scheme.

When compared with a PSC scheme, as shown in Figures 5.13(a) and (b), the SECps scheme had a smaller number of path examinations at medium switching threshold levels, but it had a similar DG. This was due to the fact that the PSC scheme monitors the SNR of all of the base stations simultaneously and then selects the base station with the highest SNR. Therefore, at medium switching threshold levels, the SECps scheme prevents the unnecessary monitoring while providing a similar performance compared to the PSC scheme, suggesting that the SECps scheme is less complex and thus more energy efficient compared to the PSC scheme. However, as expected, it was observed that the number of path examinations for the SECps and PSC schemes became similar at high switching threshold levels.

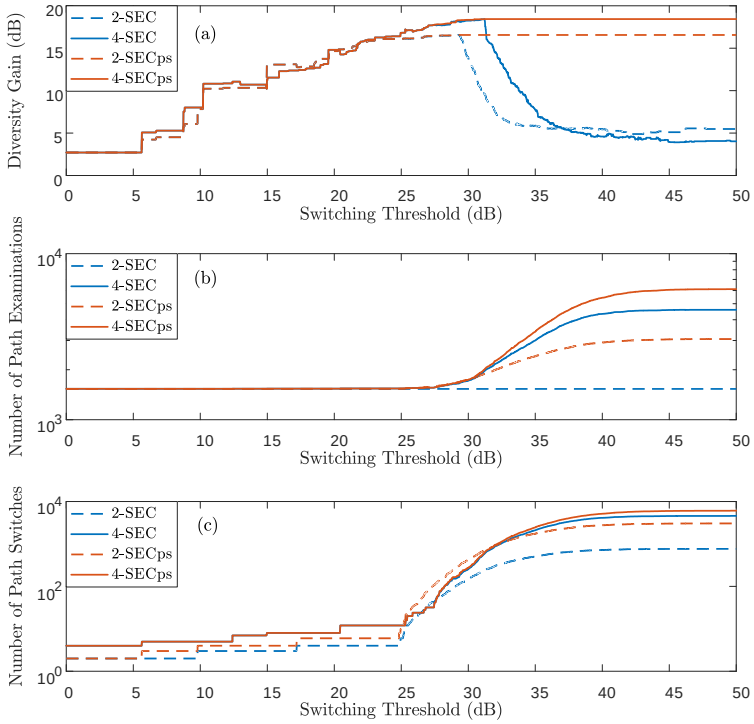

Figure 5.14: DG, the number of path examinations and number of path switches for scenario 5 using the *group* 3 configuration with four-base station SEC and SECps schemes for different switching thresholds. For comparison, dual-base station SEC and SECps using the *group* 1 configuration are also presented.

Figures 5.14(a)-(c) show a comparison of the DG, number of path examinations and number of path switches between base stations for dual- and four-base station SEC and SECps. While it is obvious that four-base station configurations provided a greater DG (higher performance) than dual-base station configurations, they also had a significantly greater number of path examinations and switches (higher complexity and higher energy consumption). Therefore the choice as to which configuration and scheme to implement for wearable systems will come down to a choice between performance and complexity. For some, but not all cases (see Figures 5.13, 5.14 and Tables 5.4 and 5.5), a dual-base station configuration with the appropriate switching threshold/technology may offer a good compromise between complexity (energy consumption) and information recovering capability.

5.2.3.4 Fading Statistics at the Output of the Switched Combiners

To characterize the fading behaviour at the output of the hypothetical switched combiners, the diversity specific analytical equations for L-base station SSC, SEC and SECps systems operating in i.n.i.d. Nakagami-m shadowing channels were fitted to the empirical data. The Nakagami m and $\bar{\gamma}$ parameters were estimated using a non-linear least squares routine written in MATLAB to fit (5.12), (5.14) and (5.16) to the measurement data. Again, dual- and four-base station configurations with the same groupings presented in Chapter 5.2.3 were considered. It should be noted that the minimum data set size used for the parameter estimation was 761 samples.

As an example of the results of the model fitting process, Figure 5.15 shows the PDFs of four-base station SEC and SECps (*group* 3) with three different switching thresholds for scenario 5. The RAD was evaluated to provide a quantitative measure of the goodness-of-fit of the theoretical PDFs with the measured data. As the RAD tends towards zero, the test PDF (i.e. theoretical PDF) is in very good agreement with the true PDF (i.e. empirical PDF). The corresponding RAD analysis results are presented in Table 5.6. For the majority of cases, the estimated RAD values were less than 0.1, suggesting that the theoretical models for four-base stations SEC and SECps provided an adequate fit to the measured data.

Tables 5.7 and 5.8 provide the parameter estimates for four-base station SEC and SECps (*group* 3) respectively with three different switching thresholds for all of the considered movement scenarios. As shown in Tables 5.7 and 5.8, the parameter estimates obtained for the fading experienced at each of the considered base stations were different, suggesting that each base station experienced non-identical shadowing. Additionally, as expected, the parameter estimates also varied according to the user's movement. For example, when comparing scenarios 4 and 5 for four-base station SECps with a medium switching threshold (30 dB), the estimated m parameters for scenario 4 were higher than those for

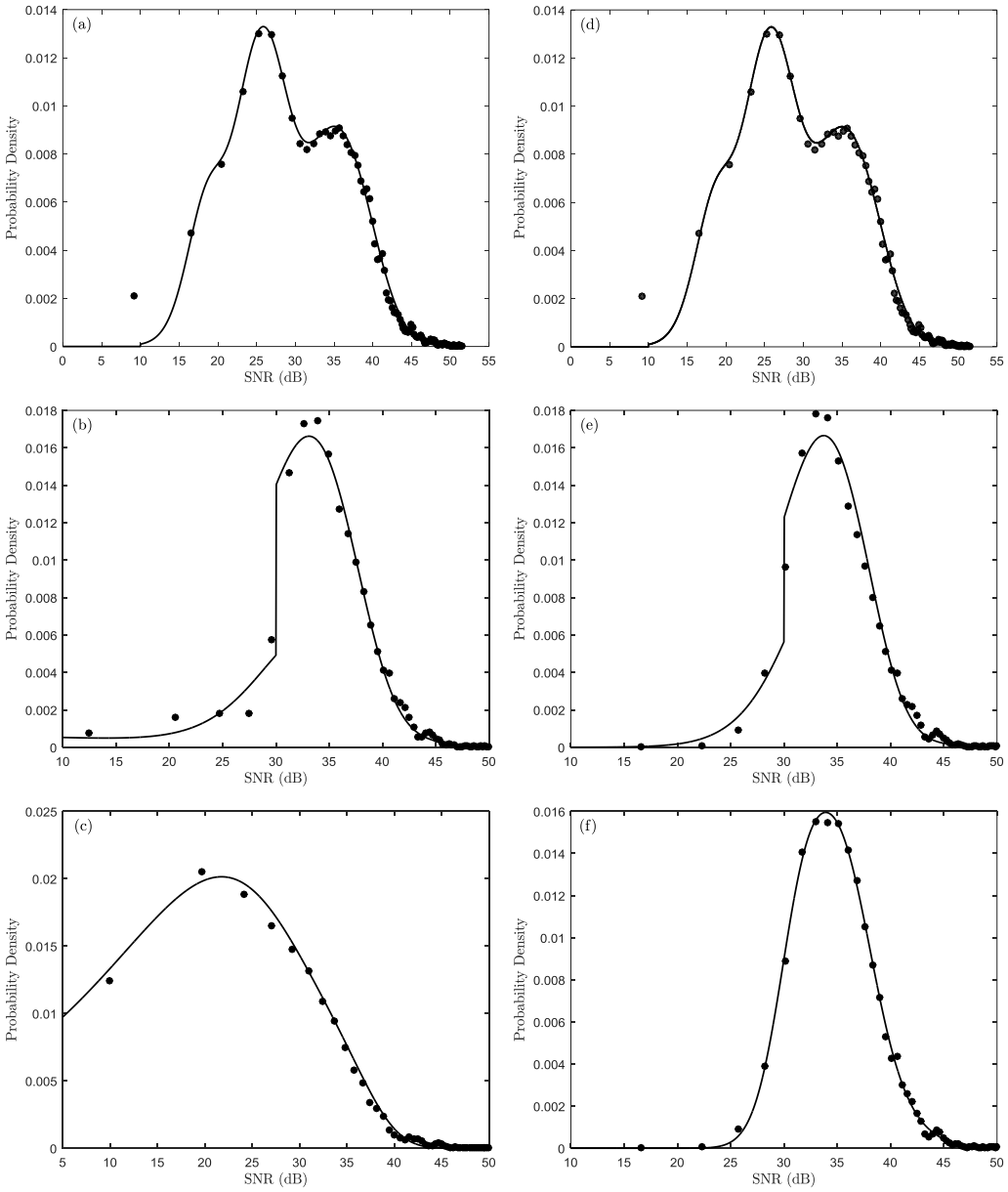

Figure 5.15: Empirical (circles) and theoretical (continuous lines) PDFs for scenario 5 with *group* 3 for four-base station SEC with (a) low, (b) medium and (c) high switching thresholds and four-base station SECps with (d) low, (e) medium and (f) high switching thresholds.

scenario 5. This suggests that the fading observed at the four base stations during scenario 4 suffered less from shadowing compared to scenario 5. This observation is supported by the fact that the average SNR for the output of four-base station SECps for scenario 4 (36.4 dB) was greater than that for scenario 5 (35.8 dB).

As shown in Figure 5.15, the shapes of the PDFs were different according to the switching threshold that was adopted. When a low switching threshold was chosen (i.e. 10 dB) the PDFs of both SEC and SECps were the same as

Table 5.6: Estimated resistor-average distance for all of the considered cases.

Switching Threshold	Scenarios	Dual-Base Station				Four-Base Station			
		Group 1		*Group* 2		*Group* 3		*Group* 4	
		SEC	SECps	SEC	SECps	SEC	SECps	SEC	SECps
Low (10 dB)	S1	0.0267	0.0224	0.0213	0.0213	0.0070	0.0206	0.0139	0.0135
	S2	0.0194	0.0441	0.0201	0.0120	0.0106	0.0252	0.0192	0.0238
	S3	0.0150	0.0162	0.0467	0.0309	0.0153	0.0297	0.0085	0.0172
	S4	0.0172	0.0239	0.0137	0.0175	0.0070	0.0316	0.0107	0.0096
	S5	0.0246	0.0232	0.0208	0.0162	0.0048	0.0107	0.0098	0.0182
Medium (30 dB)	S1	0.0091	0.0061	0.0211	0.0067	0.0206	0.0107	0.0254	0.0238
	S2	0.0385	0.0115	0.0280	0.0120	0.0779	0.0111	0.0529	0.0178
	S3	0.0465	0.0067	0.0279	0.0081	0.0159	0.0064	0.0168	0.0129
	S4	0.0233	0.0600	0.0193	0.0083	0.0190	0.0258	0.0337	0.0137
	S5	0.0540	0.0089	0.0104	0.0258	0.0356	0.0120	0.0388	0.0124
High (50 dB)	S1	0.0159	0.0049	0.0359	0.0067	0.0190	0.0151	0.5051	0.0262
	S2	0.0195	0.0130	0.0120	0.0099	0.0090	0.0109	0.0226	0.0135
	S3	0.0150	0.0110	0.0074	0.0039	0.0119	0.0061	0.0197	0.0062
	S4	0.0887	0.0557	0.0273	0.0072	0.0614	0.0122	0.0155	0.0158
	S5	0.0104	0.0061	0.0241	0.0081	0.0222	0.0108	0.0221	0.0099

shown in Figures 5.15(a) and (d). This was most likely due to the fact that path switching between base stations rarely occurred at low switching threshold levels. More specifically, as shown in Figure 5.16(a), there was only one instance of path switching between base stations (base station $6 \rightarrow 9$) with the hypothetical switched combiner selecting base station 9 for the remainder of the time. As evidence for this, Figure 5.16(b) shows that the PDF of the output SNR of four-base station SEC and the PDF of the received SNR at base station 9. It is clear that these two PDFs were similar. It is worth remarking that the PDF of the received SNR at base station 9 in Figure 5.16(b) was generated using the received SNR beyond the vertical line in Figure 5.16(a) which represents path switching from base station 6 to 9.

On the contrary, path switching between base stations occurs during almost every single time slot when the switching threshold is high (50 dB). This is particularly evident from Figure 5.17, where the SEC scheme switched from the

Table 5.7: Parameter estimates for four-base station SEC with three different switching thresholds for all of the considered movement scenarios in *group* 3 (base stations 1, 4, 6, and 9).

Scenarios	m_1	$\bar{\gamma_1}$	m_2	$\bar{\gamma_2}$	m_3	$\bar{\gamma_3}$	m_4	$\bar{\gamma_4}$
Low Switching Threshold (10 dB)								
S1	2.9	52.7	6.4	13.3	15.0	6.8	1.6	2.9
S2	9.0	14.6	4.1	59.4	15.0	7.1	15.0	9.0
S3	2.1	100.0	4.2	39.3	9.3	11.6	15.0	2.1
S4	8.0	14.3	3.8	64.2	15.0	7.1	15.0	7.5
S5	4.2	73.6	3.1	100.0	7.5	21.1	15.0	8.7
Medium Switching Threshold (30 dB)								
S1	3.9	58.3	0.5	0.1	10.0	1.5	0.8	62.9
S2	2.5	100.0	15.0	44.5	8.2	64.2	15.0	44.5
S3	15.0	1.8	11.7	1.1	0.6	80.6	6.1	58.1
S4	9.8	64.7	0.9	100.0	3.5	100.0	15.0	46.6
S5	0.8	62.8	4.7	58.9	15.0	1.0	9.1	4.8
High Switching Threshold (50 dB)								
S1	14.0	59.7	1.8	22.9	13.5	41.5	11.6	74.5
S2	1.7	25.1	8.1	32.9	12.9	83.1	5.0	51.3
S3	7.3	20.7	1.5	18.9	13.7	28.6	5.9	51.7
S4	8.1	49.1	13.7	35.4	5.5	58.5	1.7	26.2
S5	4.6	25.0	7.3	22.9	6.1	64.2	1.7	29.4

currently selected base station to another base station even if the presently selected base station had the highest SNR, causing a degradation in the overall performance. As a result of this, there was a significant increase in the spread of the output SNR as shown in Figure 5.15(c). It is worth remarking that the SECps scheme does not follow this regime when the switching threshold is high, as it favours the base station with the highest SNR when no acceptable signal base station is above the switching threshold (Figure 5.17). In this scenario, the SECps scheme effectively operates as a PSC scheme. Therefore, unlike the SEC scheme, the majority of the SECps output SNR levels were in the reduced range from 25 dB to 45 dB, which resulted in an empirical probability density with a significantly reduced spread as shown in Figure 5.15(f).

For both the SEC and SECps schemes, when the switching threshold was

Table 5.8: Parameter estimates for four-base station SECps with three different switching thresholds for all of the considered movement scenarios in *group* 3 (base stations 1, 4, 6, and 9).

Scenarios	m_1	$\bar{\gamma_1}$	m_2	$\bar{\gamma_2}$	m_3	$\bar{\gamma_3}$	m_4	$\bar{\gamma_4}$
Low Switching Threshold (10 dB)								
S1	0.9	46.7	12.8	11.2	15.0	54.6	4.4	3.8
S2	1.5	53.5	15.0	13.2	12.0	13.2	14.1	7.9
S3	1.3	34.0	15.0	2.0	2.1	6.3	15.0	2.3
S4	1.8	68.1	15.0	18.8	9.3	16.9	14.1	88.1
S5	1.6	61.4	15.0	10.8	15.0	62.9	7.6	15.4
Medium Switching Threshold (30 dB)								
S1	4.2	61.2	0.5	48.9	15.0	7.1	15.0	7.1
S2	13.4	0.4	0.7	38.0	9.0	53.3	9.6	0.1
S3	0.5	30.5	7.6	59.7	15.0	19.6	15.0	19.6
S4	0.5	45.8	15.0	10.9	9.7	62.6	15.0	14.3
S5	5.1	60.9	0.5	100.0	2.9	0.4	8.9	0.2
High Switching Threshold (50 dB)								
S1	5.8	33.4	15.0	9.4	3.3	55.6	0.5	31.2
S2	7.6	26.9	5.1	51.0	15.0	34.1	0.5	30.4
S3	6.2	19.9	15.0	29.8	6.7	56.6	0.5	30.6
S4	6.8	58.7	14.9	32.5	0.5	21.0	0.5	41.7
S5	5.2	52.7	12.0	28.0	15.0	11.8	1.4	50.6

set at a medium value (30 dB), the majority of combiner output SNR levels ranged between 25 dB and 45 dB as shown in Figures 5.15(b) and (e). These were almost identical to those obtained for the SECps scheme configured with a high switching threshold, i.e. a PSC scheme, although occasionally the SEC scheme still had instances where the combiner output SNR was below 15 dB. When compared in terms of the number of path examinations and achievable DG, the SECps scheme operating with a medium switching threshold provided a more favourable alternative because it achieved sufficient performance with a lesser number of path examinations compared to the PSC scheme.

Further evidence of the benefits of having more than two base stations can also be realised by analysing the fading statistics at the output of the switched diversity combiner. For example, Figure 5.18 shows the PDFs of dual-base station

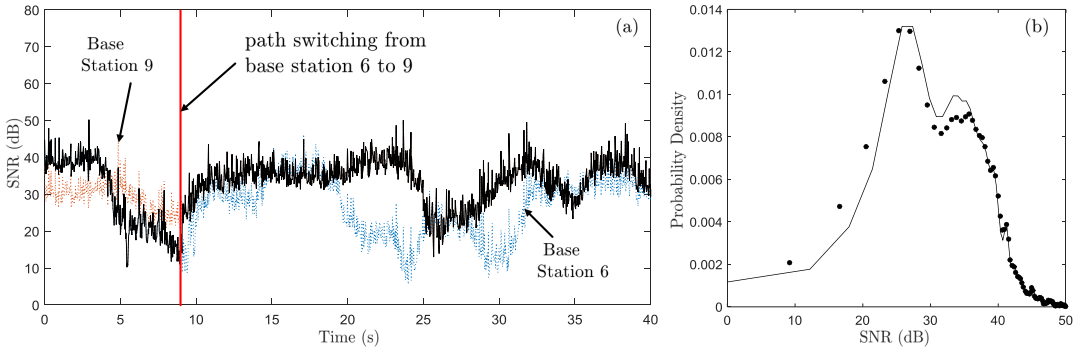

Figure 5.16: (a) Received SNR at base stations 6 and 9 along with the output SNR of four-base station SEC (continuous lines); (b) PDFs of the output SNR (circle symbols) of four-base station SEC and the received SNR (continuous lines) at base station 9. It should be noted that the received SNR at base stations 1 and 4 in *group* 3 are not shown in Figure 5.16(a) for clarity.

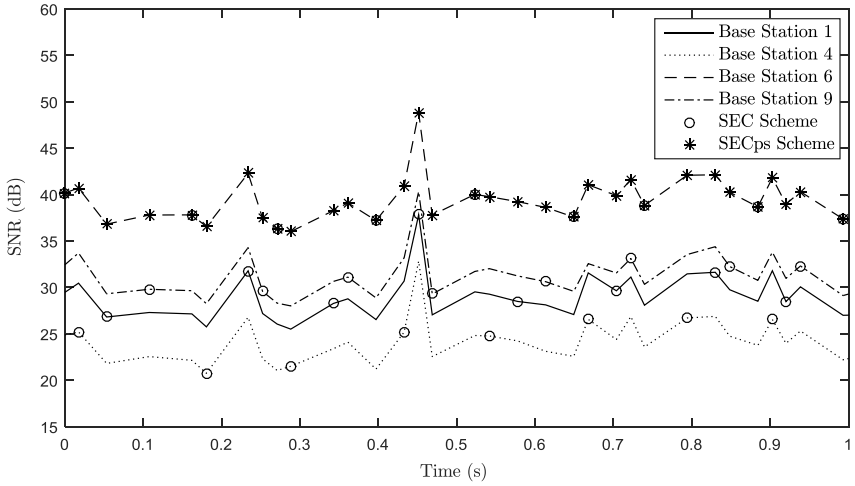

Figure 5.17: Excerpt of the SNR time series obtained for scenario 5 comparing four-base station SEC and SECps with the received SNR at base stations 1, 4, 6 and 9.

SEC and SECps with *group* 2 and four-base station SEC and SECps with *group* 4 for scenario 2 when a medium switching threshold was adopted. It is obvious that for both the SEC and SECps schemes, the four-base station configurations had a lower number of signal observations at low SNR levels and a higher number of signal observations at high SNR levels than the dual-base station configurations. More specifically, as shown in Figure 5.18(a), the dual-base station configuration had some output SNR levels which were less than 15 dB whereas the four-base station configuration had no output SNR less than 15 dB. This result indicates that an additional improvement in the signal quality can be achieved by implementing a four-base station macro-diversity configuration, in which case all SNR

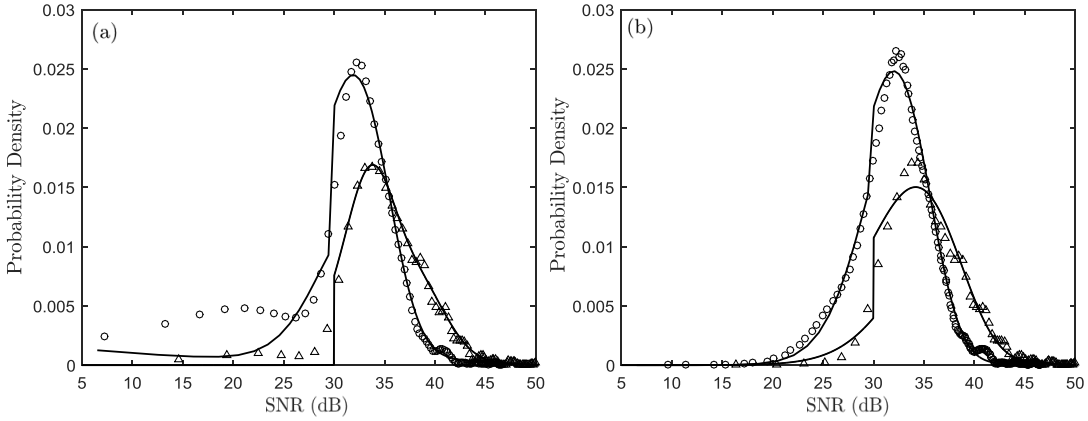

Figure 5.18: Empirical (symbols) and theoretical (continuous lines) PDFs for scenario 2 for dual-base station with *group* 2 (circle symbols) and four-base station with *group* 4 (triangle symbols) for both (a) SEC and (b) SECps schemes with a medium switching threshold.

drops below 15 dB level will be eradicated. Again, it was shown that the theoretical PDFs provided an adequate fit to empirical PDFs with the exception of the dual- and four-base station SEC schemes at SNR levels below the switching threshold. Table 5.9 provides a sample of the parameter estimates obtained for both dual- and four-base station SEC and SECps with a medium switching threshold for scenario 2 to allow the reproduction of the theoretical probability densities presented in Figure 5.18.

5.3 Conclusion

The potential improvement in the received signal for indoor wearable communications at 5.8 GHz using micro-diversity configurations based on dual-branch SSC, dual- and four- branch SEC, dual- and four-branch SECps has been evaluated in terms of their DGs. Among these switched diversity schemes, the SECps scheme provided a better performance than both SSC and SEC schemes. It has been observed that up to 7.9 dB DG can be achieved when using four-branch SECps. The impact of different switching thresholds has also been investigated and the importance of selecting the optimum switching threshold has been emphasized. When a medium switching threshold was adopted, the mean Ω parameter (i.e.

Table 5.9: Parameter estimates for dual-base station SEC and SECps with *group* 2 (base stations 5 and 10) and four-base station SEC and SECps with *group* 4 (base stations 3, 5, 8, and 10) at the medium switching threshold for scenario 2.

	Dual-base Station				Four-base Station							
	m_1	$\bar{\gamma_1}$	m_2	$\bar{\gamma_2}$	m_1	$\bar{\gamma_1}$	m_2	$\bar{\gamma_2}$	m_3	$\bar{\gamma_3}$	m_4	$\bar{\gamma_4}$
SEC	6.99	46.45	0.50	51.68	0.88	100.00	0.88	100.00	6.01	81.90	15.00	49.58
SECps	6.86	47.09	0.50	26.92	4.64	65.64	0.78	100.00	0.50	0.10	10.52	0.10

spread parameter) was observed to decrease, resulting in a reduction of the spread of the output envelope. It has also been shown that for the scenarios considered in this study, an SECps scheme provided almost the same performance as a PSC scheme when the optimum switching threshold was chosen. An analysis of the output envelope of dual-branch SSC, four-branch SEC and SECps operating in i.i.d. Nakagami-m multipath fading channels has been presented and shown to provide a good fit to the measured wearable channel data.

This Chapter has also investigated the potential improvement in signal reliability for outdoor wearable communications channels operating at 868 MHz using macro-diversity arrangements based on dual-base station SSC, SEC and SECps and four-base station SEC and SECps. The benefit of having more than two signal base stations has been demonstrated by comparing the DGs between a range of dual- and four-base station configurations. It was found that for the scenarios considered here, switched diversity systems consisting of four-base station configurations were less affected by the location of the individual base stations and thus provided a more stable performance (in terms of signal reliability). Among the three different switched diversity schemes, the SECps scheme provided the best performance for all scenarios and groupings. The results have shown that this type of switched diversity system can provide up to 19.5 dB DG when using a four-base station arrangement. However, this improvement is not open-ended as it will add extra complexity to the design of the switched diversity system.

The impact of different switching thresholds on the DG, number of path examinations and number of path switches of the various combiner outputs has

been studied to emphasize the importance of selecting an appropriate switching threshold. It was observed that there exists an optimum switching threshold which maximizes the performance for this type of the wearable system. More specifically, at the optimum switching threshold, the switched diversity system can provide considerable performance with much fewer path examinations when compared to the PSC scheme. It was also found that while a four-base station switched diversity system provides higher DG than a dual-base station switched diversity system, this comes at the cost of having a greater number of path examinations and switches. This result indicates that there exists a trade-off between DG (performance) and the number of path examinations and path switches between base stations (complexity and energy consumption).

In direct contrast to this, an inappropriate switching threshold may cause not only the substandard performance of the wearable systems but also greater energy consumption due to the unnecessary path examinations and needless path switches between base stations. In this case, no additional benefit is obtained using a switched combining based macro-diversity system. Consequently, the appropriate switching threshold must be carefully chosen so that the switched combining based macro-diversity system works as desired. In this study, each scenario was found to have a different optimum switching threshold. Nonetheless, among the three switching threshold levels which were considered, the medium switching threshold (30 dB) was found to be quite close to the optimum switching threshold for all of the scenarios.

Finally, a statistical analysis of the switched diversity combiner output has been presented under the assumption of i.n.i.d. Nakagami-m shadowing channels. Over all of the considered measurement scenarios, the PDFs of the switched combiner including SSC, SEC and SECps schemes have been shown to provide an adequate fit to the fading observed at the output of the virtual switched combiner. From the parameter estimates, it was found that each base station experienced non-identical Nakagami-m shadowing. The parameter estimates also suggest that

the shadowing conditions observed at each base station varied according to the user's movement.

Chapter 6

Mitigation of Combined Micro and Macro Fading

The previous Chapter investigated the potential improvement in signal reliability which may be obtained in wearable communications channels using a switched combining based micro-diversity system (to overcome multipath) and a switched combining based macro-diversity setup (to mitigate shadowing). In many scenarios, the received signal in wearable systems may experience multipath and shadowing simultaneously. In this instance, the use of either micro-diversity or macro-diversity in isolation may not be sufficient to overcome the deleterious effects caused by the simultaneous existence of multipath and shadowing. Therefore, in this Chapter, a systematic investigation of the utilisation of both micro- and macro-diversity techniques to mitigate multipath and shadowing in wearable communications channels is undertaken.

6.1 Introduction

Over the last few decades, relatively few studies have been published on the combined micro- and macro-diversity systems operating in fading channels [103–106]. For example, an analytical expression for the outage probability in correlated gamma shadowing channels has been provided when MRC and PSC schemes

are considered at the micro-level and macro-level respectively [103]. Modulation schemes using this type of setup have also been considered [104], Here, the performance of M-ary differential phase shift keying (MDPSK) with EGC based micro-diversity and PSC based macro-diversity techniques was evaluated in terms of its bit error rate (BER) and outage probability.

For convenience, these studies have only considered a PSC scheme at the macro-level due to its low complexity and ease of implementation. As discussed in Chapter 5, an SECps scheme can provide a comparable performance (with less complexity) compared to a PSC scheme when the optimum switching threshold is chosen. As well as this, a study on the utility of a combined micro- and macro-diversity system has not been performed in the context of wearable communications yet. Motivated by these two factors, in this Chapter, the potential improvement in signal reliability for wearable communications channels operating at 5.8 GHz using a combined micro- and macro-diversity system has been investigated. To this end, an MRC scheme is considered at the micro-level (i.e. at each base station) while an SECps scheme is used at the macro-level to switch between the base stations, i.e. a combined MRC-SECps system.

6.2 Measurement System and Experiments

The same wireless node used for the TX in Chapter 3 was also utilised for the TX in this Chapter. The TX was alternated between four different positions of an adult male of height 1.83 m and weight 73 kg using a small strip of Velcro®. These were central-chest, right-head, right-pocket and right-wrist positions. As shown in Figure 6.1, the hypothetical micro- and macro-diversity system considered in this study consisted of four spatially separated base stations where each base station availed of two micro-diversity branches (separated by a distance of 0.28 m). The RX branches featured an identical ML5805 transceiver whose analog received signal strength output was sampled with a 10-bit quantization depth at a rate of 10 kHz using a PIC32MX micro-controller. The same antennas described in

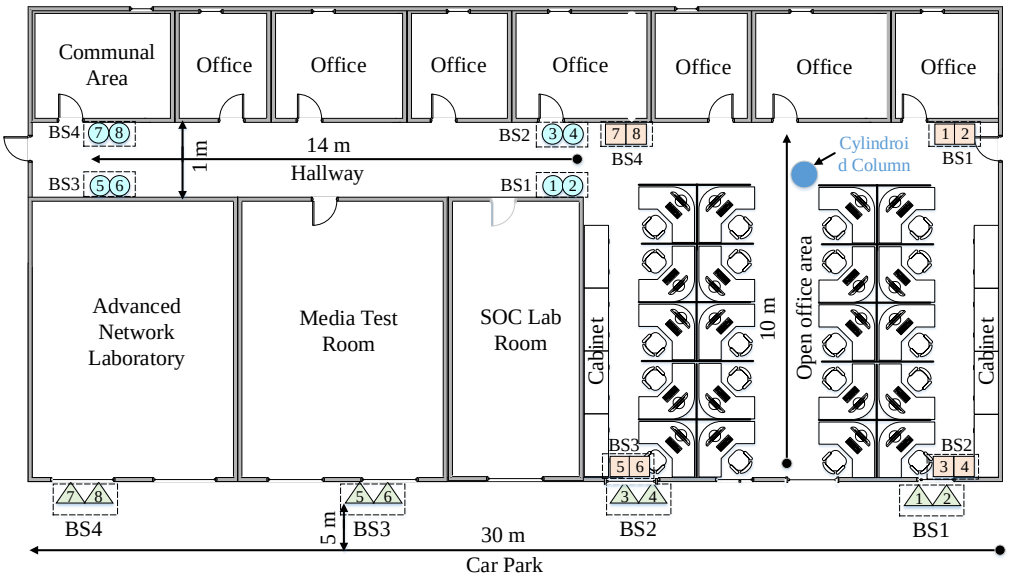

Figure 6.1: Measurement environments showing the positions of the micro- and macro-diversity RXs. It should be noted that the base station consisting of two RX branches is denoted as BS here for brevity.

Chapter 3 were also used for both the TX and RXs.

As shown in Figure 6.1, the measurements were conducted in three different environments, namely an indoor hallway, an open office area and an outdoor car park area. The indoor hallway and open office area are located on the first floor of the ECIT building. The virtual base stations were positioned in a rectangular configuration with a length of 10.0 m and a width of 10.4 m in the open office environment and a length of 14.0 m and a width of 1.0 m in the hallway environment. It is worth highlighting that the RX branches were directly attached to the wall at a height of 2.0 m from the floor level. The outdoor car park is adjacent to the ECIT building as shown in Figure 6.1. The virtual base stations in the outdoor car park environment were aligned along a straight line with an equal spacing of 10 m and positioned on the wall at a height of 5.0 m from the ground level. During the measurements, the test subject walked in a straight line within each environment, covering a total distance of 10 m, 14 m and 30 m for the open office, hallway and car park environments respectively. All of the measurements were repeated three times for each of the body worn node positions and environments.

6.3 Correlation and Power Imbalance

Prior to the diversity analysis, the cross-correlation coefficient and power imbalance were calculated using the approach detailed in Chapter 2.7. Before determining the correlation due to shadowing in the macro-diversity setup, the shadowing was extracted from the received signal by averaging over a distance of 10 wavelengths. Following from this, the correlation due to multipath fading observed in the micro-diversity setup was calculated after removing the estimated shadowing from the raw received signal.

Figures 6.2 shows the CDFs of the cross-correlation coefficients and power imbalances calculated for all of the considered body worn node positions and environments. It is worth highlighting that branch pairs (1, 2), (3, 4), (5, 6) and (7, 8) were considered for the micro-diversity system. For the macro-diversity system, two different four-base station configurations were considered by selecting one RX branch from each of four base stations, which were *group* 1 (1, 3, 5, 7) and *group* 2 (2, 4, 6, 8). Consequently, for the calculation of the cross-correlation coefficient and power imbalance, branch pairs (1, 3), (1, 5), (1, 7), (3, 5), (3, 7) and (5, 8) were considered for *group* 1 while branch pairs (2, 4), (2, 6), (2, 8), (4, 6), (4, 8) and (6, 8) were considered for *group* 2.

As expected, for all of the considered body worn node positions and environments, the power imbalances for the micro-diversity configuration were generally smaller than those for the macro-diversity setup. More specifically, the estimated cross-correlation coefficients ranged from -0.2 to 0.6 for the micro-diversity configuration while they were from -0.8 to 0.9 for the macro-diversity configuration. For the micro-diversity setup, the estimated cross-correlation coefficients for the indoor environments (hallway and open office) were smaller than those for the outdoor environment (car park). This is most likely due to the fact that the indoor environments are likely to have stimulated more multipath, helping to de-correlate the signals received at each of the micro-diversity branches.

Interestingly, negative correlation coefficients were quite often observed for

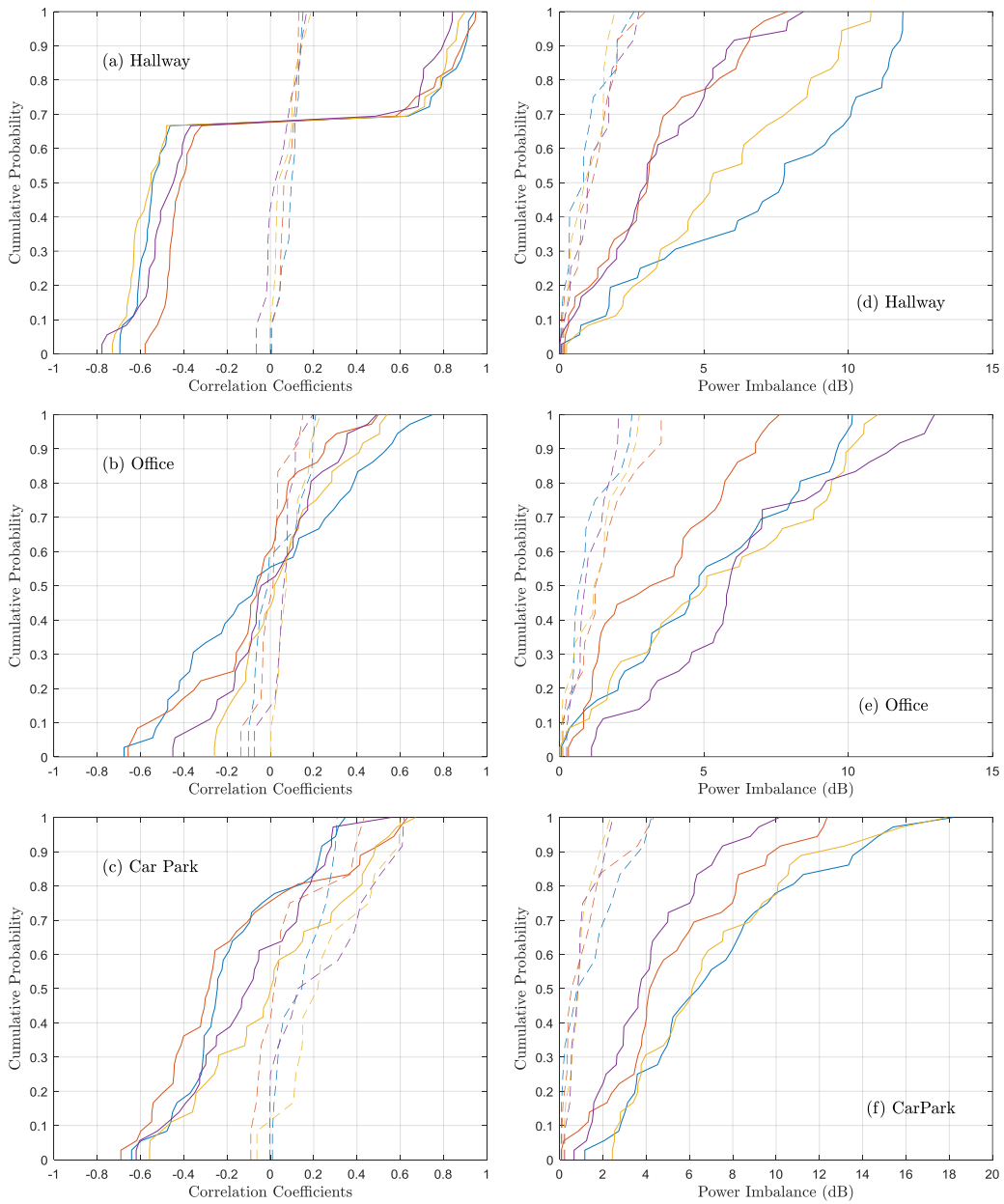

Figure 6.2: CDFs of the calculated cross-correlation coefficients and power imbalances of micro-diversity (dashed lines) and macro-diversity (continuous lines) systems for the chest (blue) and wrist (red) positions in the hallway, office and car park environments.

the macro-diversity setup. For example, the mean cross-correlation coefficient between the RX4 and RX8 was found to be -0.64 for the chest position in the hallway environment. This negative value indicates that an increase in the received signal power at the RX4 is associated with a decrease in the received signal power at the RX8. Furthermore, the majority of the cross-correlation coefficients for the hallway environment were greater than those for the open office and car park environments. Shadowing is generally caused by terrain configuration and

the presence of obstructions between the TX and RX. In wearable communications channels considered in this study, the body shadowing between the TX and RX is a predominant factor. As shown in Figure 6.1, the separation distance between the BS1 and BS2 (or equivalently the separation distance between the BS3 and BS4) is 1 m for the hallway environment. Consequently, due to the short separation distance between base stations in the hallway environment, the RXs 1 and 2 at the BS1 is more likely to experience similar shadowing caused by the user's body with the RXs 3 and 4 at the BS2 in the hallway environment compared to those for the office and car park environments.

6.4 Diversity Gain

The potential improvement in the received signal reliability that could be obtained using micro-diversity, macro-diversity and then combined micro- and macro-diversity systems is now evaluated using their DGs. For a micro-diversity system, as described in Chapter 5.1, the DG can be characterized as the measured improvement between the signal level at the output of the diversity combiner and that of the branch with the highest mean for a given probability or signal reliability. For a macro-diversity system, as defined in Chapter 5.2, this can be defined as the difference in signal level at the output of the diversity combiner and that of the target base station. For a combined micro- and macro-diversity system, the DG was estimated in the same manner as a macro-diversity system. In this study, RXs 7 and 8 were selected as the target base stations for *groups* 1 and 2 respectively to calculate the DG for the macro-diversity setup. To allow a direct comparison, the DG obtained by the combined micro- and macro-diversity setup was also evaluated using the same target base stations (i.e. RXs 7 and 8).

The average received signal power at each RX branch for all of the considered body worn node positions ranged between -65.2 dBm and -50.3 dBm in the hallway environment, between -63.0 dBm and -47.9 dBm in the open office environment and between -79.8 dBm and -60.3 dBm in the car park environment.

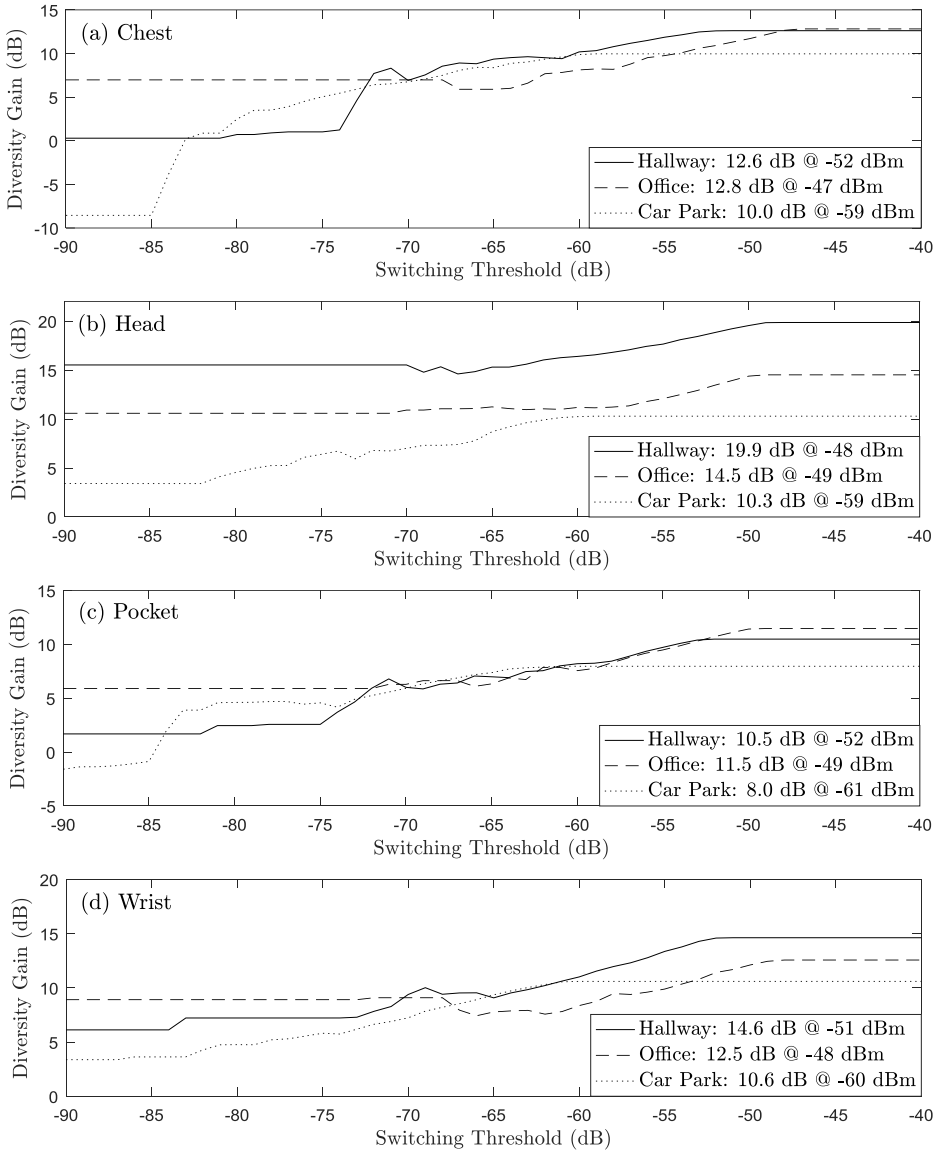

Figure 6.3: Mean DGs of the combined MRC-SECps system for increasing values of switching threshold for (a) chest, (b) head, (c) pocket and (d) wrist positions in each of the environments alongside the maximum achievable DGs at the optimum switching threshold.

The average output signal power of each MRC based micro-diversity combiner ranged between -60.7 dBm and -46.7 dBm in the hallway environment, between -58.0 dBm and -44.4 dBm in the open office environment and between -74.9 dBm and -57.0 dBm in the car park environment. Additionally, Figure 6.3 shows the achievable DGs for the combined MRC-SECps system with different switching threshold values ranging between -90 dBm and -40 dBm for all of the body worn node positions and environments alongside the maximum achievable DGs at the optimum switching threshold. It should be noted that the RX8 is

Table 6.1: Mean DGs for the MRC based micro-diversity and SECps based macro-diversity systems.

Environments	Positions	Diversity Gain (dB)					
		MRC based Micro-Diversity				SECps based Macro-Diversity	
		(1, 2)	(3, 4)	(5, 6)	(7, 8)	(1, 3, 5, 7)	(2, 4, 6, 8)
Hallway	Chest	6.4	6.5	5.0	4.8	8.9	6.9
	Head	5.2	5.3	5.0	5.9	16.6	15.1
	Pocket	5.5	6.7	5.2	5.5	7.4	6.0
	Wrist	6.4	5.3	5.0	5.5	11.2	9.0
Office	Chest	6.4	4.9	6.7	6.4	9.1	8.4
	Head	6.3	4.7	5.9	6.2	11.2	11.6
	Pocket	6.2	5.2	6.5	6.2	8.2	8.1
	Wrist	7.0	6.0	7.1	6.4	9.0	8.4
Car Park	Chest	3.4	5.5	4.4	4.2	6.7	5.5
	Head	3.6	5.5	4.6	4.1	6.8	5.6
	Pocket	5.8	4.1	4.5	5.1	4.7	5.0
	Wrist	2.1	4.7	3.9	3.7	7.7	7.8

considered as the target base station in Figure 6.3. Based on these, the switching threshold was determined as -50 dBm and -60 dBm for the indoor (i.e. hallway and office) and outdoor (i.e. car park) environments respectively to perform the DG analysis for the SECps based macro-diversity and combined MRC-SECps systems.

Table 6.1 presents the mean DG statistics averaged over the three trials for the MRC based micro-diversity system and the SECps based macro-diversity setup for all of the considered cases while Table 6.2 shows the mean DG statistics for the combined MRC-SECps configuration. For comparison, the mean DG obtained for the combined MRC-PSC setup is also shown in Table 6.2. It should be noted that all DG calculations were made at a signal reliability of 90%. As shown in Tables 6.1 and 6.2, all of the considered diversity systems (i.e. micro-diversity, macro-diversity and combined micro-and macro-diversity) provided a worthwhile DG. The mean DG obtained for the micro-diversity system ranged between 2.1 dB and 7.1 dB while this was between 4.7 dB and 16.6 dB for the macro-diversity

Table 6.2: Mean DGs for the combined micro- and macro-diversity system.

Environments	Positions	Diversity Gain (dB)			
		MRC-SECps		MRC-PSC	
		Target (RX7)	Target (RX8)	Target (RX7)	Target (RX8)
Hallway	Chest	12.6	10.9	12.6	10.9
	Head	19.5	18.6	19.9	18.9
	Pocket	10.5	10.0	10.5	10.0
	Wrist	14.6	13.0	14.6	13.0
Office	Chest	11.7	11.9	12.8	13
	Head	14.4	15.7	14.5	15.9
	Pocket	11.4	12.2	11.5	12.2
	Wrist	12.1	12.2	12.5	12.6
Car Park	Chest	9.9	9.2	10.0	9.2
	Head	10.2	9.4	10.3	9.5
	Pocket	8.0	9.3	8.0	9.3
	Wrist	10.6	11.4	10.6	11.4

system. Consulting Table 6.2, it is clear that the combined micro- and macro-diversity system provided a greater DG than using macro-diversity in isolation. More specifically, it was found that the combined MRC-SECps system provided worthwhile additional gains of between 2.6 dB and 4.3 dB. Furthermore, is is clear from Table 6.2 that the MRC-SECps system considered in this study provided a comparable performance compared to a MRC-PSC system.

As an example, Figures 6.4, 6.5 and 6.6 provide some empirical plots which illustrate the improving DGs achievable by each of the three diversity configurations (i.e. micro-diversity, macro-diversity and combined micro- and macro-diversity) for the wrist position in the hallway (Figure 6.4), office (Figure 6.5) and car park (Figure 6.6) environments during the second trial. Again, it can be seen that all of the three diversity configurations achieved a great improvement in the received signal. More specifically, for the hallway environment, the DGs obtained using the micro-diversity, macro-diversity and combined micro- and macro-diversity systems were found to be 5.4 dB, 9.7 dB and 13.9 dB respectively.

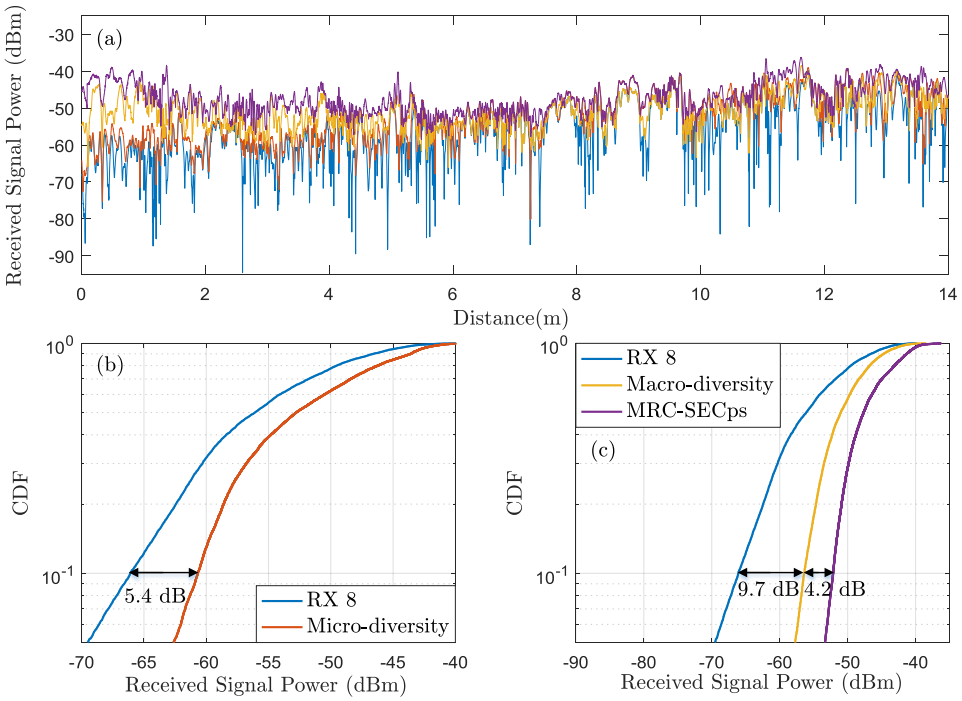

Figure 6.4: (a) Received signal power and (b) CDFs of the output of micro-diversity (RX7, RX8), (c) macro-diversity (*group* 2) and micro- and macro-diversity (MRC-SECps) systems alongside those of the RX8 for the wrist position in the hallway environment during the second trial.

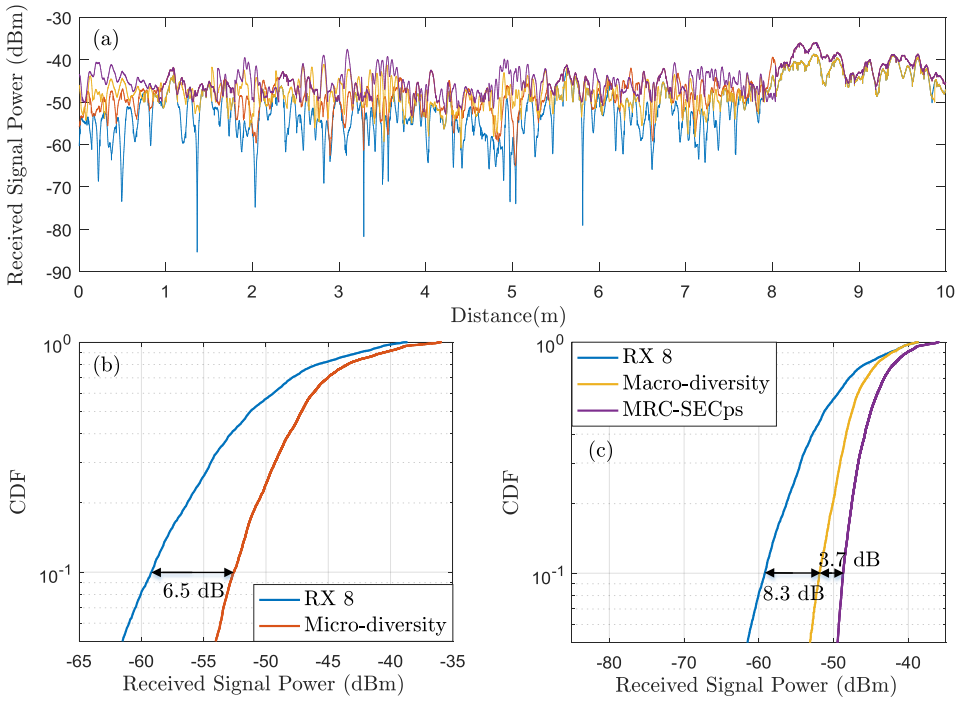

Figure 6.5: (a) Received signal power and (b) CDFs of the output of micro-diversity (RX7, RX8), (c) macro-diversity (*group* 2) and micro- and macro-diversity (MRC-SECps) systems alongside those of the RX8 for the wrist position in the office environment during the second trial.

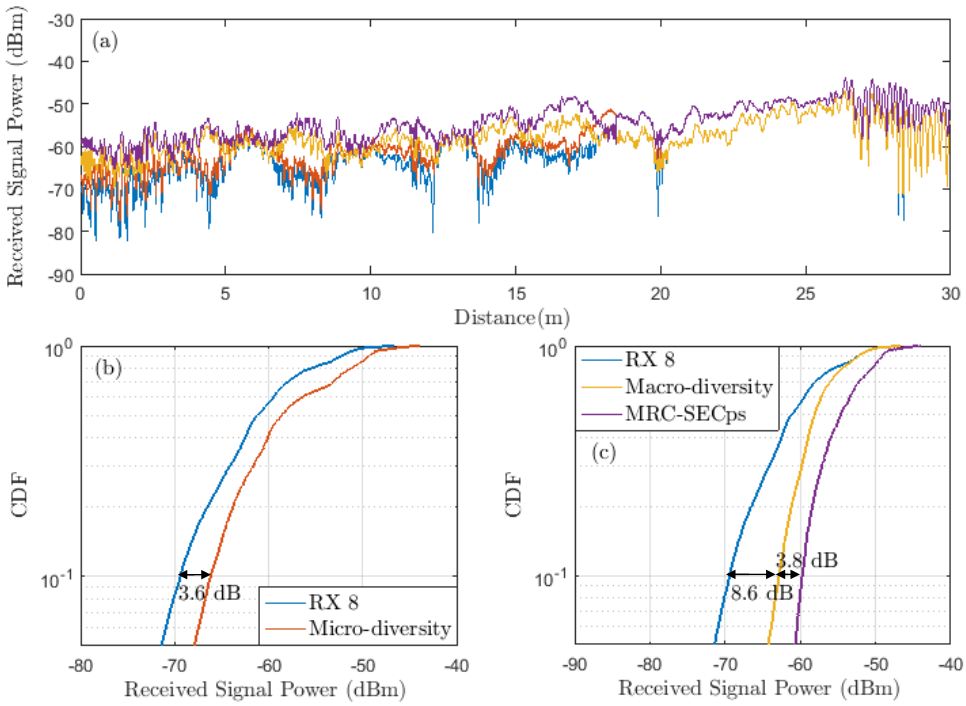

Figure 6.6: (a) Received signal power and (b) CDFs of the output of micro-diversity (RX7, RX8), (c) macro-diversity (*group* 2) and micro- and macro-diversity (MRC-SECps) systems alongside those of the RX8 for the wrist position in the outdoor car park environment during the second trial.

6.5 Conclusion

The MRC based micro-diversity, SECps based macro-diversity and MRC-SECps based micro- and macro-diversity systems have been considered to counteract the negative effects of multipath and shadowing for wearable communications. To this end, field measurements were performed in both indoor and outdoor environments and their performance were evaluated in terms of DG. Prior to the DG, the cross-correlation coefficient and power imbalance were calculated.

It was shown that the power imbalances for the micro-diversity configuration were smaller than those for the macro-diversity setup. Additionally, for the micro-diversity configuration, the multipath fading observed at each RX in the outdoor environment was more correlated compared to the indoor environments. For the macro-diversity configuration, the cross-correlation coefficients for the hallway environment were observed to be greater than those for the office and car park environments due to the short separation distance between base sta-

tions. Additionally, it was found that all three diversity configurations provided a worthwhile DG. In particular, up to 7.1 dB, 16.6 dB and 19.9 dB DG can be achieved when using MRC based micro-diversity, SECps based macro-diversity and then MRC-SECps based micro- and macro-diversity systems respectively.

Chapter 7

Conclusion and Future Work

In this thesis, a number of new composite fading models, namely $\mathcal{F}$, κ-μ / inverse gamma and η-μ / inverse gamma, have been proposed. It has been demonstrated that these models can accurately describe the composite fading signal observed in wearable communications channels and frequently provide a better fit to the measurement data compared to other composite fading models. The proposed composite fading models will find application in the general area of wireless communications and beyond (i.e. non-wearable communications) although their applicabilities are restricted to wearable applications in this thesis. Then, switched combining based micro-diversity and switched combining based macro-diversity systems have been studied to overcome multipath and shadowing respectively in wearable channels. Building upon this, combined micro- and macro-diversity configuration has been considered to mitigate the negative effects caused by simultaneous existence of multipath and shadowing for wearable communications.

7.1 Conclusion

After stating the motivations and contributions for the thesis in Chapter 1, to help with the understanding of the work, the necessary background knowledge and the relevant literature on path loss, multipath, shadowing and composite fading models were presented in Chapter 2. Additionally, a description of the operation of a number of different diversity combining schemes along with the concepts of DG, correlation and power imbalance were introduced. Also in Chapter 2, the

RAD was introduced to evaluate the goodness-of-fit while the AICc metric was presented to as a criterion for model selection.

Chapter 3 presented the κ-μ / inverse gamma composite fading model as a means to characterize the behaviour of the composite fading signal observed in LOS wearable communications channels. Its key statistical metrics (i.e. PDF, CDF, higher order moments, AF and MGF) were obtained in simple closed-form expressions. The versatility of the κ-μ / inverse gamma composite fading model was demonstrated through reduction to some special cases which coincide with existing well-known distributions as well as its ability to approximate other composite fading models. Furthermore, the use of the κ-μ / inverse gamma composite fading model to characterize LOS wearable communications channels was validated using an exhaustive set of field measurements coverage a wide range of environments. It was shown that the model provided a good fit to the composite fading over all of the LOS wearable channel measurements. Most importantly though, using the AICc, the κ-μ / inverse gamma composite fading model was selected as the most likely candidate model for the majority of the considered cases.

Chapter 4 proposed the $\mathcal{F}$ and η-μ / inverse gamma composite fading models to characterize the behaviour of the composite fading signal observed in NLOS wearable communications channels. Their fundamental statistics were obtained in simple and convenient closed-form expressions with the exception of the CDF and MGF for the η-μ / inverse gamma composite fading model. Nonetheless, straightforward analytical formulations were obtained using infinite series expansions. Similar to the κ-μ / inverse gamma composite fading model presented in Chapter 3, both the $\mathcal{F}$ and η-μ / inverse gamma composite fading models include other well-known distributions as special cases. As demonstrated in Chapter 4, they can also be used to provide a good approximation to other more complicated composite fading models. The versatility of the proposed $\mathcal{F}$ and η-μ / inverse gamma composite fading models was validated using a diverse range of

NLOS wearable channel measurements. Interestingly for the majority of the experiments conducted in this thesis, the η parameter estimate for the η-μ / inverse gamma composite model was equal to unity (i.e. the scattered wave power of the in-phase and quadrature components of each cluster of multipath were identical). Consequently, the $\mathcal{F}$ and η-μ / inverse gamma composite fading models coincided. Using an analysis of the AICc, it was found that the $\mathcal{F}$ composite fading model was determined as the most likely candidate model for the majority of cases due to its reliance on a fewer number of parameters compared to the η-μ / inverse gamma model.

In Chapter 5, the potential improvement in signal reliability for wearable communications channels which undergo multipath fading was investigated using a switched combining based micro-diversity setup. Following from this, a switched combining based macro-diversity configuration was studied with the aim of mitigating shadowing. Among SSC, SEC and SECps schemes, an SECps scheme provided the best performance. Nonetheless, this improvement was not open-ended as its implementation will add extra complexity to the design of the switched diversity system. The impact of different switching thresholds on the DG, number of path examinations and number of path switches were studied to emphasize the importance of selecting an appropriate switching threshold. The fading observed at the output of both the switched combining based micro-diversity and switched combining based macro-diversity systems were statistically characterized using their diversity specific analytical equations. Using an analysis of the RAD, it was shown that that the theoretical PDFs provided an adequate fit to the measured data.

A systematic investigation of the use of combined micro- and macro-diversity system to mitigate simultaneous multipath and shadowing for wearable communications channels was presented in Chapter 6. Here, the use of an MRC scheme at the base station (i.e. micro-diversity) and an SECps scheme for switching between the base stations (i.e. macro-diversity) were considered (i.e. combined

MRC-SECps stages). It was found that the combined MRC-SECps system provided additional gains of between 2.6 dB and 4.3 dB compared to when the SECps based macro-diversity system was utilised in isolation.

7.2 Future Work

This thesis has provided important contributions to our understanding of the composite fading signal observed in wearable communications channels. It has proposed three novel composite fading models, which although aimed at wearable applications, will find application in the general area of wireless communications and beyond. As well as this the thesis has studied diversity techniques aimed at mitigating the deleterious effects of multipath and shadowing. Nonetheless, there are still some issues that warrant investigation in the future. These include:

- **The second-order statistics of wearable channels which undergo composite fading**: Second-order statistics, such as the level crossing rate (LCR) and average fade duration (AFD), can complement the first-order statistics which has mainly been addressed in this thesis. They are useful in the design of wearable systems and the analysis of its performance because they give a direct indication of the rate of change with respect to time. For instance, the LCR and AFD can carry useful information about burst error statistics [107], which facilitate the design and selection of error correcting techniques. They can also be used for the optimization of interleaver size, choosing the buffer depth for adaptive modulation schemes, system throughput analysis and channel modelling [108, 109].

  There exist a number of studies on the second-order statistics of composite fading models [62, 63, 110]. More specifically, the expressions for the LCR and AFD of Rice / lognormal [63], Rice / Nakagami [62] and shadowed κ-μ [110] models have been presented. However, for the majority of cases, closed-form expressions for the LCR and AFD are not available and thus are not convenient to work with. Furthermore, they assume that the dominant

signal components are subject to shadowing. As discussed in this thesis, it is more appropriate to assume that both the dominant and scattered signal components are shadowed together in wearable communications channels. Accordingly, simple closed-form expressions for both the LCR and AFD of the proposed composite fading models should be derived and employed to further evaluate the performance of wearable systems.

- **Diversity reception over composite fading channels**: The sum and the maximum of random variables can play an important role in the performance analysis of diversity combining schemes (e.g. PSC and MRC) for wireless communications. Therefore, simple closed-form expressions for both the PDFs and CDFs of the sum and maximum of $\mathcal{F}$, κ-μ / inverse gamma and η-μ / inverse gamma random variables should be derived and compared with some empirical data obtained from field measurements. Furthermore, the behaviour of the composite fading signal observed at the output of PSC and MRC diversity systems should be statistically characterised using the derived PDFs and CDFs.

  Diversity reception over composite fading channels can be expanded to multiple-input and multiple-output (MIMO) systems to take into account multiple antennas at both TX and RX. The use of MIMO techniques can provide a significant increase in the channel capacity for high data rate applications. MIMO systems exploit multipath provided in rich scattering environments to achieve an increase in channel capacity and high data rates. Correlation between the different antenna elements and shadowing have a important impact on the capacity and bit error rate performance of MIMO systems. Therefore, for wearable communications, it is more appropriate to deploy multiple antennas with a separation distance of the order of (or shorter than) the signal wavelength (i.e. micro) for wearable nodes to avoid the potential obtrusion to the user. On the other hand, it is more suitable to deploy multiple antennas in different, spatially separated base stations

for which the spacing is much longer than the signal wavelength (i.e. macro) to alleviate shadowing. This setup will effectively combat multipath fading and shadowing observed in wearable channels and thus improve the signal reliability. Accordingly, the potential improvement in signal reliability of the wearable channels which can be obtained by MIMO systems should be empirically investigated with the corresponding correlation analysis.

- **Spatial and temporal characterization of wearable channels**: Systems with multiple antennas require channel models that characterize both spatial and temporal characteristics of the channel. For wearable systems with high data rates and directional antennas, it is more complex to characterize multipath compared to that for omnidirectional and narrowband systems which have mainly been addressed in this thesis. Multipath components can be classified either by their angle of arrival (AOA) or time of arrival (TOA). The corresponding channel characteristics can be recorded as a power delay profile (PDP) or a power angle profile (PAP). A PDP records temporal power distribution relative to multipath TOA and a PAP records spatial power distribution relative to multipath AOA [111]. The TOA parameters include mean excess delay, rms delay spread, timing jitter and standard deviation while the AOA parameters contain angular spread, angular constriction, maximum fading angle and maximum AOA direction. Accordingly, a detailed analysis on spatial and temporal characteristics of wearable channels should be performed using an extensive measurement campaign in the future. These measurement results will provide not only important empirical values for wearable system design, but also a better understanding of the radio wave propagation observed in wearable channels.

- **Millimetre-wave wearable communications**: Much interest has been generated towards the use of millimetre-wave (mm-wave) technologies for wearable systems [112–117]. Advancements in this area mean that it will

soon be feasible to use operating frequencies in the 59-66 GHz range to provide high bandwidth capabilities for these applications. Operating wearable systems within this part of the mm-wave spectrum will be attractive for many reasons, not least due to the small size of antenna that can be used [113], the lower interference and much greater frequency reuse that can be achieved over smaller areas [116] compared to competing microwave technologies.

Despite these apparent benefits, there are a number of key challenges which need to be surmounted before realizing the use of wearables in these frequency bands. These include shadowing, rapid channel fluctuations, intermittent connectivity, processing power consumption and health related issues [118]. In particular, due to wearables operating in close proximity to the human body, the channels will be prone to shadowing induced by the movement of body parts and blockages caused by user's body and/or surroundings. For example, materials such as brick can attenuate signals by approximately 40-80 dB [119,120] while the human body itself can result in up to 35 dB loss [121]. To address all of these issues, the proposed composite fading models should be used to characterize the composite fading behaviour observed in wearable communication channels at mm-wave frequencies. Moreover, the switched diversity schemes considered in the thesis should be applied to mm-wave wearable communications to improve the connectivity and reduce the power consumption.

Appendix A

Author's Publications

A.1 Publications related to the thesis

- **S. K. Yoo**, S. L. Cotton, P. C. Sofotasios, M. Matthaiou, M. Valkama and G. K. Karagiannidis, "The κ-μ / inverse gamma fading model," in *IEEE International Symposium on Personal, Indoor and Mobile Radio Communications (PIMRC)*, Hong Kong, China, Sep. 2015, pp. 425-429 **(Chapter 3)**.

- **S. K. Yoo**, N. Bhargav, S. L. Cotton, P. C. Sofotasios, M. Matthaiou, M. Valkama and G. K. Karagiannidis, "The κ-μ / inverse gamma and η-μ / inverse gamma composite fading models: Fundamental statistics and empirical validation," *submitted in Apr. 2017 to IEEE Transactions on Communications* **(Chapters 3 & 4)**.

- **S. K. Yoo** and S. L. Cotton, "Composite fading in non-line-of-sight off-body communications channels," *presented at European Conference on Antennas and Propagation (EuCAP)*, Paris, France, Mar. 2017 **(Chapter 4)**.

- **S. K. Yoo**, S. L. Cotton, P. C. Sofotasios, M. Matthaiou, M. Valkama and G. K. Karagiannidis, "The Fisher-Snedecor $\mathcal{F}$ distribution in the context of composite fading model," *accepted, IEEE Communications Letters in Feb. 2017* **(Chapter 4)**.

- **S. K. Yoo**, S. L. Cotton, P. C. Sofotasios, M. Matthaiou, M. Valkama and G. K. Karagiannidis, "The η-μ / inverse gamma composite fading

model," in *IEEE International Symposium on Personal, Indoor and Mobile Radio Communications (PIMRC)*, Hong Kong, China, Sep. 2015, pp. 166-170 **(Chapter 4)**.

- **S. K. Yoo**, S. L. Cotton, W. G. Scanlon and G. A. Conway, "An experimental evaluation of switched combining based macro-diversity for wearable communications operating in an outdoor environment," *accepted, IEEE Transactions on Wireless Communications* in Mar. 2017 **(Chapter 5)**.

- **S. K. Yoo**, S. L. Cotton and W. G. Scanlon, "Switched diversity techniques for indoor off-body communications channels: An experimental analysis and modelling," *IEEE Transactions on Antennas and Propagation*, vol. 64, no. 7, pp. 3201-3206, Jul. 2016 **(Chapter 5)**.

- **S. K. Yoo** and S. L. Cotton, "An evaluation of micro and macro based diversity combining for wearable communications," *to be presented at IEEE Antennas and Propagation Society International Symposium (APSURSI)*, San Diego, USA, Jul. 2017 **(Chapter 6)**.

A.2 Publications not related to the thesis

- **S. K. Yoo**, S. L. Cotton, Y. J. Chun, W. G. Scanlon and G. A. Conway, "Channel characteristics of dynamic off-body communications at 60 GHz under line-of-sight (LOS) and non-LOS conditions," *accepted, IEEE Antennas and Wireless Propagation Letters in Dec. 2016.*

- **S. K. Yoo**, S. L. Cotton, R. W. Heath Jr. and Y. J. Chun, "Measurements of the 60 GHz UE to eNB channel for small cell deployments," *accepted, IEEE Wireless Communications Letters in Dec. 2016.*

- **S. K. Yoo**, S. L. Cotton, P. C. Sofotasios and S. Freear, "Shadowed fading in indoor off-body communications channels: A statistical characterization using the κ-μ / gamma composite fading model," *IEEE Transactions on Wireless Communications*, vol. 15, no. 8, pp. 5231-5244, Aug. 2016.

- **S. K. Yoo**, S. L. Cotton, A. McKernan and W. G. Scanlon, "Signal reliability improvement using selection combining based macro-diversity for off-body communications at 868 MHz," in *European Conference on Antennas and Propagation (EuCAP)*, Lisbon, Portugal, Apr. 2015, pp. 1-5.

- **S. K. Yoo**, S. L. Cotton and P. C. Sofotasios, "A statistical characterization of shadowed fading in indoor off-body communications channels at 5.8 GHz," in *European Conference on Antennas and Propagation (EuCAP)*, Lisbon, Portugal, Apr. 2015, pp. 1-5.

- **S. K. Yoo** and S. L. Cotton, "Indoor off-body communications at 5.8 GHz with multiple antennas at the base station: A statistical characterization using the Nakagami-*m* fading model," in *URSI General Assembly and Scientific Symposium (URSI GASS)*, Beijing, China, Aug. 2014, pp. 1-4.

- **S. K. Yoo** and S. L. Cotton, "Small-scale fading characteristics of diversity combining schemes used for body-to-body communications within an urban environment at 2.45 GHz," in *URSI General Assembly and Scientific Symposium (URSI GASS)*, Beijing, China, Aug. 2014, pp.1-4.

- **S. K. Yoo**, S. L. Cotton and M. G. Doone, "Fading characteristics of indoor off-body communications with multiple-antennas at the base station," in *IEEE Antennas and Propagation Society International Symposium (APSURSI)*, Memphis, USA, Jul. 2014, pp. 719-720.

- **S. K. Yoo**, S. L. Cotton and M. G. Doone, "An experimental evaluation of spatial diversity for body-to-body communications within an urban environment at 2.45 GHz," in *IEEE Antennas and Propagation Society International Symposium (APSURSI)*, Memphis, USA, Jul. 2014, pp. 721-722.

- **S. K. Yoo** and S. L. Cotton, "Improving signal reliability for indoor off-body communications using spatial diversity at the base station," in *European Conference on Antennas and Propagation (EuCAP)*, The Hague, Netherlands, Apr. 2014, pp. 857-861.

- Y. J. Chun, S. L. Cotton, H. S. Dhillon, F. J. Lopez-Martinez, J. F. Paris and **S. K. Yoo**, "A comprehensive analysis of 5G heterogeneous cellular system operation over κ-μ shadowed fading channels," *under revision, IEEE Transactions on Wireless Communications*, Mar. 2017.

- S. L. Cotton, **S. K. Yoo** and P. C. Sofotasios, "Characterizing fading in wearable communications channels using composite models," in *Asilomar Conference on Signals, Systems and Computers (ACSSC)*, Pacific Grove, CA, USA, Nov. 2015, pp. 887-881.

- S. L. Cotton, **S. K. Yoo** and W. G. Scanlon, "A measurements based comparison of new and classical models used to characterize fading in body area networks," in *IEEE International Microwave Workshop Series on RF and Wireless Technologies for Biomedical and Healthcare Applications (IMWS-Bio)*, London, United Kingdom, Dec. 2014, pp. 1-4.

- S. L. Cotton, **S. K. Yoo** and M. G. Doone, "A statistical characterization of on-body fading using the shadowed κ-μ fading model," in *IEEE Antennas and Propagation Society International Symposium (APSURSI)*, Memphis, USA, Jul. 2014, pp.717-718.

References

[1] Beecham Research, visited on 04/04/2017. [Online]. Available: http://www.beechamresearch.com/download.aspx?id=36

[2] Nature, visited on 11/06/2017. [Online]. Available: http://www.nature.com/news/what-could-derail-the-wearables-revolution-1.18263

[3] GSMA, visited on 11/06/2017. [Online]. Available: https://www.gsma.com/iot/news/new-report-backs-mass-adoption-of-wearables/

[4] CCS Insight, visited on 04/04/2017. [Online]. Available: http://www.ccsinsight.com/press/company-news/2516-wearables-momentum-continues

[5] CNBC, visited on 04/04/2017. [Online]. Available: http://www.cnbc.com/2015/09/22/after-smartphones-wearable-tech-poised-to-be-next-big-thing.html

[6] *IEEE standard for local and metropolitan area networks - Part 15.4: Low-Rate Wireless Personal Area Networks (LR-WPANS).* IEEE Std. 802.15.4, May 2003.

[7] *IEEE standard for local and metropolitan area networks - Part 15.6: Wireless Body Area Networks (WBAN).* IEEE Std. 802.15.6, Feb. 2012.

[8] H.-R. Chuang, "Human operator coupling effects on radiation characteristics of a portable communication dipole antenna," *IEEE Transactions on Antennas and Propagation*, vol. 42, no. 4, pp. 556–560, Apr. 1994.

[9] W. G. Scanlon and N. E. Evans, "Numerical analysis of bodyworn UHF antenna systems," *Electronics and Communication Engineering Journal*, vol. 13, no. 2, pp. 53–64, Apr. 2001.

[10] M. Okoniewski and M. A. Stuchly, "A study of the handset antenna and human body interaction," *IEEE Transactions on Microwave Theory and Techniques*, vol. 44, no. 10, pp. 1855–1864, Aug. 1996.

[11] S. L. Cotton, A. McKernan, A. J. Ali, and W. G. Scanlon, "An experimental study on the impact of human body shadowing in off-body communications channels at 2.45 GHz," in *European Conference on Antennas and Propagation (EuCAP)*, Apr. 2011, pp. 3133–3137.

[12] R. Rosini, R. Verdone, and R. D'Errico, "Body-to-body indoor channel modeling at 2.45 GHz," *IEEE Transactions on Antennas and Propagation*, vol. 62, no. 11, pp. 5807–5819, Nov. 2014.

[13] C. W. Kim, T. S. P. See, T. M. Chiam, Y. Ge, Z. N. Chen, and S. Sun, "Channel characterization of walking passerby's effects on 2.48-GHz wireless body area network," *IEEE Transactions on Antennas and Propagation*, vol. 61, no. 3, pp. 1495–1498, Mar. 2013.

[14] A. A. Serra, P. Nepa, G. Manara, and P. S. Hall, "Diversity measurements for on-body communication systems," *IEEE Antennas and Wireless Propagation Letters*, vol. 6, pp. 361–363, Oct. 2007.

[15] J. G. Proakis, "Digital communications," *McGraw-Hill, New York*.

[16] M. K. Simon and M.-S. Alouini, *Digital communication over fading channels*, 2nd ed. New York: Wiley, 2005.

[17] ——, "A unified approach to the performance analysis of digital communication over generalized fading channels," *Proceedings of the IEEE*, vol. 86, no. 9, pp. 1860–1877, Sep. 1998.

[18] Q. H. Abbasi, M. M. Khan, S. Liaqat, A. Alomainy, and Y. Hao, "Ultra wideband off-body radio channel characterisation for different environments," in *International Conference on Electrical and Computer Engineering (ICECE)*, Dec. 2012, pp. 165–168.

[19] M. Mackowiak and L. M. Correia, "Towards a radio channel model for off-body communications in a multipath environment," in *European Wireless Conference (EW)*, Apr. 2012, pp. 1–7.

[20] S. L. Cotton and W. G. Scanlon, "Characterization and modeling of the indoor radio channel at 868 MHz for a mobile bodyworn wireless personal area network," *IEEE Antennas and Wireless Propagation Letters*, vol. 6, pp. 51–55, Mar. 2007.

[21] R. Rosini and R. D'Errico, "Off-body channel modelling at 2.45 GHz for two different antennas," in *European Conference on Antennas and Propagation (EuCAP)*, Mar. 2012, pp. 3378–3382.

[22] A. A. Goulianos, T. W. Brown, B. G. Evans, and S. Stavrou, "Wideband power modeling and time dispersion analysis for UWB indoor off-body communications," *IEEE Transactions on Antennas and Propagation*, vol. 57, no. 7, pp. 2162–2171, Jul. 2009.

[23] K. I. Ziri-Castro, W. G. Scanlon, and N. E. Evans, "Indoor radio channel characterization and modeling for a 5.2 GHz bodyworn receiver," *IEEE Antennas and Wireless Propagation Letters*, vol. 3, no. 1, pp. 219–222, Dec. 2004.

[24] S. L. Cotton, "A statistical model for shadowed body-centric communications channels: Theory and validation," *IEEE Transactions on Antennas and Propagation*, vol. 62, no. 3, pp. 1416–1424, Mar. 2014.

[25] S. K. Yoo, S. L. Cotton, P. C. Sofotasios, and S. Freear, "Shadowed fading in indoor off-body communication channels: A statistical characterization

using the κ-μ / gamma composite fading model," *IEEE Transactions on Wireless Communications*, vol. 15, no. 8, pp. 5231–5244, Aug. 2016.

[26] S. L. Cotton and W. G. Scanlon, "Channel characterization for single-and multiple-antenna wearable systems used for indoor body-to-body communications," *IEEE Transactions on Antennas and Propagation*, vol. 57, no. 4, pp. 980–990, Apr. 2009.

[27] I. Khan, L. Yu, Y. I. Nechayev, and P. S. Hall, "Space and pattern diversity for on-body communication channels in an indoor environment at 2.45 GHz," in *European Conference on Antennas and Propagation (EuCAP*, Nov. 2007, pp. 1–6.

[28] S. L. Cotton and W. G. Scanlon, "Characterization and modeling of on-body spatial diversity within indoor environments at 868 MHz," *IEEE Transactions on Wireless Communications*, vol. 8, no. 1, pp. 176–185, Jan. 2009.

[29] Q. H. Abbasi, M. M. Khan, A. Alomainy, and Y. Hao, "Diversity antenna techniques for enhanced ultra wideband body-centric communications," in *IEEE Antennas and Propagation Society International Symposium (APSURSI)*, Jul. 2011, pp. 1323–1326.

[30] A. J. Ali, S. L. Cotton, and W. G. Scanlon, "Spatial diversity for off-body communications in an indoor populated environment at 5.8 GHz," in *Loughborough Antennas and Propagation Conference (LAPC)*, Nov. 2009, pp. 641–644.

[31] C. Ahn, B. Ahn, S. Kim, and J. Choi, "Experimental outage capacity analysis for off-body wireless body area network channel with transmit diversity," *IEEE Transactions on Consumer Electronics*, vol. 58, no. 2, pp. 274–277, May 2012.

[32] S. L. Cotton, W. G. Scanlon, and A. McKernan, "Improving signal reliability in outdoor body-to-body communications using front and back positioned antenna diversity," in *European Conference on Antennas and Propagation (EuCAP)*, Mar. 2012, pp. 3393–3396.

[33] S. L. Cotton and W. G. Scanlon, "Measurements, modeling and simulation of the off-body radio channel for the implementation of bodyworn antenna diversity at 868 MHz," *IEEE Transactions on Antennas and Propagation*, vol. 57, no. 12, pp. 3951–3961, Dec. 2009.

[34] S. L. Cotton, R. D'Errico, and C. Oestges, "A review of radio channel models for body centric communications," *Radio Science*, vol. 49, no. 6, pp. 371–388, Jun. 2014.

[35] M. Patel and J. Wang, "Applications, challenges, and prospective in emerging body area networking technologies," *IEEE Wireless Communications*, vol. 17, no. 1, pp. 80–88, Feb. 2010.

[36] T. S. Rappaport, *Wireless communications: Principles and practice*. Upper Saddle River, NJ, USA: Prentice-Hall, 2002.

[37] S. J. Ambroziak *et al.*, "An off-body channel model for body area networks in indoor environments," *IEEE Transactions on Antennas and Propagation*, vol. 64, no. 9, pp. 4022–4035, Sep. 2016.

[38] M. Mackowiak and L. M. Correia, "Statistical path loss model for dynamic off-body channels," in *IEEE International Symposium on Personal, Indoor, and Mobile Radio Communication (PIMRC)*, Sep. 2014, pp. 53–57.

[39] S. L. Cotton and W. G. Scanlon, "Received signal characteristics of the indoor off-body communications channel at 5.8 GHz," in *IEEE Antennas and Propagation Society International Symposium (APSURSI)*, Jul. 2013, pp. 1952–1953.

[40] M. M. Khan, Q. H. Abbasi, A. Alomainy, and Y. Hao, "Study of line of sight (LOS) and none line of sight (NLOS) ultra wideband off-body radio propagation for body centric wireless communications in indoor," in *European Conference on Antennas and Propagation (EuCAP)*, Apr. 2011, pp. 110–114.

[41] A. A. Goulianos, T. W. C. Brown, and S. Stavrou, "A novel path-loss model for UWB off-body propagation," in *IEEE Vehicular Technology Conference (VTC)*, May 2008, pp. 450–454.

[42] H. B. Janes and P. I. Wells, "Some tropospheric scatter propagation measurements near the radio horizon," *Proceedings of the IRE*, vol. 43, no. 10, pp. 1336–1340, Oct. 1955.

[43] S. Basu and other, "250 MHz/GHz scintillation parameters in the equatorial, polar, and auroral environments," *IEEE Journal on Selected Areas in Communications*, vol. 5, no. 2, pp. 102–115, Feb. 1987.

[44] S. O. Rice, "Statistical properties of a sine wave plus random noise," *Bell Labs Technical Journal*, vol. 27, no. 1, pp. 109–157, Jan. 1948.

[45] R. J. C. Bultitude, S. A. Mahmoud, and W. A. Sullivan, "A comparison of indoor radio propagation characteristics at 910 MHz and 1.75 GHz," *IEEE Journal on Selected Areas in Communications*, vol. 7, no. 1, pp. 20–30, Jan. 1989.

[46] W. R. Braun and I. Dersch, "A physical mobile radio channel model," *IEEE Transactions on Vehicular Technology*, vol. 40, no. 2, pp. 472–482, May 1991.

[47] M. Nakagami, "The m-distribution: A general formula of intensity distribution of rapid fading," *Statistical Method of Radio Propagation*, 1960.

[48] M. D. Yacoub, "The κ-μ distribution and the η-μ distribution," *IEEE Antennas and Propagation Magazine*, vol. 49, no. 1, pp. 68–81, Feb. 2007.

[49] A. Fort, C. Desset, P. Wambacq, and L. V. Biesen, "Indoor body-area channel model for narrowband communications," *IET Microwaves, Antennas and Propagation*, vol. 1, no. 6, pp. 1197–1203, Dec. 2007.

[50] M. Abramowitz and I. A. Stegun, *Handbook of mathematical functions*. Washington, DC, US Dept. of Commerce, National Bureau of Standards, 1972.

[51] S. L. Cotton and W. G. Scanlon, "An experimental investigation into the influence of user state and environment on fading characteristics in wireless body area networks at 2.45 GHz," *IEEE Transactions on Wireless Communications*, vol. 8, no. 1, pp. 6–12, Jan. 2009.

[52] W. G. Scanlon and S. L. Cotton, "Understanding on-body fading channels at 2.45 GHz using measurements based on user state and environment," in *Loughborough Antennas and Propagation Conference (LAPC)*, Mar. 2008, pp. 10–13.

[53] I. S. Gradshteyn and I. M. Ryzhik, *Table of Integrals, Series, and Products*, 7th ed. London: Academic Press, 2007.

[54] M. Kim and J.-I. Takada, "Characterization of wireless on-body channel under specific action scenarios at sub-GHz bands," *IEEE Transactions on Antennas and Propagation*, vol. 60, no. 11, pp. 5364–5372, Nov. 2012.

[55] G. L. Stuber, *Principles of mobile communication*. Springer Science & Business Media, 2011.

[56] H. Hashemi, "The indoor radio propagation channel," *Proceedings of the IEEE*, vol. 81, no. 7, pp. 943–968, Jul. 1993.

[57] F. Vatalaro and F. Mazzenga, "Statistical channel modelling and performance evaluation in satellite personal communications," *International Journal of Satellite Communications*, vol. 16, no. 5, pp. 249–255, Oct. 1998.

[58] J. R. Clark and S. Karp, "Approximations for lognormally fading optical signals," *Proceedings of the IEEE*, vol. 58, no. 12, pp. 1964–1965, Dec. 1970.

[59] A. Abdi and M. Kaveh, "On the utility of gamma PDF in modeling shadow fading (slow fading)," in *IEEE Vehicular Technology Conference (VTC)*, vol. 3, May 1999, pp. 2308–2312.

[60] I. Trigui, A. Laourine, S. Affes, and A. Stephenne, "The inverse Gaussian distribution in wireless channels: Second-order statistics and channel capacity," *IEEE Transactions on Communications*, vol. 60, no. 11, pp. 3167–3173, Nov. 2012.

[61] Y. Hao *et al.*, "Statistical and deterministic modelling of radio propagation channels in WBAN at 2.45 GHz," in *IEEE Antennas and Propagation Society International Symposium (APSURSI)*, Jul. 2006, pp. 2169–2172.

[62] A. Abdi, W. C. Lau, M.-S. Alouini, and M. Kaveh, "A new simple model for land mobile satellite channels: First-and second-order statistics," *IEEE Transactions on Wireless Communications*, vol. 2, no. 3, pp. 519–528, May 2003.

[63] C. Loo, "A statistical model for a land mobile satellite link," *IEEE Transactions on Vehicular Technology*, vol. 34, no. 3, pp. 122–127, Aug. 1985.

[64] G. E. Corazza and F. Vatalaro, "A statistical model for land mobile satellite channels and its application to nongeostationary orbit systems," *IEEE Transactions on Vehicular Technology*, vol. 43, no. 3, pp. 738–742, Aug. 1994.

[65] F. Hansen and F. I. Meno, "Mobile fading - Rayleigh and lognormal superimposed," *IEEE Transactions on Vehicular Technology*, vol. 26, no. 4, pp. 332–335, Nov. 1977.

[66] H. Suzuki, "A statistical model for urban radio propogation," *IEEE Transactions on Communications*, vol. 25, no. 7, pp. 673–680, Jul. 1977.

[67] T. T. Tjhung and C. C. Chai, "Fade statistics in microcellular mobile radio channels with shadowing," in *IEEE International Conference on Communications (ICC)*, Jun. 1998, pp. 1645–1649.

[68] I. M. Kostić, "Analytical approach to performance analysis for channel subject to shadowing and fading," *IEE Proceedings on Communications*, vol. 152, no. 6, pp. 821–827, Dec. 2005.

[69] A. Abdi and M. Kaveh, "K distribution: An appropriate substitute for Rayleigh-lognormal distribution in fading-shadowing wireless channels," *IET Electronics Letters*, vol. 34, no. 9, pp. 851–852, Apr. 1998.

[70] T. Eltoft, "The Rician inverse Gaussian distribution: A new model for non-Rayleigh signal amplitude statistics," *IEEE Transactions on Image Processing*, vol. 14, no. 11, pp. 1722–1735, Nov. 2005.

[71] Karmeshu and R. Agrawal, "On efficacy of Rayleigh-inverse Gaussian distribution over K-distribution for wireless fading channels," *Wireless Communications and Mobile Computing*, vol. 7, no. 1, pp. 1–7, Jan. 2007.

[72] A. Laourine, M.-S. Alouini, S. Affes, and A. Stéphenne, "On the performance analysis of composite multipath/shadowing channels using the G-distribution," *IEEE Transactions on Communications*, vol. 57, no. 4, pp. 1162–1170, Apr. 2009.

[73] J. F. Paris, "Statistical characterization of κ-μ shadowed fading," *IEEE Transactions on Vehicular Technology*, vol. 63, no. 2, pp. 518–526, Feb. 2014.

[74] S. L. Cotton, "Human body shadowing in cellular device-to-device communications: Channel modeling using the shadowed κ-μ fading model," *IEEE Journal on Selected Areas in Communications*, vol. 33, no. 1, pp. 111–119, Jan. 2015.

[75] P. C. Sofotasios and S. Freear, "On the κ-μ / gamma composite distribution: A generalized multipath/shadowing fading model," in *IEEE International Microwave and Optoelectronics Conference (IMOC)*, Nov. 2011, pp. 390–394.

[76] ——, "The η-μ / gamma composite fading model," in *IEEE International Conference on Wireless Information Technology and Systems (ICWITS)*, Sep. 2010, pp. 1–4.

[77] J. Zhang, M. Matthaiou, Z. Tan, and H. Wang, "Performance analysis of digital communication systems over composite η-μ / gamma fading channels," *IEEE Transactions on Vehicular Technology*, vol. 61, no. 7, pp. 3114–3124, Sep. 2012.

[78] P. C. Sofotasios, T. A. Tsiftsis, K. H. Van, S. Freear, L. R. Wilhelmsson, and M. Valkama, "The κ-μ / IG composite statistical distribution in RF and FSO wireless channels," in *IEEE Vehicular Technology Conference (VTC)*, Sep. 2011, pp. 1–5.

[79] P. C. Sofotasios, T. A. Tsiftsis, M. Ghogho, L. R. Wilhelmsson, and M. Valkama, "The η-μ / IG distribution: A novel physical multipath/shadowing fading model," in *IEEE International Conference on Communications (ICC)*, Jun. 2013, pp. 5715–5719.

[80] W. C. Jakes, *Microwave mobile communications*. Wiley-IEEE Press, 1974.

[81] C. B. Dietrich, K. Dietze, J. R. Nealy, and W. L. Stutzman, "Spatial, polarization, and pattern diversity for wireless handheld terminals," *IEEE Transactions on Antennas and Propagation*, vol. 49, no. 9, pp. 1271–1281, Sep. 2001.

[82] J. Boutros and E. Viterbo, "Signal space diversity: A power- and bandwidth-efficient diversity technique for the Rayleigh fading channel,"

IEEE Transaction on Information Theory, vol. 44, no. 4, pp. 1453–1467, Jul. 1998.

[83] M. D. Yacoub, *Foundations of mobile radio engineering*. CRC press, 1993.

[84] H. Nam and M.-S. Alouini, "Optimization of multi-branch switched diversity systems," *IEEE Transactions on Communications*, vol. 57, no. 10, pp. 2960–2970, Oct. 2009.

[85] H. C. Yang and M.-S. Alouini, "Performance analysis of multibranch switched diversity systems," *IEEE Transactions on Communications*, vol. 51, no. 5, pp. 782–794, May 2003.

[86] ——, "Improving the performance of switched diversity with post-examining selection," *IEEE Transactions on Wireless Communications*, vol. 5, no. 1, pp. 67–71, Jan. 2006.

[87] A. M. D. Turkmani, A. Arowojolu, P. A. Jefford, and C. J. Kellett, "An experimental evaluation of the performance of two-branch space and polarization diversity schemes at 1800 MHz," *IEEE Transactions on Vehicular Technology*, vol. 44, no. 2, pp. 318–326, May 1995.

[88] D. Johnson and S. Sinanovic, "Symmetrizing the Kullback-Leibler distance," *IEEE Transactions on Information Theory*, 2001.

[89] S. Kullback, *Information theory and statistics*. Courier Corporation, 1997.

[90] A. Fort, C. Desset, P. De Doncker, P. Wambacq, and L. Van Biesen, "An ultra-wideband body area propagation channel model-from statistics to implementation," *IEEE Transactions on Microwave Theory and Techniques*, vol. 54, no. 4, pp. 1820–1826, Apr. 2006.

[91] M. Mechelke and M. Habeck, "Robust probabilistic superposition and comparison of protein structures," *BMC bioinformatics*, vol. 11, no. 363, pp. 1–13, Jul. 2010.

[92] A. P. Prudnikov, Y. A. Brychkov, and O. I. Marichev, *Integrals and Series, Volume 2: Special Functions*. Moscow: Fiziko-Matematicheskaya Literatura, 2003.

[93] C. Forbes, M. Evans, N. Hastings, and B. Peacock, *Statistical distributions*. John Wiley & Sons, 2011.

[94] Wolfram Research, Inc., 2017, visited on 26/03/2017. [Online]. Available: http://functions.wolfram.com/id.

[95] Wolfram Research, Inc., 2017, visited on 26/03/2017. [Online]. Available: http://functions.wolfram.com/Notations/5/.

[96] P. Humbert, "Sur les fonctions hypercylindriques," *Comptes rendus hebdomadaires des séances de l'Acadmie des sciences (in French)*, vol. 171, pp. 490–492, Jul. 1920.

[97] F. P. Fontán and P. M. Espiñeira, *Modelling the wireless propagation channel: A simulation approach with MATLAB*. New York: Wiley, 2008.

[98] T. Liang and D. B. Smith, "Energy-efficient, reliable wireless body area networks: Cooperative diversity switched combining with transmit power control," *IET Electronics Letters*, vol. 50, no. 22, pp. 1641–1643, Oct. 2014.

[99] D. B. Smith, "Cooperative switched combining for wireless body area networks," in *IEEE International Symposium on Personal, Indoor and Mobile Radio Communications (PIMRC)*, Sep. 2012, pp. 2275–2280.

[100] Z. Song, K. Zhang, and Y. L. Guan, "Generating correlated Nakagami fading signals with arbitrary correlation and fading parameters," in *IEEE International Conference on Communications (ICC)*, vol. 3, Apr. 2002, pp. 1363–1367.

[101] M. Deriche and A. H. Tewfik, "Maximum likelihood estimation of the parameters of discrete fractionally differenced gaussian noise process," *IEEE*

Transactions on Signal Processing, vol. 41, no. 10, pp. 2977–2989, Oct. 1993.

[102] D. Crecraft and S. Gergely, *Analog electronics: Circuits, systems and signal processing*. Butterworth-Heinemann, 2002.

[103] P. M. Shankar, "Macrodiversity and microdiversity in correlated shadowed fading channels," *IEEE Transactions on Vehicular Technology*, vol. 58, no. 2, pp. 727–732, Feb. 2009.

[104] A. A. Abu-Dayya and N. C. Beaulieu, "Micro-and macrodiversity MDPSK on shadowed frequency-selective channels," *IEEE Transactions on Communications*, vol. 43, no. 8, pp. 2334–2343, Aug. 1995.

[105] ——, "Micro-and macrodiversity NCFSK (DPSK) on shadowed nakagami-fading channels," *IEEE Transactions on Communications*, vol. 42, no. 9, pp. 2693–2702, Sep. 1994.

[106] B. Bornkamp, A. Kegel, and R. Prasad, "Macro and micro diversity in land-mobile cellular radio telephony networks with discontinuous voice transmission," in *IEEE International Conference on Universal Personal Communications (ICUPC)*, Nov. 1995, pp. 590–594.

[107] J. M. Morris and J.-L. Chang, "Burst error statistics of simulated viterbi decoded BFSK and high-rate punctured codes on fading and scintillating channels," *IEEE Transactions on Communications*, vol. 43, no. 2/3/4, pp. 695–700, Feb. 1995.

[108] A. J. Goldsmith and S.-G. Chua, "Variable-rate variable-power MQAM for fading channels," *IEEE Transactions on Communications*, vol. 45, no. 10, pp. 1218–1230, Oct. 1997.

[109] L. F. Chang, "Throughput estimation of ARQ protocols for a Rayleigh fading channel using fade- and interfade-duration statistics," *IEEE Transactions on Vehicular Technology*, vol. 40, no. 1, pp. 223–229, Feb. 1991.

[110] S. L. Cotton, "Second-order statistics of $\kappa - \mu$ shadowed fading channels," *IEEE Transactions on Vehicular Technology*, vol. 65, no. 10, pp. 8715–8720, Oct. 2016.

[111] H. Xu, V. Kukshya, and T. S. Rappaport, "Spatial and temporal characteristics of 60-Ghz indoor channels," *IEEE Journal on Selected Areas in Communications*, vol. 20, no. 3, pp. 620–630, Apr. 2002.

[112] K. Venugopal, M. C. Valenti, and R. W. Heath Jr., "Analysis of millimeter wave networked wearables in crowded environments," in *Asilomar Conference on Signals, Systems and Computers (ACSSC)*, Nov. 2015, pp. 872–876.

[113] N. Chahat, G. Valerio, M. Zhadobov, and R. Sauleau, "On-body propagation at 60 GHz," *IEEE Transactions on Antennas and Propagation*, vol. 61, no. 4, pp. 1876–1888, Apr. 2013.

[114] L. Petrillo *et al.*, "Statistical on-body measurement results at 60 GHz," *IEEE Transactions on Antennas and Propagation*, vol. 63, no. 1, pp. 400–403, Jan. 2015.

[115] S. L. Cotton, W. G. Scanlon, and B. K. Madahar, "Millimeter-wave soldier-to-soldier communications for covert battlefield operations," *IEEE Commununiations Magagine*, vol. 47, no. 10, pp. 72–81, Oct. 2009.

[116] S. L. Cotton, W. G. Scanlon, and P. S. Hall, "A simulated study of co-channel inter-BAN interference at 2.45 GHz and 60 GHz," in *European Wireless Technology Conference (EuWIT)*, Sep. 2010, pp. 61–64.

[117] T. Mavridis *et al.*, "Theoretical and experimental investigation of a 60-GHz off-body propagation model," *IEEE Transactions on Antennas Propagation*, vol. 62, no. 1, pp. 393–402, Jan. 2014.

[118] S. Rangan, T. S. Rappaport, and E. Erkip, "Millimeter-wave cellular wireless networks: Potentials and challenges," *IEEE Proceedings*, vol. 102, no. 3, pp. 366–385, Mar. 2014.

[119] Z. Pi and F. Khan, "An introduction to millimeter-wave mobile broadband systems," *IEEE Communications Magazine*, vol. 49, no. 6, pp. 101–107, Jun. 2011.

[120] C. R. Anderson and T. S. Rappaport, "In-building wideband partition loss measurements at 2.5 and 60 Ghz," *IEEE Transactions on Wireless Communications*, vol. 3, no. 3, pp. 922–928, May 2004.

[121] J. S. Lu, D. Steinbach, P. Cabrol, and P. Pietraski, "Modeling human blockers in millimeter wave radio links," *ZTE Communications*, vol. 10, no. 4, pp. 23–28, Dec. 2012.